Dynamic Wireless Charging of Electric Vehicles

Dynamic Wireless Charging of Electric Vehicles

Dissertation

for the purpose of obtaining the degree of doctor
at Delft University of Technology
by the authority of the Rector Magnificus Prof. dr. ir. T.H.J.J. van der Hagen,
chair of the Board for Doctorates,
to be defended publicly on
Monday 6 November 2023 at 12:30 o'clock

by

Wenli SHI

Master of Science in Mechanical Engineering, Beijing Institute of Technology, China
born in Wuhan, China.

The dissertation has been approved by promotors.

Composition of the doctoral committee:

Rector Magnificus,	chairperson
Prof. dr. ir. P. Bauer,	Delft University of Technology, promotor
Dr. J. Dong,	Delft University of Technology, copromotor
Independent members:	
Prof. dr. ing. A. Neto,	Delft University of Technology
Prof. dr. T.B. Soeiro,	University of Twente
Prof. dr. ing. P. Mattavelli,	University of Padova, Italy
Prof. dr. E. Lomonova,	Eindhoven University of Technology
Dr. ir. P. Venugopal,	University of Twente
Prof. ir. P.T.M. Vaessen,	Delft University of Technology, reserve member

Printed by: Gildeprint

Cover design: Meiling CHENG and Wenli SHI

ISBN 978-94-6384-494-9

An electronic version of this dissertation is available at
http://repository.tudelft.nl/.

To my mom and dad.

Contents

Summary

As a more convenient alternative to conductive charging technology, wireless charging is seen as a key technology drive for transportation electrification. In electric vehicle (EV) battery charging applications, wireless power is transferred through a magnetic link, so it is referred to as inductive power transfer (IPT). One advantage of IPT technology is that the charging of EVs can be fully automated. The recharge of traction batteries can start automatically when the EV stops where its receiver (Rx) coil is coupled with a transmitter (Tx) coil of an IPT charger. Apart from static charging applications, IPT technology can also be used to build dynamic charging roads where EVs can get charged in motion and the capacity of onboard batteries can be reduced. This thesis studied four challenges that should be addressed before dynamic IPT becomes mature enough for commercial use. The research topics focus on magnetic coupler design, prediction and control of transient behaviors, reduction of power fluctuation, and detection of EVs and foreign objects (FOs).

Magnetic coupler design

The key performance indicators of an IPT system include power transfer capability, power density, power efficiency, and misalignment tolerance. Due to conflicts among these performance indicators, it is indispensable to formulate the design of IPT charging pads as a multi-objective optimization (MOO) problem. By using finite element (FE) models, the magnetic field property of a coupler can be computed. However, calculating the aligned and misaligned power losses at the rated power requires not only the magnetic field property but also the compensation strategy. The compensation strategy determines the load match method which is used to calculate the optimal load condition and the rated winding currents. Therefore, compensation strategy should also be considered for the magnetic coupler design. With the magnetic field distribution known, the power losses in the AC link can be calculated through the existing analytical method.

This thesis develops a MOO method that can find the performance space from the design search space of magnetic couplers. In the performance space, Pareto fronts can be obtained under different conflicting optimization objectives. The study shows that analytically calculating the AC link power efficiency is possible when the magnetic field is accurately computed at the rated condition. More importantly, the DC-DC power efficiency of the final prototype reaches 97.2% which proves that the MOO design is vital to make full use of IPT technology.

Prediction and control of transient behaviors

IPT systems require capacitive/inductive components to form resonant circuits on both sides to improve the power transfer capability and power efficiency, while the compensation components also make the resonant stage of a high order. As a result, the analytical dynamic models of IPT systems are complex and mostly impossible to solve in the time domain.

This thesis proposes a new reduced-order dynamic modeling method that describes the transient behavior of a resonant stage from the energy point of view. The order of the resultant dynamic model is one-fourth that of conventional ones for SS compensated IPT systems. Also, a MPC controller is designed based on the proposed dynamic model. It is proven that simplifying the dynamic model is helpful in explaining how circuit parameters influence transient behaviors and also in facilitating the application of advanced control strategies in IPT systems.

Reduction of power fluctuation

The most obvious difference between static and dynamic IPT is the change in magnetic coupling. In DIPT applications, the magnetic coupling fluctuates from the maximum to a usable level as EVs move, so one of the main challenges of DIPT is to stabilize the pick-up power, especially for DIPT systems using segmented Tx coils where magnetic coupling changes more frequently. The conventional methods are either to overlap Tx coils or to add extra sets of the Rx sides, which are expensive in building costs.

This thesis presents the design of a segmented DIPT system using a multiphase Tx side. The Rx coil consists of two sub-windings connected in series with a relatively large spatial offset in the EV moving direction. One advantage of the proposed design is that the Tx coils are deployed loosely so the building cost can be reduced. The other advantage is that the pick-up power is seamless with a small ripple. The pick-up power demonstrates a 24.9% ripple by experiments.

Detection of EVs and FOs

To minimize the Tx side power losses and magnetic field radiation, the detection of EVs and FOs should be implemented in DIPT systems. Considering the integration of the detection equipment into the charging pads, PCB coils become the most suitable candidate to sense the magnetic field for detection purposes. However, the detection of EVs and FOs are mostly discussed separately in the literature. There is a need to achieve these two detection functions within one set of PCB coils.

This thesis presents the design of detection equipment consisting of PCB coils installed onto charging pads and the detection resonant circuit (DRC) connected to Tx side PCB coils. It can be concluded that the detection of EVs and FOs can both be realized by measuring the variation of the magnetic field caused by their intrusion, and PCB coils demonstrate good performances in measuring the change of magnetic field together with DRC to amplify the detection signals.

Samenvatting

Als handiger alternatief voor bedrade oplaadtechnologie, wordt draadloos opladen gezien als een belangrijke technologische drijfveer voor elektrificatie van transport. Bij toepassingen voor het opladen van elektrische voertuigen (EV) wordt draadloos vermogen overgedragen via een magnetische link, dus wordt dit inductieve stroomoverdracht (IPT) genoemd. Een voordeel van IPT-technologie is dat het opladen van EVs volledig geautomatiseerd kan worden. Het opladen van tractiebatterijen kan automatisch starten wanneer de EV stopt waar de ontvangerspoel (Rx) is gekoppeld aan een zenderspoel (Tx) van een IPT-lader. Afgezien van toepassingen voor statisch opladen, kan IPT-technologie ook worden gebruikt om dynamische laadwegen aan te leggen waar EVs in beweging kunnen worden opgeladen en de capaciteit van ingebouwde batterijen kan worden verminderd. Dit proefschrift bestudeerde vier uitdagingen die moeten worden aangepakt voordat dynamische IPT voldoende ontwikkeld is voor commercieel gebruik. De onderzoeksthema's richten zich op het ontwerp van magnetische koppelingen, voorspelling en controle van voorbijgaand gedrag, vermindering van vermogensfluctuaties en detectie van EVs en vreemde voorwerpen (FOs).

Ontwerp van de magnetische koppeling

De belangrijkste prestatie-indicatoren van een IPT-systeem zijn onder meer het vermogen voor vermogensoverdracht, vermogensdichtheid, energie-efficiëntie en foutieve uitlijningstolerantie. Vanwege conflicten tussen deze prestatie-indicatoren is het noodzakelijk om het ontwerp van IPT-oplaadpads te formuleren als een multi-objectief optimalisatie (MOO) probleem. Door eindige-elementen (FE) modellen te gebruiken, kan de magnetische veldeigenschap van een koppelaar worden berekend. Het berekenen van de uitgelijnde en verkeerd uitgelijnde vermogensverliezen bij het nominale vermogen vereist echter niet alleen de eigenschap van het magnetische veld, maar ook de compensatiestrategie. De compensatiestrategie bepaalt de load match-methode die wordt gebruikt om de optimale belastingstoestand en de nominale wikkelstromen te berekenen. Daarom moet ook een compensatiestrategie worden overwogen voor het ontwerp van de magnetische koppeling. Met de bekende magnetische veldverdeling kunnen de vermogensverliezen in de AC-link worden berekend via de bestaande analytische methode.

Dit proefschrift ontwikkelt een MOO-methode die de prestatieruimte kan vinden vanuit de ontwerpzoekruimte van magnetische koppelaars. In de prestatieruimte kunnen Pareto-fronten worden verkregen onder verschillende tegenstrijdige optimalisatiedoelstellingen. De studie toont aan dat analytische berekening van de energie-efficiëntie van de AC-link mogelijk is wanneer het magnetische veld nauwkeurig wordt berekend in de nominale toestand. Wat nog belangrijker is, is dat de DC-DC-stroomefficiëntie van het uiteindelijke prototype 97, 2% bereikt, wat bewijst dat het MOO-ontwerp essentieel is om volledig gebruik te maken van IPT-technologie.

Voorspelling en controle van overgangsgedrag

IPT-systemen hebben capacitieve/inductieve componenten nodig om aan beide zijden resonantiecircuits te vormen om de vermogensoverdracht en de vermogensefficiëntie te verbeteren, terwijl de compensatiecomponenten ook de resonantietrap van een hoge orde maken. Als gevolg hiervan zijn de analytische dynamische modellen van IPT-systemen complex en meestal onmogelijk op te lossen in het tijdsdomein.

Dit proefschrift stelt een nieuwe dynamische modelleringsmethode van gereduceerde orde voor die het overgangsgedrag van een resonantietrap beschrijft vanuit het oogpunt van energie. De orde van het resulterende dynamische model is een vierde van die van conventionele modellen SS-gecompenseerde IPT-systemen. Ook wordt een MPC-controller ontworpen op basis van het voorgestelde dynamische model. Het is bewezen dat het vereenvoudigen van het dynamische model nuttig is om uit te leggen hoe circuitparameters overgangsgedrag beïnvloeden en ook om de toepassing van geavanceerde besturingsstrategieën in IPT-systemen te vergemakkelijken.

Vermindering van stroomfluctuaties

Het meest voor de hand liggende verschil tussen statische en dynamische IPT is de verandering in magnetische koppeling. In DIPT-toepassingen fluctueert de magnetische koppeling van het maximale naar een bruikbaar niveau terwijl EVs bewegen, dus een van de belangrijkste uitdagingen van DIPT is het stabiliseren van het opneemvermogen, vooral voor DIPT-systemen die gesegmenteerde Tx-spoelen gebruiken waarbij de magnetische koppeling vaker verandert . De conventionele methoden zijn om Tx-spoelen te overlappen of om extra sets van de Rx-zijden toe te voegen, wat duur is qua bouwkosten.

Dit proefschrift presenteert het ontwerp van een gesegmenteerd DIPT-systeem met een meerfasige Tx-zijde. De Rx-spoel bestaat uit twee subwikkelingen die in serie zijn geschakeld met een relatief grote ruimtelijke offset in de EV-bewegingsrichting. Een voordeel van het voorgestelde ontwerp is dat de Tx-spoelen losjes worden ingezet, zodat de bouwkosten kunnen worden verlaagd. Het andere voordeel is dat het ophaalvermogen naadloos is met een kleine rimpel. De ophaalkracht demonstreert een rimpeling van 24.9% door experimenten.

Detectie van EVs en FOs

Om de vermogensverliezen aan de Tx-zijde en de straling van magnetische velden te minimaliseren, moet de detectie van EVs en FOs worden geïmplementeerd in DIPT-systemen. Gezien de integratie van de detectieapparatuur in de oplaadspoelen, worden PCB-spoelen de meest geschikte kandidaat om het magnetische veld voor detectiedoeleinden te detecteren. De detectie van EVs en FOs wordt in de literatuur echter meestal afzonderlijk besproken. Het is nodig om deze twee detectiefuncties binnen één set PCB-spoelen te realiseren.

Dit proefschrift presenteert het ontwerp van detectieapparatuur bestaande uit PCB-spoelen die zijn geïnstalleerd op oplaadspoelen en het detectieresonantiecircuit (DRC) dat is aangesloten op PCB-spoelen aan de Tx-zijde. Er kan worden geconcludeerd dat de detectie van EVs en FOs beide kan worden gerealiseerd door de variatie van het magnetische veld veroorzaakt door hun indringing te meten, en de PCB-spoelen goede resultaten zijn te zien bij het meten van de verandering van het magnetische veld samen met het DRC om de detectiesignalen te versterken.

1 Introduction

1.1 Background

Climate change has brought about a global awareness of the decarbonization of the energy system. The European Commission has made the decision to reduce at least 40% greenhouse gas emissions compared with the level of 1990 and cover at least 32% of the total energy consumption in the European Union through renewable energy sources such as wind and solar generation by 2030 [1]. The transportation section had a share of about 20% in total greenhouse gas emissions on the global scale [2]. In this context, incentive policies are announced to stimulate electrification in the transportation sector which is heavily reliant on fossil fuels. European Commission promises to end sales of new CO_2 emitted cars by 2035. As an alternative to fossil-fueled vehicles, electric vehicles (EVs) are widely promoted because EVs have no greenhouse gas emissions and provide convenient and efficient usage of the electricity produced by renewable energy sources.

Indeed, the sales of EVs have been growing rapidly all over the world in recent years. The yearly global EV sales of 2019 increased to 2.1 million with the total EV stock reaching 7.2 million, but EVs only accounted for 2.6% of global vehicle sales and about 1% of global car stock in 2019 [3]. The total number of fully electric cars on Dutch roads rose from more than 145 thousand in 2020 to 216 thousand in 2021 [4]. The major technical barriers that impede EV adoption lie in the traction batteries and charging infrastructures. With the current lithium-ion battery technology, EVs can reach the same level of driving range as fossil-fueled vehicles by increasing the number of battery packs. A Tesla Model S EV can go more than 600 km on a full charge with the air conditioner off, which generally matches the conventional vehicles. However, a large number of battery packs leads to a high price and weight of EVs. The cost, energy density, and safety of lithium-ion batteries remain to be a concern. Automotive makers, battery manufacturers, and governments have set goals to improve the performance of the lithium-ion battery, including “Energy-saving and New Energy Vehicle Technology Roadmap 2.0” in China, “Battery 500” in the USA, “Battery 2030+” in Europe, and “Research and Development Initiative for Scientific Innovation of New Generation Batteries” in Japan [5]. According to Energy-saving and New Energy Vehicle Technology Roadmap 2.0 [6], lithium-ion batteries of EVs are required to have a

lifespan above 3,500 charging cycles and a cost below 113 euros (900 Yuan converted with exchange rate in July of 2023) per kWh in 2025.

Apart from the battery technology, the charging infrastructures also significantly influence EV adoption. EVs are currently charged via conductive charging technology that requires drivers to pull and plug the cable of charging equipment. To increase the charging power and reduce the charging time, the cable has a heavy gauge to conduct a high charging current, and it becomes less convenient to connect the charging cable to EVs. A more convenient alternative to conductive charging technology is wireless charging technology. In EV battery charging applications, wireless power is transferred through a magnetic link, so it is referred to as inductive power transfer (IPT). The magnetic link is achieved by the magnetic coupler consisting of the transmitter (Tx) coil embedded in parking areas or the road, and the receiver (Rx) coil mounted to the underfloor of EVs. One advantage of IPT technology is that the charging of EVs can be fully automated. The recharge of traction batteries can start automatically when the EV stops where its Rx coil is coupled with a Tx coil of an IPT charger. The IPT chargers can be installed in parking lots for stationary charging. EVs can get charged even if the EV only parks for a short period of time. The IPT chargers can also be installed on the road for dynamic charging.

Since 2015, several standards and regulations on IPT-based wireless charging have been released and revised, including IEC 61980-1, SAE J2954 RP, and ISO/PAS 19363:3017, where the electromagnetic compatibility (EMC) limits, electromagnetic field (EMF) exposure, operating frequency range and transfer power classes are specified. Up to the date when the thesis is finished, reference designs are recommended for four power levels: 3.7 kW, 7 kW, 11 kW, and 20 kW. These reference designs have an air gap range from 100 mm to 250 mm, and a nominal frequency of 85 kHz with a tuning band of 79-90 kHz.

Significant progress has been made on IPT-based charging systems above 20 kW, as shown in Table 1.1. To accommodate the high winding currents and component stresses in the resonant circuits, the air gap and operating frequency have to be changed out of the defined ranges in the standards. It shows a trend to reduce the air gap for a higher rated power. The air gap decreases from 280 mm at the 20 kW system of Oak Ridge National Laboratory (ORNL) [24] to 30 mm at the 200 kW system of Bombardier [9]. By reducing the air gap, the magnetic coupling can be improved. The winding currents, therefore, can be lowered to transfer the same amount of power. Another way to reduce the winding current stresses is to increase the switching frequency. However, increasing the switching frequency for a higher rated power is not always favorable because the voltage stress over the compensation capacitors and between the adjacent coil turns may exceed the voltage limits of their insulation wrapping. Thus, the on-line electric vehicle (OLEV) prototypes developed by the Korea Advanced Institute of Science and Technology (KAIST) apply 20 kHz switching frequency [25]. Due to the limit in the increment of both ω_s and M considering the area power density, it is inevitable to utilize high DC-link voltages in both the Tx and Rx sides for IPT systems with high power levels. Most of the reported prototypes in Table 1.1 have a Tx side DC-link voltage above 750 V. For example, the Korea Railroad Research Institute (KRRI) applies a full-bridge resonant inverter consisting of five inverter modules and a matching transformer to reach a maximum AC voltage of 4000 V on the Tx side. Regarding the power transfer efficiency, Table 1.1 shows that the prototypes with the efficiency above 95% mostly operate at 85 kHz, except for ORNL which

uses 20 kHz at a price of lower area power density. The highest power transferred via the inductive coupling is achieved by KRRI at 818 kW with 82.7% efficiency. The highest aligned efficiency reported in the existing literature is 95.8% among prototypes including the non-isolated DC-DC converters by ETH Zurich and 96% among prototypes excluding the non-isolated DC-DC converters by ORNL. It should be mentioned that Fraunhofer Institute integrated the IPT system into an EV and the measured efficiency includes the whole charging system from the grid to the battery, which is 91% at the aligned condition.

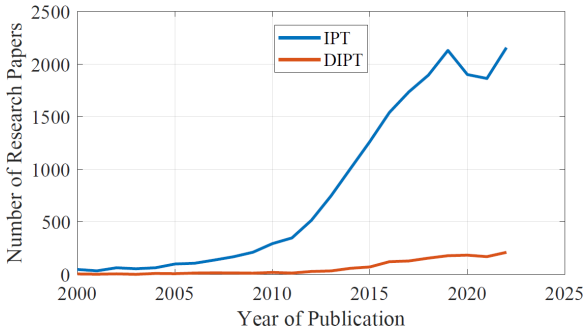

Figure 1.1: Number of research publications in IEEE Explore. The IPT curve includes both stationary and dynamic charging publications.

The research into IPT technology has increased dramatically in recent years, as presented in Fig. 1.1. In the area of high power IPT systems, great effort has been paid to the improvement of power efficiency, power density, EMF exposure, and reliability. In stationary IPT (SIPT) battery charging applications, state-of-the-art systems can achieve fast charging functions in an efficient way. From the author's understanding, IPT technology has become mature for stationary charging of EVs, and the next step of research on IPT technology is how to achieve reliable and efficient dynamic wireless charging of EVs. DIPT technology can charge EVs in motion and it is a compelling solution to extend the driving range and reduce the battery packs of EVs. Fig. 1.1 also shows that more and more researchers are working on DIPT technology.

1

Table 1.1: State-of-Art IPT Systems

References	Power [kW]	Year	Airgap [mm]	Tx-Rx side DC Voltage [V]	Aligned-Misaligned Efficiency [%]	Freq-uency [kHz]	Area Power Density [kW/m^2]
TU Delft (this study)	20	2021	150	800-800	97.2-94.1 (150 mm)	85	69.1
KRRI [7]	818	2015	50	4000(AC)-2800	82.7-N/A	60	N/A
Bombardier [8, 9]	200	2013	30	N/A	90-N/A	N/A	N/A
University of Seoul (US) [10]	150	2016	70	800-750	90.4-N/A	60	781.2
Conductix Wampfler [8]	120	2012	40	N/A	90-N/A	20	N/A
KAIST [11]	100	2014	260	five-module 500-620	80.8-N/A	20	N/A
ETH [12, 13]	50	2016	160	800-800	95.8-92 (150 mm)	85	160
ORNL [14]	50	2020	150	3ϕ 550-580	95-88.5 (100 mm)	85	195
Zhejiang University (ZJU) [15]	50	2021	160	three-module 800-600	95.2-N/A	85	208
WAVE [16]	50	2015	178	3ϕ 480-N/A	92-N/A	23.4	N/A
Showa Aircraft [17]	30	2009	140	N/A	92-N/A	22	N/A
INTIS [18, 19]	30	2014	100	N/A	90-N/A	30	N/A
KAIST [20]	27	2011	200	N/A-550	74-N/A	20	33.7
New York University (NYU) [21]	25	2016	210	750-375	91-N/A	85	N/A
KAIST [22]	22	2015	200	N/A	71-N/A	20	27.5
Fraunhofer [23]	22	2015	136	800-800	91-89 (120 mm)	100	61.1
ORNL [24]	20	2021	280	800-420	96-N/A	22	31.9

1.2 Key Technical Challenges

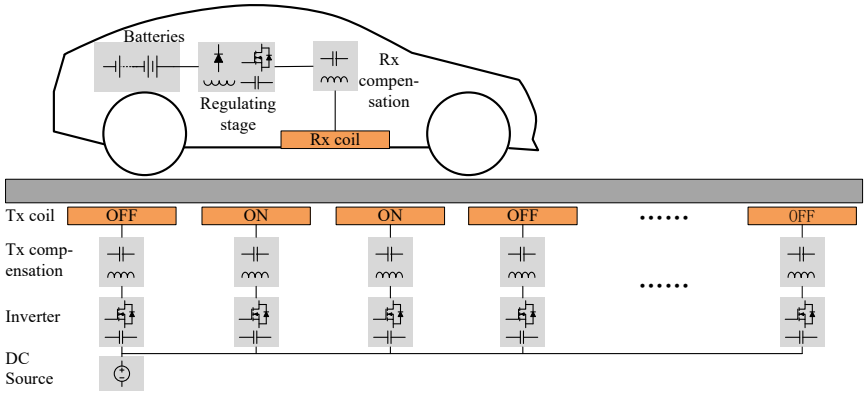

Figure 1.2: Basic architecture of segmented DIPT systems.

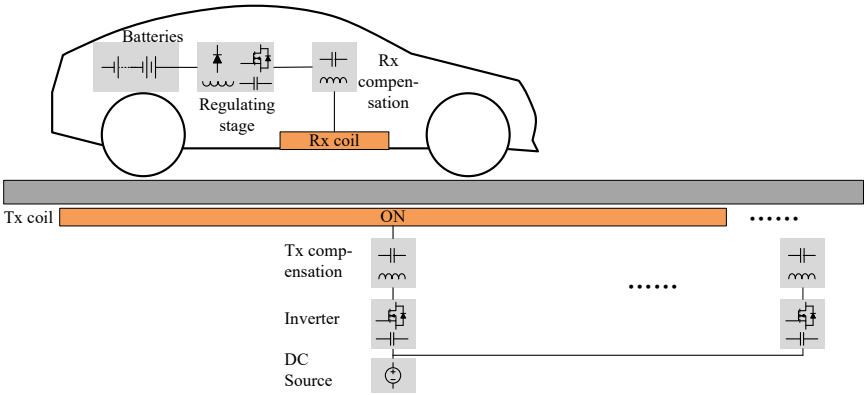

Figure 1.3: Basic architecture of elongated DIPT systems.

The fundamental difference between DIPT and SIPT systems is the magnetic coupling between the Tx and Rx coil. As EVs move in the roadway, the magnetic coupling changes with a ripple up to 100% depending on the mechanical design of the magnetic coupler. This kind of coupling change makes DIPT systems operate under critical conditions. When the magnetic coupling is low, winding currents have to be increased to compensate for the drop in the pick-up power. Consequently, the power electronics and main coils should be designed with a larger safety margin, which incurs higher building costs. To maintain a seamless pick-up power, the magnetic coupling should be above a certain value all the way, and the easiest way is to stretch the Tx coil in the driving direction like the OLEV system [20], as presented in Fig. 1.3. However, the build cost of such elongated Tx coils is high and the high leakage inductance leads to low power efficiency. Alternatively, the Tx coil can be made in a segmented form like the SIPT systems [8], as shown in Fig. 1.2. The Tx coils can be switched on only when they are coupled with a Rx coil, so the Tx side power

losses and stray magnetic field can be minimized. To achieve high power efficiency and power density of the DIPT system, it is essential to conduct a multiobjective optimization design of the magnetic couplers.

It is inevitable that the magnetic coupling curve varies with a large ripple in a segmented DIPT system. The variation of the magnetic coupling forces the system to operate under a transient state, and the current and voltage may have peak values several times larger than their steady-state values. As a result, the control system should have a fast and precise response to smooth the pick-up power. It becomes essential to develop a dynamic modeling method to predict the transient behavior of DIPT systems and assist the control system in improving the transient performance.

The pick-up power will also fluctuate and even become seamed particularly when the Tx coils are loosely deployed. The magnetic coupling variation can be suppressed by placing Tx coils in a tight or overlapped way. If the magnetic coupling curve becomes seamless and always beyond a certain value, the pick-up power can be further smoothed by controlling the back-end DC-DC converter. What remains a problem is the considerable rise in the building cost due to the increased number of Tx coils. Therefore, innovative ideas are required to stabilize the pick-up power and avoid high building costs, so DIPT technology can attract more attention from governments and EV companies.

The control of the pick-up power is highly reliant on the feedback signals of EV and foreign object detection. In DIPT systems, the Tx coils should only be switched on when they are coupled with an Rx coil, so the stray field and power losses on the Tx side can be minimized. The foreign objects are very likely on the open road. Mteal-based foreign objects reduce the efficiency of the DIPT system and can even catch fire because of circulating eddy currents and resulting losses. In order to improve the reliability of the DIPT system, both the mechanisms and detection methods of foreign objects should be studied.

1.2.1 Optimization Design of Magnetic Couplers

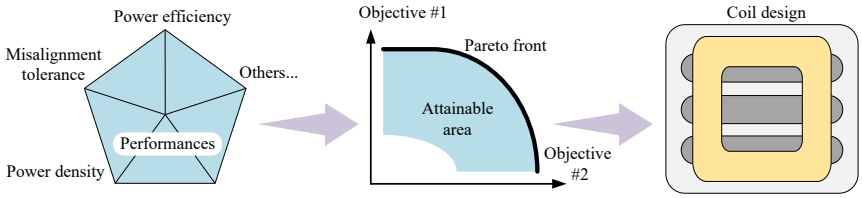

Figure 1.4: MOO framework illustration. Based on the defined performance indicators, a Pareto front can be derived in the performance space of IPT systems, and an optimal design should be on or close to the Pareto front depending on the application preferences.

The performance index of IPT systems, including the rated power, power transfer efficiency, power density and misalignment tolerance, are limited by a number of design constraints. Since the receiver (Rx) side components are mounted in the EV, the allowable space and weight of the circuit are bounded. Therefore, a high power density of the IPT system is required. According to the standards SAE J2954, the air gap in the isolating transformer ranges from 100 mm to 250 mm, and the achievable magnetic coupling between the transmitter (Tx) and the Rx pads is limited. As compensation for the low magnetic

coupling, the winding currents tend to be relatively high to reach the rated power. It is reported in [12] that the major sources of the power losses are the conduction loss in the semiconductors and the power loss in the capacitors and windings, which are mostly determined by the winding current. Thus, the power efficiency of IPT systems is limited and naturally smaller than conductive chargers. To ensure a high power transmission, it is inevitable to use large pads for a high magnetic coupling. Additionally, these pads would employ Litz wire with a reasonable current density and a large number of compensation capacitors connected in series and parallel to deal with the commonly high voltage and current stresses. This trend results in conflicts between the power efficiency and power density of IPT systems. To deal with conflicts among different performance indicators, the design of IPT systems should be formulated into a MOO problem as shown in Fig. 1.4. Finite element (FE) models are found to be effective and accurate in computing the Pareto front in the performance space based on a specified design search space.

As reported in [26], an important figure-of-merit (*FOM*), $FOM = kQ$ where k is the magnetic coupling coefficient and Q is the coil quality factor, determines the maximum efficiency of an IPT system [27]. Extensive research has been conducted into both the coil topology [28–34] and the optimization of the geometric parameters [12, 35–38] for a high *FOM*. In [35], a multi-objective optimization (MOO) method is proposed for the design of circular charging pads. This MOO method conducts a parametric sweep within the design search space and takes the power transfer efficiency and power density as the optimizing objectives, which illustrates the conflicts between these two objectives in the form of Pareto fronts. Later, this MOO method is applied to design a 50 kW IPT system with a DC-DC efficiency of 95.8 % at the aligned condition in [12]. It is common that there is a misalignment between the Tx and Rx pads when there are no aid-positioning devices, but the misaligned performances of IPT systems are not studied in [12, 35]. Although the misalignment is considered in the MOO method proposed in [36], the proposed optimal design is not experimentally validated. Therefore, the challenge is to propose a MOO method that considers both the aligned and misaligned performances of IPT systems, and also to verify the correctness of the optimal results in a prototype.

1.2.2 Modeling of Dynamic Characteristics

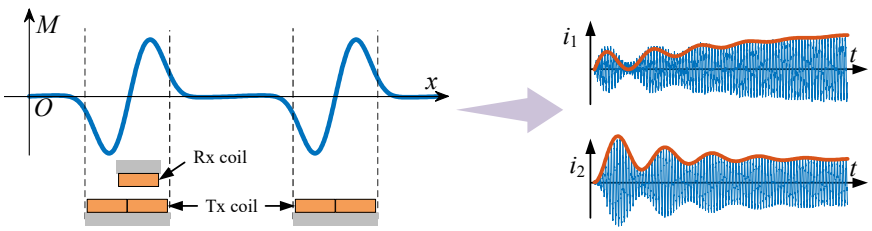

Figure 1.5: Dynamic behavior of DIPT systems. Since the magnetic coupling changes over time, the DIPT system should be controlled based on its transient behavior, especially during the turning on transients. i_1 and i_2 represent the Tx and Rx side winding current during a turn-on transient.

Due to the discrete operation of switches and changing magnetic coupling between Tx and Rx coils, the instantaneous model of a DIPT system is discontinuous and time-variant.

1

As illustrated in Fig. 1.5, the Tx power supply may turn on and off depending on the magnetic coupling, and the magnetic coupling changes over time, which can result in a large variation of the system output. It becomes important to model and analyze the dynamic behaviors. To study a specific design, the instantaneous model can be processed numerically to evaluate its dynamic characteristics [39]. However, the instantaneous model offers limited insights into the design of the feedback controller and the optimization of the resonant circuit components. To overcome the discontinuity and time-variance of the instantaneous model and to derive analytic solutions, the oscillating state variables can be transformed into slowly varying variables, based on the short-time Fourier transform. Existing studies report dynamic modeling methods including state-space averaging (SSA), generalized state-space averaging (GSSA) [40, 41], Laplace phasor transformation (LPT) [42–44], extended describing function (EDF) [45] and coupled model theory (CMT) [46, 47].

The SSA method is not applicable for IPT systems since the fundamental harmonic components of state variables cannot be neglected [48]. The GSSA method is based on a time-dependent Fourier series representation for a sliding window of state variables. When fundamental harmonics approximation is applied in the GSSA model, each oscillating state variable is represented by a complex variable, thus the order of the AC circuit is doubled. The state-space models using GSSA and LPT are essentially the same. The advantage of the LPT method is that the time-domain model can be transformed into a phasor-domain model where conventional circuit analysis techniques can be applied [43], and it is possible to reduce the order of the state-space model through circuit analysis [44]. The CMT method models the LC resonant tank from the energy point of view and the oscillating current through the inductor and the voltage across the capacitor can be replaced by the energy magnitude and phase which are two slowly varying real variables. In this way, the order of the state-space model derived from the CMT method is further reduced.

The aforementioned methods can reduce the order of the dynamic model of IPT systems, but the order of these models is not low enough to provide insights into the transient behaviors of an IPT system [44]. Besides, it obstructs the applications of control strategies where the analytical dynamic model is required. The challenge is to find a new dynamic model that can simplify the transient analysis and facilitate the application of control strategies relying on the analytical system model,

1.2.3 Detection of Electric Vehicles and Foreign Objects

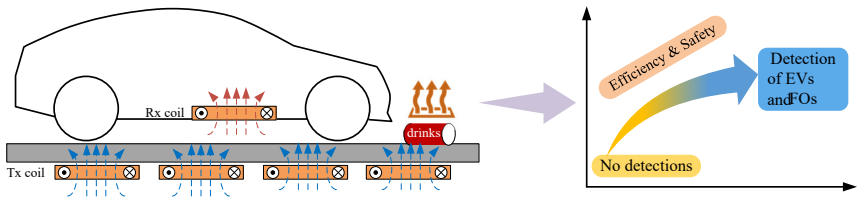

Figure 1.6: Detection functions of DIPT systems. Both the detection of EVs and FOs should be realized to improve the power transfer efficiency and safety of a DIPT system.

When segmented charging pads are used in DIPT systems, the energized Tx coils uncoupled with a Rx will give rise to unnecessary power losses as well as leakage magnetic

field which may be hazardous to nearby human beings and animals [49, 50]. It is equally important to detect foreign objects that can be heated up due to the eddy current loss and become a fire hazard to a DIPT system. Therefore, the DIPT Tx should be turned ON/OFF depending on the position of the EV as well as the presence of FOs [51, 52], which makes the EV and FO detection function necessary.

The EVD methods can be broadly classified into three categories. The first kind measures the variation of system performances for EVD, which requires no auxiliary devices [53–55]. As the mutual coupling increases as the EV approaches to the Tx, variations can be observed in the phase angle between the primary input current and voltage [53] and also in the amplitude of the primary winding current [55] for a detuned DIPT system. The second kind of EVD method relies on the image, magnetic field and coordinate information extracted from auxiliary equipment including camera [56], satellite [57], magnetic sensor [58] and infrared light sensor [59]. The auxiliary equipment is of a high cost to be integrated into the DIPT system. The third kind of EVD method applies auxiliary coils [51, 60, 61]. In [51, 60], auxiliary coils are deployed on both Tx and Rx sides. The auxiliary coil on the Rx side is constantly energized, so the auxiliary coils on the Tx side have an increasing induced voltage as the EV approaches. By analyzing the pattern of the induced voltage changes in different Tx side auxiliary coils, the position and speed of EVs can be estimated. The flat shape of the auxiliary coils has advantages in the integration design, which is appealing to DIPT systems.

Numerous FOD solutions have been reported in the IPT charging applications. They are divided into two types. The first one detects MFOs by observing any variation in system parameters resulting from the MFOs, including the coil quality factor [62], resonance or cut-off frequency [63, 64], and system efficiency [65]. The second type of FOD method relies on auxiliary coil sets mounted on the Tx side, which can be either passive [52, 66–68] or active [69]. Based on the literature study, the research topics of EVD and FOD are mostly discussed separately. Although the reported auxiliary coil arrays in [52] can realize FOD and EVD when the Tx and Rx are operating, this method is not suitable for DIPT applications where the Tx should not be energized before identifying the position of EVs. The operation of the EVD using auxiliary coils can be affected by the MFO. This makes the FOD essential to maintain the reliability of the EVD, while the challenge is to the integration design of the EVD and FOD in DIPT systems.

1.2.4 Reduction of Pick-up Power Fluctuation

A DIPT system can use segmented coils to build a Tx track and the segmented coils commonly have a similar size to the Rx coil, as depicted in Fig. 1.2. Provided the position of the Rx coil is known, the segmented coils can be energized sequentially, such that the power losses of the Tx track and the unwanted stray magnetic field can be minimized. The disadvantage is that the magnetic coupling changes inevitably as EVs move, and the pick-up power becomes unstable or even seamed. To address this issue, elongated DIPT systems using rectangular Tx coil much longer than EVs are studied [70], as illustrated in Fig. 1.3. However, the power transfer efficiency drops because the leakage magnetic field increases as the Tx coil becomes longer. Also, the voltage stresses over Tx side compensation components increase and special attention should be paid to dealing with insulation problems [71].

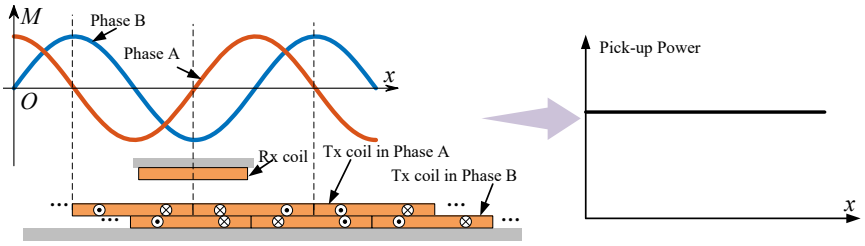

Figure 1.7: A dual-phase elongated DIPT system using BC-Rectangular coil as the magnetic coupler. By placing Tx coils of different phases with a certain spatial offset along x axis (the driving direction), the pick-up power can become independent of the position of EVs in x direction.

Elongated DIPT systems using bipolar coil (BC)-DD (length direction) and BC-Rectangular coil magnetic couplers have a sinusoidal magnetic coupling curve as shown in Fig. 1.7. The period of the sinusoidal curve is equal to twice the pole length of the elongated DD coil. To avoid null power points, there are studies proposing multiphase Rx side [72, 73], which can only suppress the fluctuation of the pick-up power. To realize a stable pick-up power, the multiphase Tx track is proven to be a reliable solution for elongated DWPT systems with a sinusoidal magnetic coupling curve [74–76]. In the multiphase Tx track, multiple identical elongated BC coils are overlapped with a spatial offset in the driving direction. These elongated BC coils are powered by AC power sources with a certain phase shift. With the multiphase Tx track, the pick-up power of the elongated DWPT system with a sinusoidal magnetic coupling curve becomes independent of the Rx coil position in the driving direction, namely a stable output power. However, the material cost of the multiphase Tx track is too high since the total copper used for the Tx track is equal to the product of that of a single-phase coil multiplied by the number of the system phases. The challenge is to maintain a stable pick-up power without overlapping Tx coils to save material costs.

1.3 Research Objectives and Questions

The main research objective of this doctoral thesis is as follows:

develop a reliable, economic, fast, and dynamic inductive charging system for electric vehicle battery charging applications.

To achieve the objectives, the research questions to be studied in this doctoral thesis are as follows:

1. How to optimize the IPT charging pad?
    - Study the recent development of multi-objective optimization strategies and find the suitable coil topology and compensation topology.
    - Analyse the losses within power electronics and coils, cores, and shielding considering the skin and proximity effect.
    - Apply the intelligent algorithm to find optimal designs maximizing the power density, efficiency, and misalignment tolerance.

- Design, construct and test the prototype using the obtained optimal results to verify the proposed optimization approach.

2. How to model the dynamic characteristics of DIPT systems?
   - Study the reported dynamic modeling methods and evaluate their potential in simplifying the dynamic model of DIPT systems.
   - Evaluate the transients of an LC resonant tank and apply the method to an IPT system.
   - Compare the derived dynamic model with a conventional one in terms of accuracy and complexity.
   - Use the derived dynamic model to assist in the implementation of advanced control strategies.
   - Validate the accuracy of the proposed dynamic model and the effectiveness of the developed control strategy.
3. What is the most suited solution for the detection of EVs and foreign objects in DIPT systems?
   - Make a survey of the existing detection methods.
   - Analyze the pros and cons of different detection methods.
   - Develop a detection resonant circuit to achieve the detection of EVs and FOs in the same detection coil.
   - Build FEM models and experiment setups to validate proposed detection methods.
4. How to reduce the pick-up power fluctuation of DIPT systems?
   - Review and evaluate the magnetic coupling curve of different DIPT systems.
   - Study the principle of multiphase DIPT systems and evaluate their performance and shortcomings.
   - Apply the multiphase method on a segmented DIPT system and optimize the deployment of Tx and Rx coils.
   - Test the pick-up power of the proposed segmented DIPT system and verify the effectiveness of the proposed design approach in stabilizing the pick-up power.

1.4 Outline of the Thesis

This thesis aims to answer four research questions in different aspects of IPT applications. Each research question constitutes one chapter of this thesis. The outline and connections between chapters of this thesis are presented in Fig. 1.8. Chapter 2 introduces the basic operating principles of IPT systems and elaborates on the features of the SS and DLCC compensation circuits based on their steady-state models. Chapter 3 presents a MOO method to design an IPT system and the optimal design is validated in a 20 kW prototype. Chapter 4 proposes a continuous reduced-order dynamic modeling method to describe

1

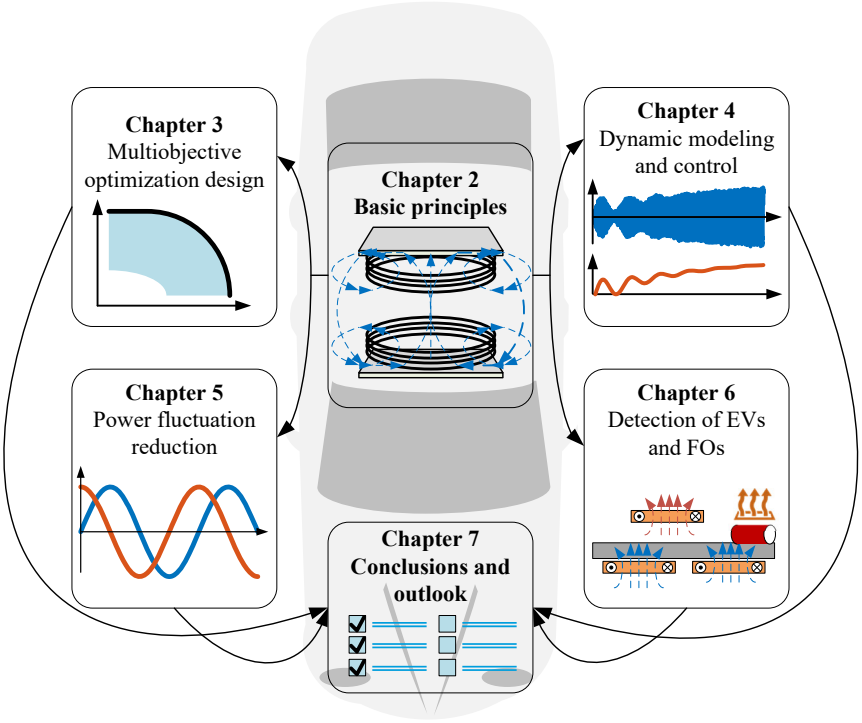

Figure 1.8: Outline of the doctoral thesis, and connections between chapters.

the transient behavior of IPT systems using the SS compensation and a MPC controller is designed based on the proposed dynamic model. Chapter 5 proposes the design of a DIPT system employing multiphase Tx side to stabilize the pick-up power without increasing the copper material cost on the Tx side. Chapter 6 presents the design of a detection device that can detect both EVs and FOs using PCB coils. Finally, Chapter 7 summarizes the conclusions and future work of this thesis.

2

Steady State Modeling

Wireless charging via magnetic coupling is called inductive power transfer (IPT). The core parts of IPT systems include a high-frequency inverter and rectifier, magnetic coupler, and compensation circuits. This chapter will first introduce the circuit model of two coupled coils. Then, the steady-state impedance models of AC links using series-series (SS) and double-sided inductor-capacitor-capacitor (DLCC) are presented. The input impedance frequency response is analyzed to explain the zero voltage switching (ZVS) turn-on operation condition of a SiC-based inverter. Finally, a detailed comparison between the SS and DLCC compensation is presented to provide guidance on the selection of compensation strategies for different charging requirements.

This chapter is based on:

- W. Shi, J. Dong, T. B. Soeiro, C. Riekerk, F. Grazian, G. Yu, P. Bauer, *"Design of a highly efficient 20-kw inductive power transfer system with improved misalignment performance"*, *IEEE Transactions on Transportation Electrification*, 8(2):2384-2399.

2.1 Introduction

The basic schematic of an IPT system is presented in Fig. 2.1. This circuit implements a power factor correction circuit for compliance with integration guidelines to the public AC grid (the AC-DC front-end), an isolated resonant-based DC-DC converter comprising an H-bridge inverter cascaded to a capacitive compensation circuit forming a two-stage equivalent resonant tank with the transmitter and receiver coils, and a rectifying stage (the back-end AC-DC converter). Finally, a non-isolated DC-DC converter can be used to control the charging profile across the battery of the vehicle. This final circuit can be controlled so that the battery and non-isolated DC-DC converter will behave as a controllable equivalent resistive load for the isolated DC-DC resonant converter. By adjusting the input voltage and the equivalent resistive load to the isolated DC-DC converter, maximum power efficiency can be attained at the rated output power.

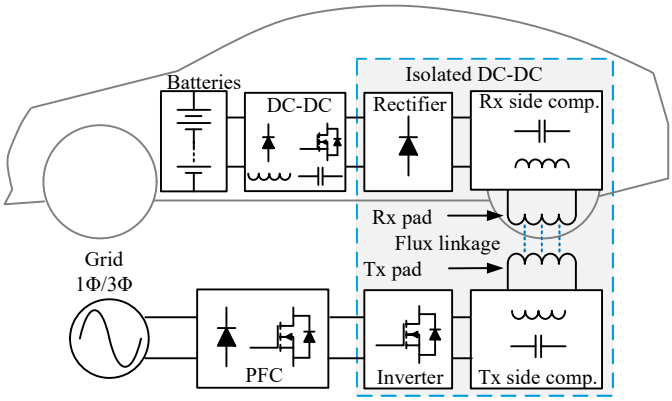

Figure 2.1: Core structure of an IPT system.

This chapter will introduce the basic operating principles of IPT systems applying different compensation strategies. The circuit model of two coupled coils is first introduced to explain the necessity of compensation circuits to improve the power transfer capability and efficiency. Then, the steady state impedance models of AC links using series-series (SS) and double-sided inductor-capacitor-capacitor (DLCC) are presented. The input impedance frequency response is analyzed to explain the zero voltage switching (ZVS) turn-on operation condition of a SiC-based inverter. Finally, a detailed comparison between the SS and DLCC compensation is presented to provide guidance on the selection of compensation strategies for different charging requirements.

2.2 Coupled Coils

Fig. 2.2(a) illustrates the magnetic flux of two coupled coils that are driven by two independent currents i_1 and i_2. The magnetic flux produced by one coil and intersecting the other one is defined as the mutual magnetic flux, ϕ_{12} and ϕ_{21}, and the rest is defined as the leakage flux, ϕ_{11} and ϕ_{22}. According to Faraday's law, the voltage of coils is calculated as

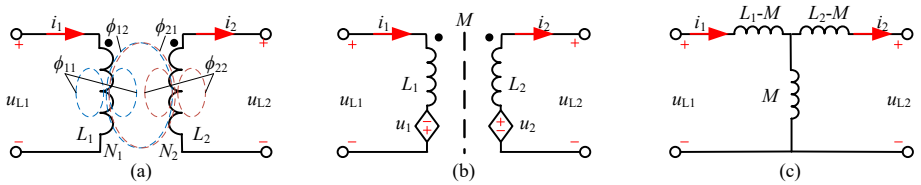

Figure 2.2: Two coupled coils.

$$u_{L1} = N_1 \frac{d(\phi_{11} + \phi_{12} - \phi_{21})}{dt}, \tag{2.1a}$$

$$u_{L2} = N_2 \frac{d(\phi_{22} + \phi_{21} - \phi_{12})}{dt}. \tag{2.1b}$$

It is known that the coupled mutual flux is the media where the energy can be exchanged within these two coils. The energy balance in this energy interaction is given by

$$N_1 i_1 \frac{\phi_{21}}{dt} = N_2 i_2 \frac{\phi_{12}}{dt} \Rightarrow \frac{N_1 \phi_{21}}{i_2} = \frac{N_2 \phi_{12}}{i_1} = M. \tag{2.2}$$

The self-inductance of coils are defined as $L_1 = \frac{N_1(\phi_{11}+\phi_{12})}{i_1}$ and $L_2 = \frac{N_2(\phi_{22}+\phi_{21})}{i_2}$. By substituting (2.2) to (2.1), one can get

$$u_{L1} = L_1 \frac{di_1}{dt} - M \frac{di_2}{dt}, \tag{2.3a}$$

$$u_{L2} = L_2 \frac{di_2}{dt} - M \frac{di_1}{dt}, \tag{2.3b}$$

(2.3) explicitly explains that the voltage of coupled coils is determined by the coil self-inductance and their mutual inductance. Therefore, the coupled coils model in Fig. 2.2(a) is equivalent to the induced voltage model in Fig. 2.2(b). (2.3) can be further expressed as

$$u_{L1} = (L_1 - M) \frac{di_1}{dt} + M \frac{d(i_1 - i_2)}{dt}, \tag{2.4a}$$

$$u_{L2} = (L_2 - M) \frac{di_2}{dt} + M \frac{d(i_2 - i_1)}{dt}. \tag{2.4b}$$

Based on (2.4), the coupled coils model can be replaced by T-model that is depicted in Fig. 2.2(c). The advantage of T-model is that circuit analysis techniques can be easily used to study the impedance behaviors of loosely coupled IPT systems.

To analyze the power interaction between two coupled coils, the induced voltage model in Fig. 2.2(b) is studied in this section. Assuming that power is transferred from the left-hand side to the right-hand side, the transferred power P_{12} is calculated as

$$P_{12} = \Re \left\{ j\omega_s M \mathbf{I}_1 \mathbf{I}_2^* \right\} = \omega_s M I_1 I_2 \sin \varphi_{12}. \tag{2.5}$$

To achieve a rated power delivery, it is preferable to increase the angular switching frequency ω_s, M and $sin(\varphi_{12})$, so I_1 and I_2 can be reduced to minimize the power losses. Regarding the increment of ω_s and M, certain design considerations should be respected, including the cost of components, the bandwidth of high-power semiconductors, and allowed onboard construction volume.

A higher operation frequency implies the rise of the eddy current losses within the ferrite core and shielding losses. To reduce the skin effect loss, a finer strand of Litz wire is required, leading to a higher cost and a larger outer diameter for the same effective cross-section.

The increment of M can be realized by putting the Tx and Rx coil closer such that the magnetic reluctance of the mutual flux path declines, while the flexibility feature becomes weak. Another way of increasing M is to apply more copper and ferrite to expand the size at a price of a higher cost and a lower power density. It is preferred to have an asymmetric coil design that the Tx is larger than the Rx, because of limited onboard space.

To maximize the value of $sin(\varphi_{12})$, the cascaded circuits to the secondary coil should be designed to have $\varphi_{12} \approx \frac{\pi}{2}$. It means the input impedance seen from u_2 must be resistive, and a common way is to adopt capacitors to compensate for the reactance of L_2. The most simple way is to connect the secondary coil in series to a capacitor whose capacitance is equal to $\frac{1}{\omega_s^2 L_2}$. Extra inductors can also be employed to form LCL or LCC resonant circuits for the same purpose. Another advantage of compensating the reactance of L_2 is that the output capacity can be improved. As presented in Fig.2.3, the secondary side can be seen to be powered by a constant voltage source when I_1 is constant. The output power P_L to the load R_L changes from $\frac{u_2^2 R_L}{2(\omega_s L_2 + R_L)^2}$ to $\frac{u_2^2 R_L}{2(\omega_s L_2 - 1/(\omega_s C_2) + R_L)^2}$. It is obvious that P_L is maximized when C_2 is equal to $\frac{1}{\omega_s^2 L_2}$.

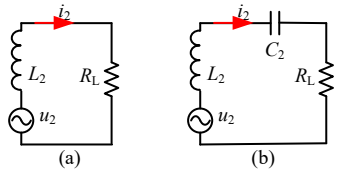

Figure 2.3: Resistive load connected to the Rx side (a) uncompensated, (b) compensated.

It is similar on the Tx side that the capacitive compensation is also necessary to compensate the reactance of L_1 and the reflected impedance from the Rx side. By slightly tuning the switching frequency, the primary side compensation can ensure zero voltage switching turn-on operation of the inverter employing SiC MOSFET as switches. Generally, the compensation circuit design is to realize the following goals:

- Minimize the VA rating of the power electronics devices for rated power.
- Achieve load-independent output characteristics, current source or voltage source behavior.
- Improve the capability of charging power to the load.
- ZVS operation of the inverter using SiC MOSFETs.

2.3 Compensations

As a loosely coupled system, capacitors, commonly connected in series and/or parallel to a charging pad, are used to compensate for the self-inductance of the Tx/Rx pads so that the power transfer capability and efficiency of the system can be improved [77, 78]. The compensation is typically implemented by connecting a resonant capacitor in series or parallel to the Tx/Rx coil. For the Rx side, the parallel compensation requires a series filter inductor after the rectifying stage to limit the current through the semiconductor, resulting in a bulky secondary converter design. Considering that the space on the vehicle side is limited and the reflected impedance is not resistive, the secondary parallel compensation is not favorable in EVs charging applications where misalignment tolerance is taken into account. As a solution to this problem, the filter inductor can be replaced by a compensation inductor connected in series between the parallel resonant tank and the rectifying stage, forming an LCL compensation circuit. To further reduce the size of the compensation inductor and improve the power transfer capability, a capacitor is connected in series with the Rx coil, forming a LCC compensation circuit. Since the compensated inductor can be integrated into the charging pad [77], the compact converter design is attainable.

To ensure the high-efficiency operation of the inverter applying MOSFETs, the Tx side compensation circuits are typically designed to have the zero phase angle (ZPA) input impedance at the resonant frequency to minimize the power requirement for the inverter. Thus, the primary series and LCC compensation are widely used for EVs charging applications. In practice, the switching frequency can slightly deviate from the resonant frequency to have the output current lagging the output voltage of the inverter, allowing for its ZVS turn-on operation, which is favorable for most MOSFET semiconductor technologies.

Based on the above discussion, the SS and DLCC compensations are found to be suitable candidates for EV charging applications because of their constant current output characteristics.

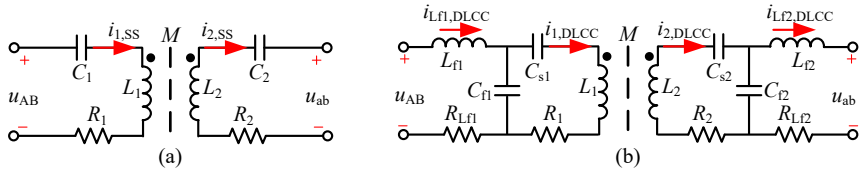

Figure 2.4: AC link of IPT systems using (a) SS or (b) DLCC compensation.

2.3.1 SS Compensation Circuits

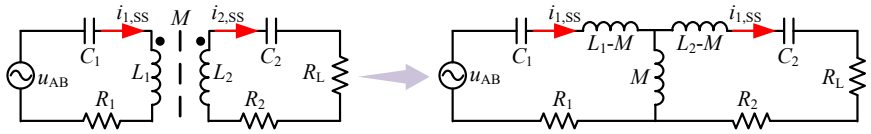

Figure 2.5: AC link of SS compensated IPT systems.

The resonant circuit of a SS compensated IPT system is illustrated in Fig. 2.5. In Section 2.1, we have introduced the T-model for the coupled two coils due to its advantage in analyzing the impedance of the resonant circuit. Based on the T-model in Fig. 2.5, the time-domain model of the circuit is given by

$$u_{\mathrm{AB}} = L_1 \frac{di_{1,\mathrm{SS}}}{dt} - M\frac{di_{2,\mathrm{SS}}}{dt} + R_1 i_{1,\mathrm{SS}} + u_{\mathrm{C1,SS}}, \tag{2.6a}$$

$$i_{1,\mathrm{SS}} = C_1 \frac{du_{\mathrm{C1,SS}}}{dt}, \tag{2.6b}$$

$$M\frac{di_{1,\mathrm{SS}}}{dt} = L_2 \frac{di_{2,\mathrm{SS}}}{dt} + i_{2,\mathrm{SS}}(R_2 + R_{\mathrm{L}}) + u_{\mathrm{C2,SS}}, \tag{2.6c}$$

$$i_{2,\mathrm{SS}} = C_2 \frac{du_{\mathrm{C2,SS}}}{dt}. \tag{2.6d}$$

The time-domain model can be used to predict the behavior of the resonant circuits in both steady state and transient state. In the steady state analysis, the fast-varying variables in (2.6) will be replaced by their phasors. Taking $i_{1,\mathrm{SS}}$ as an example,

$$i_{1,\mathrm{SS}} = \Re\left\{\mathbf{I}_{1,\mathrm{SS}} e^{j\omega_{\mathrm{s}} t}\right\} = \Re\left\{I_{1,\mathrm{SS}} e^{j\omega_{\mathrm{s}} t + \varphi_{I_{1,\mathrm{SS}}}}\right\}. \tag{2.7}$$

In the steady state, the time rate change of $I_{1,\mathrm{SS}}$ and $\varphi_{i_{1,\mathrm{SS}}}$ is zero, so the $\frac{di_{1,\mathrm{SS}}}{dt}$ is calculated as

$$\frac{di_{1,\mathrm{SS}}}{dt} = \Re\left\{\frac{d(\mathbf{I}_{1,\mathrm{SS}} e^{j\omega_{\mathrm{s}} t})}{dt}\right\} = \Re\left\{j\omega_{\mathrm{s}}\mathbf{I}_{1,\mathrm{SS}} e^{j\omega_{\mathrm{s}} t} + \frac{dI_{1,\mathrm{SS}} e^{\varphi_{I_{1,\mathrm{SS}}}}}{dt} e^{j\omega_{\mathrm{s}} t}\right\} = \Re\left\{j\omega_{\mathrm{s}}\mathbf{I}_{1,\mathrm{SS}} e^{j\omega_{\mathrm{s}} t}\right\}. \tag{2.8}$$

Based on (2.7) and (2.8), we can derive the frequency-domain model of the SS compensation circuit as

$$\mathbf{U}_{\mathrm{AB}} = j\omega_{\mathrm{s}} L_1 \mathbf{I}_{1,\mathrm{SS}} - j\omega_{\mathrm{s}} M \mathbf{I}_{2,\mathrm{SS}} + R_1 \mathbf{I}_{1,\mathrm{SS}} + \mathbf{U}_{\mathrm{C1,SS}}, \tag{2.9a}$$

$$\mathbf{I}_{1,\mathrm{SS}} = j\omega_{\mathrm{s}} C_1 \mathbf{U}_{\mathrm{C1,SS}}, \tag{2.9b}$$

$$j\omega_{\mathrm{s}} M \mathbf{I}_{1,\mathrm{SS}} = j\omega_{\mathrm{s}} L_2 \mathbf{I}_{2,\mathrm{SS}} + \mathbf{I}_{2,\mathrm{SS}}(R_2 + R_{\mathrm{L}}) + \mathbf{U}_{\mathrm{C2,SS}}, \tag{2.9c}$$

$$\mathbf{I}_{2,\mathrm{SS}} = j\omega_{\mathrm{s}} C_2 \mathbf{U}_{\mathrm{C2,SS}}. \tag{2.9d}$$

By using the frequency-domain model in (2.9), the currents and voltages in the compensation circuit can be solved, and the results can be used to calculate the power efficiency and analyze the frequency behavior of the resonant circuits. In the SS compensation circuit, C_1 and C_2 are

$$C_1 = \frac{1}{\omega_{\mathrm{s}}^2 L_1}, \tag{2.10a}$$

$$C_2 = \frac{1}{\omega_{\mathrm{s}}^2 L_2}. \tag{2.10b}$$

Therefore, the reactance of L_1 and L_2 can be fully compensated at the operating frequency ω_{s}, and $\mathbf{I}_{1,\mathrm{SS}}$ and $\mathbf{I}_{2,\mathrm{SS}}$ can be solved from (2.9) as

$$\mathbf{I}_{1,\mathrm{SS}} = \frac{(R_2 + R_{\mathrm{L}})\mathbf{U}_{\mathrm{AB}}}{R_1(R_2 + R_{\mathrm{L}}) + \omega_{\mathrm{s}}^2 M^2}, \tag{2.11a}$$

$$\mathbf{I}_{2,\mathrm{SS}} = \frac{j\omega_s M \mathbf{U}_{\mathrm{AB}}}{R_1(R_2+R_\mathrm{L})+\omega_s^2 M^2}. \tag{2.11b}$$

As R_1 and R_2 are far smaller than $\omega_s M$ in highly efficient IPT systems, (2.11) can be further simplified as

$$\mathbf{I}_{1,\mathrm{SS}} \approx \frac{R_\mathrm{L}\mathbf{U}_{\mathrm{AB}}}{\omega_s^2 M^2}, \tag{2.12a}$$

$$\mathbf{I}_{2,\mathrm{SS}} \approx \frac{j\mathbf{U}_{\mathrm{AB}}}{\omega_s M}. \tag{2.12b}$$

It is obvious in (2.12b) that the output current $\mathbf{I}_{2,\mathrm{SS}}$ is independent of the load resistance R_L, so the SS compensated IPT system has a load-independent current-source output behavior. Besides, $\mathbf{I}_{2,\mathrm{SS}}$ is in-phase with the induced voltage in Rx coil. From (2.12a), we can see that the $\mathbf{I}_{1,\mathrm{SS}}$ is in-phase with $\mathbf{U}_{\mathrm{AB}}$, so the input impedance of the SS compensated IPT system is almost resistive. In summary, the SS compensated IPT system has a current-source output behavior and the reactive power is minimized on both sides to ensure highly efficient operation.

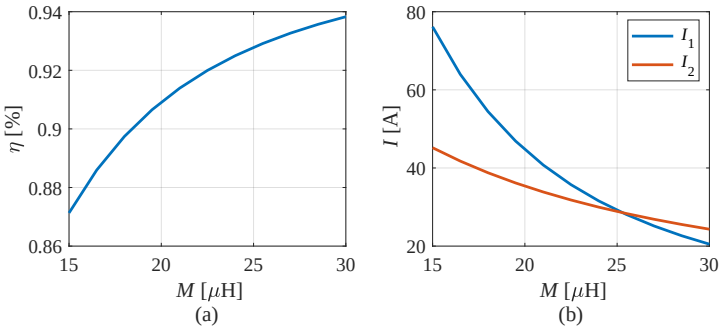

Figure 2.6: Misalignment performances of SS compensated IPT systems.

In EV charging applications, it is inevitable to have a misalignment between the Tx and Rx coils. (2.12) shows that I_1 and I_2 will increase as the magnetic coupling drops, given U_{AB} is constant. The performance of a SS compensated IPT system is illustrated in Fig. 2.6. As the mutual inductance M declines, the winding current increases on both sides, while the efficiency drops.

Bifurcation operation

To realize the ZVS turn-on operation of the inverter, the input impedance of the compensation circuit $\mathbf{Z}_{\mathrm{in,SS}} = \frac{\mathbf{U}_{\mathrm{AB}}}{\mathbf{I}_{1,\mathrm{SS}}}$ should be inductive, which is commonly done by tuning the operating frequency slightly deviating from the resonant frequency. Based on the frequency-domain model in (2.9), we can solve $\mathbf{Z}_{\mathrm{in,SS}}$ as

$$\mathbf{Z}_{\mathrm{in,SS}} = \frac{j\omega_\mathrm{r}((-L_2(g_s-1)^2(g_s+1)^2L_1+M^2g_s^4)\omega_\mathrm{r}+jL_1(g_s-1)R_\mathrm{L}g_s(g_s+1))}{g_s(-g_s^2\omega_\mathrm{r}L_2+jR_\mathrm{L}g_s+\omega_\mathrm{r}L_2)} \tag{2.13}$$

2

where ω_r is the angular resonant frequency of the compensation circuit and $\omega_s = g_s\omega_r$. When $\omega_s = \omega_r$, we can get $\mathbf{Z}_{in,SS} = \frac{\omega_r^2 M^2}{R_L}$ from (2.13). Therefore, the input impedance $\mathbf{Z}_{in,SS}$ of a SS compensated IPT system is purely resistive when the system operates at resonance, as shown in Fig. 2.7. Fig. 2.7 also shows that the number of zero-crossing points may increase from 1 to 3 as the load resistance R_L decreases and mutual inductance M increases, which is referred to as bifurcation. The bifurcation happens when the system satisfies

$$k > \frac{R_L}{\omega_r L_2}. \tag{2.14}$$

When the system operates at non-bifurcation conditions, $\angle\mathbf{Z}_{in,SS}$ can be adjusted to be inductive by keeping ω_s slightly higher than ω_r. Thus, the ZVS operation of the inverter can be guaranteed without increasing too much reactive power. However, increasing ω_s cannot ensure an inductive $\mathbf{Z}_{in,SS}$ when the system operates in bifurcation conditions. As shown in Fig. 2.7, $\mathbf{Z}_{in,SS}$ becomes capacitive first as ω_s increase from ω_r when multiple zero-crossing points exist. By reducing R_L and increasing M, the SS compensated IPT system can transit from non-bifurcation to bifurcation operation. As a result, the ZVS operation of the inverter may fail and the power efficiency drops. It is recommended to ensure the non-bifurcation operation in the design process, so the inductive $\mathbf{Z}_{in,SS}$ can be realized by slightly increasing ω_s.

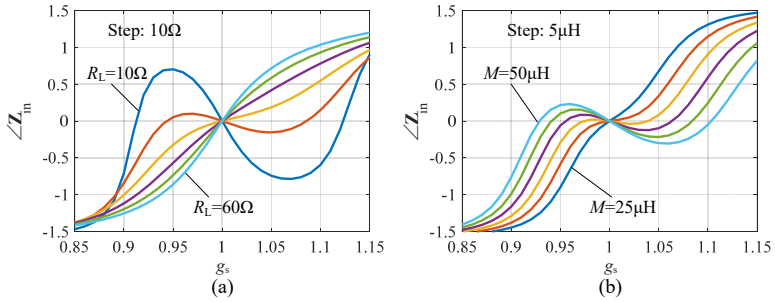

Figure 2.7: Bifurcation of SS compensated IPT systems.

2.3.2 DLCC Compensation Circuits

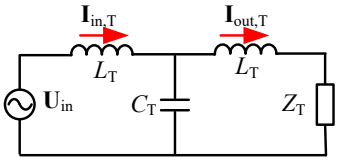

Figure 2.8: A T-type resonant circuit.

The DLCC compensation includes four passive components on both sides, which makes the circuit model of a high order. To simplify the analysis, we will first study the behavior

of the T-type resonant circuit presented in Fig. 2.8, because the T-type resonant circuit emerges on both sides of the DLCC compensation circuit. By selecting the capacitor $C_{\mathrm{T}} = \frac{1}{\omega_{\mathrm{s}}^2 L_{\mathrm{T}}}$, we can derive the input impedance $Z_{\mathrm{in,T}}$ as

$$Z_{\mathrm{in,T}} = \frac{\mathbf{U}_{\mathrm{in,T}}}{\mathbf{I}_{\mathrm{in,T}}} = \frac{\omega_s^2 L_{\mathrm{T}}^2}{Z_{\mathrm{T}}}, \tag{2.15}$$

where Z_{T} is the impedance of the cascaded circuit. Also, the output current $\mathbf{I}_{\mathrm{out,T}}$ can be solved as

$$\mathbf{I}_{\mathrm{out,T}} = \frac{\mathbf{U}_{\mathrm{in,T}}}{j\omega_{\mathrm{s}} L_{\mathrm{T}}}, \tag{2.16}$$

which shows that $\mathbf{I}_{\mathrm{out,T}}$ is independent of Z_{T}. Therefore, when the T-type resonant circuit is powered by a voltage source at the resonant frequency, the T-type resonant circuit works as a current source to the cascaded circuit.

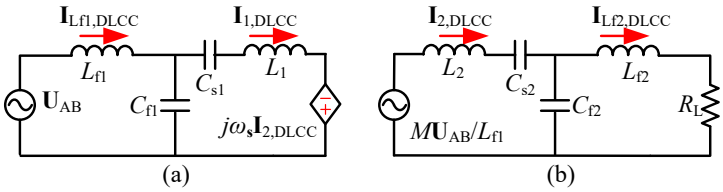

Figure 2.9: DLCC compensated IPT systems.

The equivalent Tx and Rx sides circuit of a DLCC compensation network is depicted in Fig. 2.9. To form the T-type resonant circuit, the DLCC compensation components satisfy

$$C_{\mathrm{f1}} = \frac{1}{\omega_{\mathrm{s}}^2 L_{\mathrm{f1}}}, C_{\mathrm{f2}} = \frac{1}{\omega_{\mathrm{s}}^2 L_{\mathrm{f2}}} \tag{2.17a}$$

$$C_{\mathrm{s1}} = \frac{1}{\omega_{\mathrm{s}}^2 (L_1 - L_{\mathrm{f1}})}, C_{\mathrm{s2}} = \frac{1}{\omega_{\mathrm{s}}^2 (L_2 - L_{\mathrm{f2}})} \tag{2.17b}$$

In Fig. 2.9(a), a T-type resonant circuit is powered by the voltage source $\mathbf{U}_{\mathrm{AB}}$. According to (2.16), the Tx side winding current $\mathbf{I}_{1,\mathrm{DLCC}}$ can be solved as

$$\mathbf{I}_{1,\mathrm{DLCC}} = \frac{\mathbf{U}_{\mathrm{AB}}}{j\omega_{\mathrm{s}} L_{\mathrm{Lf1}}}. \tag{2.18}$$

Given $\mathbf{U}_{\mathrm{AB}}$ is a constant voltage source, $\mathbf{I}_{1,\mathrm{DLCC}}$ is constant, so the Rx side of the DLCC compensation circuit can also be seen to be powered by a constant voltage source as shown in Fig. 2.9(b). Similar as the Tx side of the DLCC compensation circuit, the output current $\mathbf{I}_{\mathrm{Lf2,DLCC}}$ can be obtained as

$$\mathbf{I}_{\mathrm{Lf2,DLCC}} = \frac{M\mathbf{U}_{\mathrm{AB}}}{j\omega_{\mathrm{s}} L_{\mathrm{Lf1}} L_{\mathrm{Lf2}}}. \tag{2.19}$$

When the load resistive R_{L} is seen as a voltage source that has a voltage of $\frac{MR_{\mathrm{L}}\mathbf{U}_{\mathrm{AB}}}{j\omega_{\mathrm{s}} L_{\mathrm{Lf1}} L_{\mathrm{Lf1}}}$, we can also solve $\mathbf{I}_{2,\mathrm{DLCC}}$ and $\mathbf{I}_{\mathrm{Lf1,DLCC}}$ as

$$\mathbf{I}_{2,\mathrm{DLCC}} = \frac{M\mathbf{U}_{\mathrm{AB}}}{\omega_{\mathrm{s}}^2 L_{\mathrm{Lf1}} L_{\mathrm{Lf2}}^2}, \tag{2.20a}$$

$$\mathbf{I}_{\mathrm{Lf1,DLCC}} = \frac{M^2 \mathbf{U}_{\mathrm{AB}}}{\omega_s^2 L_{\mathrm{Lf1}}^2 L_{\mathrm{Lf2}}^2}. \tag{2.20b}$$

Based on the above analysis, it can be summarized that the DLCC compensated IPT system has a current source output behavior. Besides, the Tx side winding current is independent of both the mutual inductance M and load resistance R_{L}, which makes the system less sensitive to variations of magnetic coupling and is advantageous for DIPT applications. In DIPT systems employing the DLCC compensation, the over-current fault in the Tx coil can be easily avoided by setting a threshold to U_{AB}.

According to (2.15), the Rx side input impedance seen from the induced voltage in the Rx winding $\mathbf{Z}_{\mathrm{2,DLCC}}$ is calculated as

$$\mathbf{Z}_{\mathrm{2,DLCC}} = \frac{\omega_s^2 L_{\mathrm{f2}}^2}{R_{\mathrm{L}}}, \tag{2.21}$$

which is resistive, so the $\mathbf{I}_{\mathrm{2,DLCC}}$ is in phase with the induced voltage in the Rx coil. By calculating the reflected impedance of the Rx side on the Tx side, the Tx side input impedance $\mathbf{Z}_{\mathrm{in,DLCC}}$ can be solved as

$$\mathbf{Z}_{\mathrm{in,DLCC}} = \frac{\omega_s^2 L_{\mathrm{f1}}^2 L_{\mathrm{f2}}^2}{M^2 R_{\mathrm{L}}}. \tag{2.22}$$

$\mathbf{Z}_{\mathrm{in,DLCC}}$ is resistive when the system operates under the resonant condition. However, $\mathbf{Z}_{\mathrm{in,DLCC}}$ has to be slightly inductive so the ZVS operation of the inverter can be ensured.

In SS compensated IPT system, we can make ω_s slightly higher than ω_r under the non-bifurcation condition to realize the ZVS operation of the inverter. However, the high-order nature of the DLCC compensation makes the frequency response of the IPT system more complex. Fig. 2.10 shows the frequency response of the phase angle of $\mathbf{Z}_{\mathrm{in,DLCC}}$ under different R_{L} and M. In the studied g_s range $0.7-1.3$, the number of zero-crossing points is 3 or 5 depending on the value of R_{L} and M. It shows a trend that increasing R_{L} and M can ensure $\angle\mathbf{Z}_{\mathrm{in,DLCC}}$ to be inductive when ω_s is slightly higher than ω_r. However, it is hard to find the design criteria to calculate the boundary value of R_{L} and M, due to the complexity of $\mathbf{Z}_{\mathrm{in,DLCC}}$.

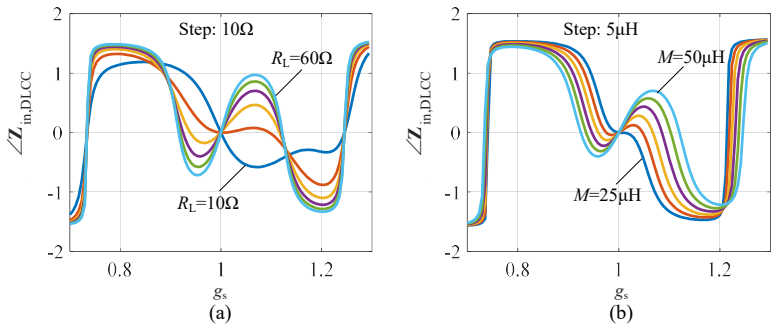

Figure 2.10: Phase angle of the input impedance of DLCC compensated IPT systems.

2.4 Maximum Efficiency Analysis

Previous research has been conducted into the optimal load condition for the SS compensated IPT systems [79–81]. The analytical expressions of both the maximum efficiency and the optimal load have been solved, which provides good insights on the design of the IPT system [36]. Different from the SS compensation, the parameters of the DLCC compensation are designed based on the self-inductance of the charging pads as well as the DC voltage and the rated power [82–86]. Due to the consideration of misalignment tolerance and the limited space for the Rx side, the Tx pad tends to cover a larger area than that of the Rx pad. This kind of design results in an asymmetric selection of the compensation parameters, and the definition of the self-inductance of the compensation inductors L_{fi} (subscript $i = 1$ for the Tx side and $i = 2$ for the Rx side) is critical for the high-efficiency operation. In [84], the expressions of the maximum efficiency and optimal load condition is derived and found to be dependent on the selection of L_{fi}. In [86], a comparison of the power efficiency is presented between a specific DLCC and a SS compensation circuits under the condition that the magnetic coupler and the compensation component equivalent series resistance are the same, but the selection of the L_{fi} for the maximum efficiency is not studied. It is found in [83] that an optimal L_{fi} exists for the maximum efficiency. However, due to the complexity of the double-sided LCC compensation circuit, the analytical expression of the optimal L_{fi} is not derived. Therefore, this paper proposes an efficiency analysis method that does not involve the specifications of the compensation circuit, and a fair comparison between the SS compensation and the double-sided LCC compensation is presented in terms of the total power losses in the AC link.

A general schematic of the AC link of an IPT system is presented in Fig. 2.4. The voltages across C_{i}, C_{si} and C_{fi} are $\mathbf{U}_{\mathrm{i,SS}}$, $\mathbf{U}_{\mathrm{i,DLCC}}$ and $\mathbf{U}_{\mathrm{fi,DLCC}}$, respectively. The power transferred from the Tx side to the Rx side P_{12} has been introduced in (2.5). For both the SS and DLCC compensation circuits, the Rx side compensation can satisfy $\phi_{12} = \frac{\pi}{2}$. From (2.5), one can obtain

$$I_1 I_2 = \frac{P_{12}}{\omega_{\mathrm{s}} M} \tag{2.23}$$

To study the power losses in the AC link, the equivalent AC resistance R_{i} is assumed to be connected in series to L_{i}. When the IPT system applies SS compensation as (2.10), the power losses within the AC link $P_{\mathrm{loss,SS}}$ can be calculated as

$$P_{\mathrm{loss,SS}} = I_{1,\mathrm{SS}}^2 R_1 + I_{2,\mathrm{SS}}^2 R_2 \tag{2.24}$$

I_{i} and R_{i} are both positive-valued. Based on (2.24) and (2.23), one can get

$$P_{\mathrm{loss,SS}} \geq \underbrace{2 I_{1,\mathrm{SS}} I_{2,\mathrm{SS}} \sqrt{R_1 R_2}}_{2 \frac{P_{12}}{\omega_{\mathrm{s}} M} \sqrt{R_1 R_2}} \tag{2.25}$$

The equality of (2.25) is attained when $I_{1,\mathrm{SS}} \sqrt{R_1} = I_{2,\mathrm{SS}} \sqrt{R_2}$, implying that the maximum efficiency is achieved close to the operating point where the power losses in the Tx and Rx sides are balanced.

The equivalent AC resistance R_{fi} is assumed to be connected in series to L_{fi} that is the self-inductance of the compensated inductors. When the IPT system applies DLCC compensation as (2.17), the power losses within the AC link $P_{\mathrm{loss,DLCC}}$ can be calculated as

$$P_{\text{loss,DLCC}} = I_{\text{1,DLCC}}^2 R_1 + I_{\text{2,DLCC}}^2 R_2 + I_{\text{f1,DLCC}}^2 R_{\text{f1}} + I_{\text{f2,DLCC}}^2 R_{\text{f2}} \tag{2.26}$$

Similar to (2.25), one can obtain

$$P_{\text{loss,DLCC}} \geq \underbrace{2I_{\text{1,DLCC}} I_{\text{2,DLCC}} \sqrt{R_1 R_2}}_{2\frac{P_{12}}{\omega_s M}\sqrt{R_1 R_2}} + 2I_{\text{f1,DLCC}} I_{\text{f2,DLCC}} \sqrt{R_{\text{f1}} R_{\text{f2}}} \tag{2.27}$$

The equality of (2.27) is attained when

$$I_{\text{1,DLCC}} \sqrt{R_1} = I_{\text{2,DLCC}} \sqrt{R_2}, I_{\text{Lf1,DLCC}} \sqrt{R_{\text{Lf1}}} = I_{\text{Lf2,DLCC}} \sqrt{R_{\text{Lf2}}}, \tag{2.28}$$

which suggests that the maximum efficiency is realized close to the operating point where the power losses in the Tx and Rx sides are balanced.

It can be concluded by (2.25) and (2.27) that the minimal value of $P_{\text{loss,SS}}$ is smaller than that of $P_{\text{loss,LCC}}$ when P_{12} is fixed. A specific case is presented in [86] where the same magnetic coupler and the same compensation component equivalent series resistance are applied to a SS and a DLCC circuit, and the SS circuit is found to be more efficient than the DLCC.

2.5 Comparison of SS and DLCC Compensation Circuits

As the power of IPT systems increases, the current stresses over the coils and the voltage stresses over the capacitors are essential issues to be considered. On one hand, the high current density through the winding can cause thermal problems, and the Litz wire with a large number of strands should be selected as a compromise. The increment of the outer diameter of the Litz wire constrains the minimal gap between the adjacent coil turns, and a relatively large pad size is designed. On the other hand, the rated voltage over the compensated capacitors could be above 10 kV which is far higher than the maximum AC voltage of one single off-shelf commercial film capacitor for 85 kHz applications. It is common to connect a large number of single capacitor units in series to distribute the voltage stress. Reducing the current/voltage stresses is essential for the integration design of the AC link.

The selection of compensation topology is vital in determining the winding currents and the capacitor voltages. To have a fair comparison between the SS and DLCC compensated IPT systems, the system performances are analyzed in terms of the power transfer efficiency η, DC voltage requirement $U_{\text{dc,i}}$, voltage stresses ($U_{\text{i,SS}}$, $U_{\text{i,DLCC}}$ and $U_{\text{fi,DLCC}}$) and current stresses ($I_{\text{i,SS}}$, $I_{\text{i,DLCC}}$ and $I_{\text{fi,DLCC}}$) with the DC voltage ranging from 400 V to 850 V. As the compensation performance of the DLCC compensated IPT system is dependent on the selection of L_{fi}. A parametric sweep is applied within the feasible range of L_{fi}. The ratio of L_{fi} to L_{i} is defined as γ_i, and $\gamma_1 = \gamma_2 = \gamma$ for simplicity. The self-inductances of the Tx and Rx pads are 292.3 μH and 199.6 μH, which is derived from the selected pad design in Chapter 3. To consider the misaligned performances, the aligned and misaligned mutual inductances are 50 μH and 25 μH, respectively. The output power is set to be 20 kW. γ can

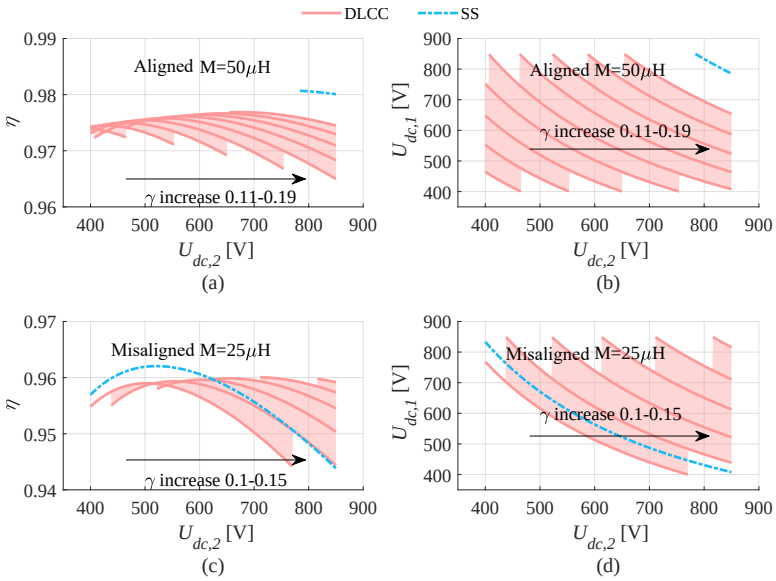

Figure 2.11: Comparison of SS and DLCC compensation circuits under different Rx side DC voltage, in terms of (a) and (c) the AC link efficiency, (b) and (d) the Tx sided DC voltage requirements. At aligned conditions, the mutual inductance is 50 μH as shown in (a) and (b). At misaligned condition, the mutual inductance is 25 μH as shown in (c) and (d).

be calculated as

$$\gamma = \sqrt{\frac{8MU_{\mathrm{dc},1}U_{\mathrm{dc},2}}{\pi^2\omega_s P_{\mathrm{out}} L_1 L_2}} \tag{2.29}$$

Therefore, γ is investigated in the range of $0.1-0.19$. To analyse the efficiency of the IPT system, the quality factor Q of the charging pads and the compensation inductors are set to be 500 at 85kHz, which is close to that of the final prototype. The equivalent AC resistances can be obtained as (subscript $i = 1,2$ stands for the Tx and Rx sides of the IPT system, respectively)

$$R_{\mathrm{i}} = \frac{\omega_{\mathrm{s}} L_{\mathrm{i}}}{Q}, R_{\mathrm{fi}} = \frac{\omega_{\mathrm{s}} L_{\mathrm{fi}}}{Q} \tag{2.30}$$

The AC link efficiency and DC voltage requirements under aligned and misaligned conditions are presented in Fig. 2.11. In both Fig. 2.11(a) and 2.11(c), the efficiency of the DLCC compensated IPT system is heavily dependent on the selection of γ, and the design with a larger value of γ is found to have a higher maximum efficiency. It is because $I_{\mathrm{fi,DLCC}}$ reduces with the rise of L_{fi}. It can also be seen that the maximum efficiency of the SS compensation is higher than that of the DLCC compensation, which verifies the analysis in Section III-B. In comparison of Fig. 2.11(b) and 2.11(d), the effective range of $U_{\mathrm{dc,i}}$ becomes narrow for SS compensation when M increases, indicating that there exists a maximum value of M for the SS compensation to deliver the rated power considering the maximum permissible DC voltage. The DLCC compensation can have a larger effective range of $U_{\mathrm{dc,i}}$ by properly selecting γ. However, if the design objective of the DLCC compensation is

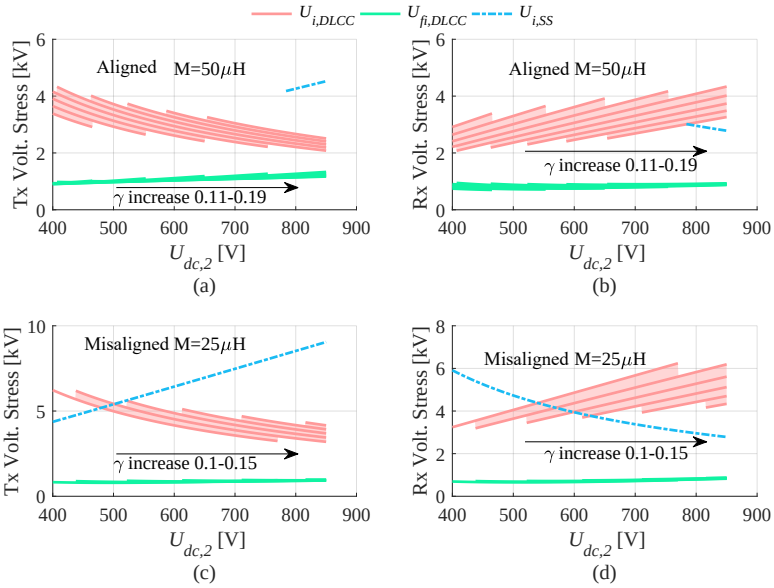

Figure 2.12: Comparison of SS and DLCC compensation circuits under different Rx side DC voltage, in terms of (a) and (c) the Tx side AC voltage stresses, (b) and (d) the Rx sided AC voltage stresses. At aligned conditions, the mutual inductance is 50 μH as shown in (a) and (b). At misaligned condition, the mutual inductance is 25 μH as shown in (c) and (d).

to maximize η, the largest value of γ should be selected and the effective range of $U_{\mathrm{dc,i}}$ is comparable to that of the SS compensation. It can be summarized that the SS and DLCC compensations have the same trend that η is high when the system can use a high DC voltage on both sides, and the SS compensation has a higher maximum efficiency than the DLCC compensation under the same M and P_{out}.

The voltage over the capacitors under aligned and misaligned conditions is depicted in Fig. 2.12. It can be seen that $U_{\mathrm{fi,DLCC}}$ is constantly lower than $U_{\mathrm{i,DLCC}}$ for the DLCC compensation. When comparing the SS and DLCC compensation, $U_{1,\mathrm{SS}}$ is mostly above $U_{1,\mathrm{DLCC}}$ and the difference increases when $U_{\mathrm{dc,1}}$ rises as shown in Fig. 2.12(a) and 2.12(c). The trend is reversed for the Rx side as presented in Fig. 2.12(b) and 2.12(d). $I_{2,\mathrm{DLCC}}$, $I_{\mathrm{f2,DLCC}}$ and $I_{2,\mathrm{SS}}$ can be expressed as

$$I_{2,\mathrm{DLCC}} = \frac{2\sqrt{2}U_{\mathrm{dc,2}}}{\pi\omega_{\mathrm{s}}L_{\mathrm{f2}}} \tag{2.31a}$$

$$I_{\mathrm{f2,DLCC}} = I_{2,\mathrm{SS}} = \frac{\pi P_{\mathrm{out}}}{2\sqrt{2}U_{\mathrm{dc,2}}} \tag{2.31b}$$

It is proved by (2.31) that $I_{2,\mathrm{DLCC}}$ increases but $I_{2,\mathrm{SS}}$ decreases as a higher $U_{\mathrm{dc,2}}$ is applied. Besides, the reactance of C_{s2} is close to that of C_2 because γ is small. Thus, the Rx side voltage stress of DLCC compensation is generally higher than that of the SS compensation, especially when $U_{\mathrm{dc,2}}$ is high and M is low as indicated in Fig. 2.12(d). As the Rx side has

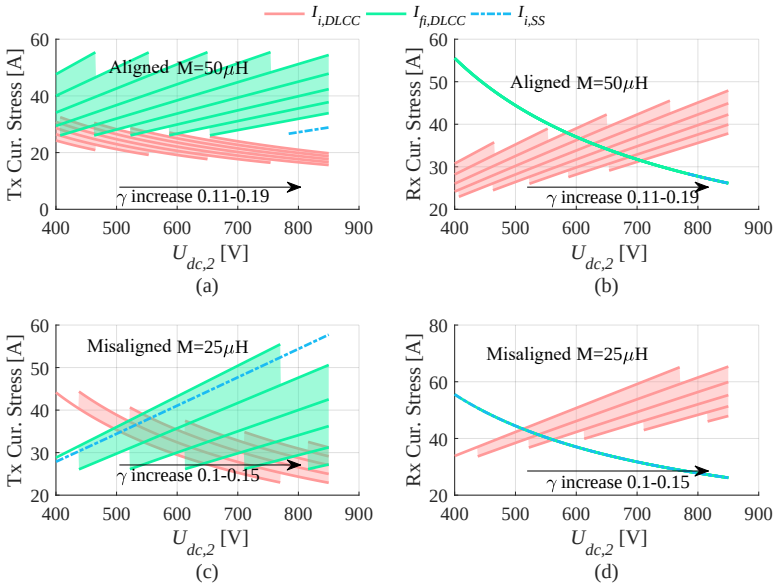

Figure 2.13: Comparison of SS and DLCC compensation circuits under different Rx side DC voltage, in terms of (a) and (c) the Tx side AC current stresses, (b) and (d) the Rx sided AC current stresses. At aligned conditions, the mutual inductance is 50 μH as shown in (a) and (b). At misaligned condition, the mutual inductance is 25 μH as shown in (c) and (d).

limited space, reducing the voltage stress on the Rx side is of higher priority to the Tx side, which makes the SS compensation more advantageous.

The current through both windings and the compensation inductors under aligned and misaligned conditions are presented in Fig. 2.13. It shows that the same side currents of the DLCC compensation cannot be reduced at the same time, which can be explained by (2.31). For the Tx side current stresses, the SS compensation presents better performances under the aligned condition as illustrated in Fig. 2.13(a) where $I_{1,\mathrm{SS}}$ is below the region covered by $I_{\mathrm{f1,DLCC}}$. However, the Tx side of the DLCC tends to have a lower current stress under the misaligned condition as shown in Fig. 2.13(c). Regarding the Rx side current stresses, the SS compensation is always better than that of the DLCC within the effective region of $U_{\mathrm{dc,2}}$. As per Fig. 2.13(b) and 2.13(d), $I_{2,\mathrm{DLCC}}$ is considerably larger than $I_{\mathrm{f2,DLCC}}$ and $I_{2,\mathrm{SS}}$ when a high $U_{\mathrm{dc,2}}$ is applied. It can be found that the DLCC compensation is more advantageous in avoiding high Tx side current stresses under misaligned conditions. By contrast, the SS compensation holds obviously lower current stress on the Rx side under both aligned and misaligned conditions, which is more favorable in EV charging applications.

2.6 Conclusions

This chapter has introduced the basic operating principles of IPT systems. Due to the current source output characteristics of the SS and DLCC compensation circuits, their performances are analyzed in particular. Regarding the ZVS operation condition, the analytical non-bifurcation criteria of the SS compensation circuit can help the designer to find the operating

condition to ensure an inductive input impedance when ω_s is slightly higher than ω_r. By contrast, the input impedance frequency response of the DLCC compensation is much more complex, and no analytical approach is available for the designer to identify the number of zero-crossing points. Then, the power transfer efficiency, and voltage/current stresses on AC link components are compared in a case study of a 20 kW IPT system. It has been found that the SS compensation outperforms the DLCC compensation in terms of maximum power efficiency and Rx side voltage/current stresses. Considering the limited construction volume on the EV side, reducing Rx side voltage/current stresses is advantageous because the size of AC link components on the Rx side can be reduced correspondingly. However, the DLCC compensation has its unique feature that the Tx winding current is independent of the magnetic coupling, which is advantageous for DIPT applications.

3

IPT System Design and Optimization

Due to the urgent desire for a fast, convenient, and efficient battery charging technology for electric vehicle (EV) users, extensive research has been conducted into the design of high-power inductive power transfer (IPT) systems. However, there are few studies that formulate the design as a multi-objective optimization (MOO) research question considering both the aligned and misaligned performances and validating the optimal results in a full-scale prototype. This chapter presents a comprehensive MOO design guideline for highly efficient IPT systems and demonstrates it by a highly efficient 20 kW *IPT system with the DC-DC efficiency of* 97.2% *at the aligned condition and* 94.1% *at* 150 mm *lateral misalignment. This achievement is a leading power conversion efficiency metric compared to IPT EV charging systems disseminated in today's literature. Herein, a MOO method is proposed to find the optimal design of the charging pads, taking the aligned/misaligned efficiency and area/gravimetric power density as the objectives. Finally, a prototype is built according to the MOO results. The charging pad dimension and total weight, including the housing material, are* $516 \times 552 \times 60$ mm^3/25 kg *for the transmitter and* $514 \times 562 \times 60$ mm^3/21 kg *for the receiver. Correspondingly, the gravimetric, volumetric, and area power densities are* 0.435 kW/kg, 581 kW/m^3, *and* 69.1 kW/m^3, *respectively. The measured efficiency agrees with the anticipated value derived from the given analytical models.*

This chapter is based on:

- W. Shi, J. Dong, T. B. Soeiro, C. Riekerk, F. Grazian, G. Yu, P. Bauer, *"Design of a highly efficient 20-kw inductive power transfer system with improved misalignment performance"*, *IEEE Transactions on Transportation Electrification*, 8(2):2384-2399.

3.1 Introduction

In IPT systems, the energy transferred from the Tx side to the Rx side relies on magnetic coupling. A high coupling is favorable to improve the efficiency in high-power applications since less Tx side winding current is required. As a price of high coupling, the size of charging pads may be designed larger and thus become more expensive. The misalignment tolerance can also be improved by enlarging the size of the charging pad. Considering the limited size on the EV side, a trade-off emerges among the power transfer efficiency, power density as well as misalignment tolerance. Therefore, a multi-objective optimization (MOO) design is recommended for the design of IPT systems.

In [35], a multi-objective optimization (MOO) method is proposed for the design of circular charging pads. This MOO method conducts a parametric sweep within the design search space and takes the power transfer efficiency and power density as the optimizing objectives, which shows the power transfer efficiency and power density cannot be maximized at the same time, and a trade-off has to be made according to the application scenarios. Later, this MOO method is applied to design a 50 kW IPT system with a DC-DC efficiency of 95.8 % at the aligned condition in [12]. It is common that there is a misalignment between the Tx and Rx pads when there are no aid-positioning devices, but the misaligned performances of IPT systems are not studied in [12, 35]. Although the misalignment is considered in the MOO method proposed in [36], the proposed optimal design is not experimentally validated. Therefore, the aim of this chapter is to propose a MOO method that considers both the aligned and misaligned performances of IPT systems, and also to verify the correctness of the optimal results in a prototype that delivers a leading power conversion efficiency metric when compared to IPT EV charging systems disseminated in today's literature.

Based on the Pareto fronts analysis in [36], the circular and rectangular pads outperform the polarized pads with respect to the power transfer efficiency under the same area-related power density. Under the condition that the area enclosed by the coil is the same, the circular coil outweighs the rectangular coil in terms of the magnetic coupling, but considering the available space in a practical application, the rectangular coil can cover a larger area and be more favorable than the circular coil instead [35]. Therefore, the rectangular configuration is selected for the design of the proposed 20 kW IPT system discussed in this chapter.

This chapter will first introduce the modeling method for calculating the power losses of the IPT system. The power losses in Litz wire, ferrite cores, and shielding plates are determined by the magnetic field distribution. Hence, the finite element (FE) models of the magnetic coupler are presented to derive the magnetic field properties to help the power loss evaluation. Then, a MOO method is presented to obtain Pareto fronts taking the power density, power efficiency and misalignment tolerance as objectives. Finally, an optimal design is selected based on the MOO results and a 20 kW IPT system is built to verify the proposed MOO method.

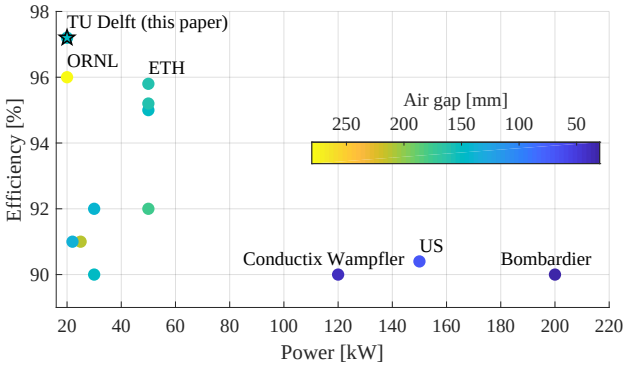

Figure 3.1: Performances of the state-of-art IPT systems recorded in Table 1.1.

3.2 Power Losses and Magnetic Field Modeling

3.2.1 Analytical Losses Model

To obtain the DC-DC efficiency of the IPT system, power losses should be modelled, including power converters (inverter and rectifier), capacitors and charging pads. The copper losses in the charging pads P_{cu} is composed of the DC ohmic loss P_{dc} and the AC losses due to the skin effect P_{skin}, internal P_{pin} and external P_{pex} proximity effects. According to [36], these power losses can be calculated as

$$\begin{cases} P_{\text{dc,i}} + P_{\text{skin,i}} = n_{\text{str}} r_{\text{dc}} F_{\text{R}}(f_{\text{s}}) \left(\dfrac{\widehat{I}_{\text{i}}}{n_{\text{str}}}\right)^2 L_{\text{coil}} \\ P_{\text{pin,i}} = n_{\text{str}} r_{\text{dc}} G_{\text{R}}(f_{\text{s}}) \dfrac{\widehat{I}_{\text{i}}^2}{2\pi^2 d_{\text{a}}^2} L_{\text{coil}} \\ P_{\text{pex,i}} = \displaystyle\sum_{k=1}^{N_{\text{i}}} n_{\text{str}} r_{\text{dc}} G_{\text{R}}(f_{\text{s}}) \oint_{l_{\text{k}}} \widehat{H}_{\text{ext}}^2(l) dl \end{cases} \tag{3.1}$$

where subscript $i = 1, 2$ stands for the Tx and Rx side, n_{str} is the number of strands in the litz wire, r_{dc} is the DC resistance per unit length of a single strand, $\widehat{I}_{\text{i}}$ is the peak value of the current through the coil, N_{i} is the number of turns of the coil, l_{k} is the k_{th} turn of the coil, d_{a} is the diameter of the litz wire, H_{ext} is the magnetic field penetrating the individual coil turns, f_{s} is the switching frequency, $F_{\text{R}}(f_{\text{s}})$ and $G_{\text{R}}(f_{\text{s}})$ are the frequency dependent factors [87]. The calculation of P_{pex} involves the geometric feature of the coil and H_{ext} over each individual coil turn which is derived from the FE models.

The ferrite core loss P_{fe} is calculated by using Steinmetz equation and integrating it over the core volume as [36]

$$P_{\text{fe,i}} = \int_{V_{\text{fe,i}}} k f_{\text{s}}^{\alpha} \widehat{B}^{\beta} dV \tag{3.2}$$

where subscript $i = 1, 2$ stands for the Tx and Rx side, V_{fe} is the set of cores for the coil, k, α and β are the Steinmetz parameters depending on the core material. For the selected core material 3C95, the Steinmetz parameters are $k = 92.66$, $\alpha = 1.045$ and $\beta = 2.44$ for W/m^3.

The shielding loss P_{sh} due to the eddy current is calculated by

$$P_{\mathrm{sh,i}} = \int_{V_{\mathrm{sh,i}}} \frac{\Re\{\mathbf{J}\cdot\mathbf{E}^*\}}{2} dV \tag{3.3}$$

where subscript $i = 1, 2$ stands for the Tx and Rx side, V_{sh} is the volume of the shielding plate, $\mathbf{J}$ is the induced current density amplitude on the shielding plate and $\mathbf{E}$ is the electric field at the surface boundary.

The film capacitor from TDK is selected for the 20 kW IPT system because its capacitance holds a relatively small deviation from its rated value for an operation at 85 kHz, while no critical de-rating due to hotspot caused by dielectric loss is necessary. The capacitor power loss is calculated by using the equivalent series resistance R_{cap} of each single unit as

$$P_{\mathrm{cap,i}} = I_{\mathrm{i}}^2 \frac{n_{\mathrm{s,i}}}{n_{\mathrm{p,i}}} R_{\mathrm{cap}} \tag{3.4}$$

where subscript $i = 1, 2$ stands for the Tx and Rx side, n_{s} and n_{p} are the number of capacitor units connected in series and in parallel, respectively. The selected film capacitor unit has a maximum AC voltage limit of 600 V. According to Fig. 2.12, the maximum voltage stress can be above 9 kV in RMS value at the misaligned case, which is far larger than the AC voltage limit of the capacitor unit. Thus, n_{s} has to be selected to ensure the voltage stress over a capacitor unit is less than its limit. Then, n_{p} is selected to achieve the design capacitance for the compensation according to (2.10). It should be noted that the total number of the capacitor units is proportional to n_{s}^2 because of $n_{\mathrm{p}} \propto n_{\mathrm{s}}$. Therefore, it becomes important for high power applications to reduce the voltage stress for a compact design.

The ZVS operation of the inverter can be attained by keeping the input impedance slightly inductive. For the synchronous rectification stage, the ZVS operation can be realized by applying a short delay between the zero-crossing of i_2 and the switching on of the MOSFETs operating in the following next half cycle. Therefore, the switching losses of the inverter and rectifier stages are negligible. The total semiconductor losses in the Tx $P_{\mathrm{sem,1}}$ and Rx sides $P_{\mathrm{sem,2}}$ can be approximated as conduction losses according to

$$P_{\mathrm{sem,i}} = I_{\mathrm{i}}^2 r_{\mathrm{DS,on}}\left(T_{\mathrm{j}}\right) \tag{3.5}$$

where subscript $i = 1, 2$ stands for the Tx and Rx side, $r_{\mathrm{DS,on}}$ is the equivalent on-state resistance of a single switch as a function of the junction temperature T_{j}.

Based on the presented losses calculation method, the equivalent AC resistance of the AC link R_{ac} can be obtained as

$$R_{\mathrm{ac,i}} = \frac{P_{\mathrm{cu,i}} + P_{\mathrm{fe,i}} + P_{\mathrm{sh,i}} + P_{\mathrm{cap,i}} + P_{\mathrm{sem,i}}}{I_{\mathrm{i}}^2} \tag{3.6}$$

where subscript $i = 1, 2$ stands for the Tx and Rx sides. As a vital part of improving the system power transfer efficiency, the optimal load for the SS compensated IPT system should be applied as (3.8). It should be noted that $R_{\mathrm{ac,i}}$ increases as the winding current becomes large, because the Steinmetz parameter β is larger than 2 according to (3.2) and (3.6). An accurate estimation of $R_{\mathrm{L,opt}}$ can only be conducted when the winding current is solved, while the winding current is determined by $R_{\mathrm{L,opt}}$. As a result, iterative steps

become necessary to accurately estimate the optimal operation condition. Since P_{dc} is a major part of the charging pad losses [12, 35] and involves no magnetic field computation, R_{ac} is simplified as

$$R_{\mathrm{ac,i}} \approx \frac{P_{\mathrm{dc,i}} + P_{\mathrm{cap,i}} + P_{\mathrm{sem,i}}}{I_{\mathrm{i}}^2} \tag{3.7}$$

to avoid the iterative procedure and reduce the computation labor for the calculation of the optimal operation conditions.

3.2.2 FE Model and Parameters

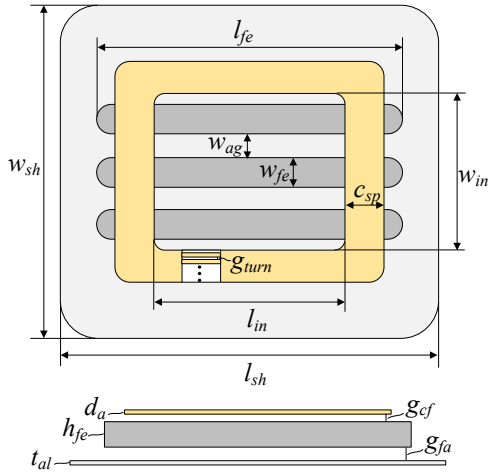

Figure 3.2: Geometrical variables for the charging pad. The width of the coil spread is $c_{\mathrm{sp}} = Nd_{\mathrm{a}} + (N-1)g_{\mathrm{turn}}$. To scale the length of the ferrite bar l_{fe} and the gap between ferrite bars w_{fe}, they are defined as $l_{\mathrm{fe}} = l_{\mathrm{fe,r}}(l_{\mathrm{in}} + 2c_{\mathrm{sp}})/100$, $w_{\mathrm{ag}} = w_{\mathrm{ag,r}}(w_{\mathrm{in}} + 2c_{\mathrm{sp}} - n_{\mathrm{fe}}w_{\mathrm{fe}})/(100(n_{\mathrm{fe}}-1))$, where $l_{\mathrm{fe,r}}$ and $w_{\mathrm{ag,r}}$ are the corresponding scaling factors. The shielding plate is set to have the same size as the coil, thus $l_{sh} = (l_{\mathrm{in}} + 2c_{\mathrm{sp}})$ and $w_{sh} = (w_{\mathrm{in}} + 2c_{\mathrm{sp}})$.

As the effective magnetic field is within the air gap between the Tx and Rx pads, the charging pads that produce a magnetic field concentrating on one side are preferred. To achieve the single-sided magnetic field, the charging pad usually consists of litz wire coil as well as ferrite cores, and the shielding plate. The ferrite cores could enhance the coupling between the Tx and Rx pads. The shielding plate is used to reduce the magnetic stray field. To obtain the electric parameters of the charging pads, including the self-inductance, mutual inductance and equivalent AC resistance, the magnetic field has to be calculated. Due to the non-linear property of the ferrite cores and various coil topologies, the magnetic field is commonly computed through finite element (FE) models [35, 36, 88].

The geometrical variables of the charging pads are illustrated in Fig. 3.2, where several identical ferrite bars in cuboid shape are applied. Thus, 3D FE models are required to calculate the magnetic field. To reduce the computation labor, the FE model utilizes a 3D solid block with uniform current density to model the winding as a whole instead of using pipes to model each turn of the winding. This can prevent the intensive computation load associated with the calculation of the eddy currents in the winding [36]. The diameter of

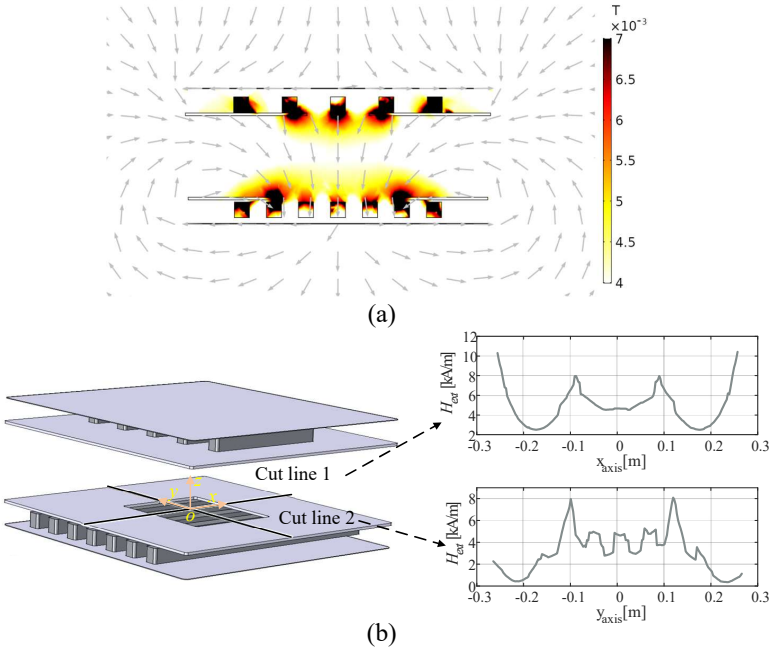

Figure 3.3: Magnetic field distribution computed by a 3D FE model simulated in COMSOL 5.4, (a) B field distribution in yz plane, (b) H field distribution along cut lines 1 and 2. Cut line 1 is along the x-axis and penetrates the center of each turn of the Tx coil. Cut line 2 is along the y-axis and penetrates the center of each turn of the Tx coil. The H field distribution is computed to calculate P_{pex} based on (3.1).

the litz wire strand is selected to eliminate the skin effect. The eddy current within the winding has a very limited impact on the magnetic field distribution. Thus, the 3D FE model can deliver reliable results of the inductance and H_{ext} that is used to calculate the proximity effect loss based on (3.1). An example of the magnetic field computed by a 3D FE model is illustrated in Fig. 3.3 where the B field distribution in the yz plane and the H field distribution in the cut lines 1 and 2 are illustrated. Fig. 3.3(b) shows that H_{ext} varies in a large range at different locations, and an obvious discontinuity emerges in the y-axis curve of H_{ext} due to the discrete deployment of the ferrite cores. Therefore, H_{ext} at multiple different points of each coil turn are computed to improve the accuracy when calculating P_{pex} based on (3.1).

In this FE model, the gap between the coil turns g_{turn} is included and a non-zero lower boundary is set. The advantages are 1) less proximity effect losses, 2) available space for the insulation wrapper of the litz wire, 3) lower parasitic capacitance between adjacent coil turns and 4) higher heat dissipation capability. The FE model also includes the gap between the coil and ferrites g_{cf} to consider the physical presence of the litz wire wrapper and to reduce the impact of the spikes of magnetic field concentrated at the edges of the ferrite cores on the winding [36]. Also, the gap between the ferrite cores and the shielding plates g_{fa} is considered. Due to the non-polarized field distribution of the rectangular coil, the shielding plates tend to have considerable eddy current losses when g_{fa} is minimal.

The investigation on g_{fa} could be helpful in improving the efficiency of the charging pad.

3.2.3 System Topology and Load Matching Method

Given the mutual coupling constant, the maximum efficiency is determined by the load condition as discussed in Section III. The load matching can be realized by applying a semi-active rectifier [81] or an active rectifier [89]. By changing the phase-shift angle of the active rectifier, the amplitude and the phase of the load impedance are controlled separately [89], which is not suitable for high power IPT applications due to the switching losses. It is more practical to apply the synchronous rectification technique on the active rectifier, which is proved to be more efficient than the diode bridge rectifier [90] but cannot effectively regulate the load. Therefore, a back-end DC-DC converter becomes necessary to change the load impedance [81]. Due to the current source output characteristics of the SS compensated IPT system, the output power regulation at a fixed battery voltage can be realized by adding a front-end DC-DC converter which will enable this functionality by adjusting the resonant circuit's input voltage. The power factor correction (PFC) stage can also provide the power regulation in a certain output voltage range by the same means, and without the need of the front-end DC-DC converter. An overview of the target IPT system is presented in Fig. 3.4. The advantage of applying the PFC stage and back-end DC-DC converters for the load matching and power regulation is that the resonant circuit can operate at a very narrow-band frequency close to minimum switching losses in the inverter and rectifier stages.

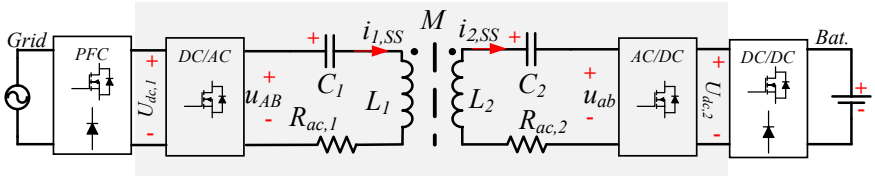

Figure 3.4: IPT system overview for battery charging applications.

The target of this chapter is to design a 20 kW IPT system with $U_{\mathrm{dc,max}} = 850\mathrm{V}$. With a 3ϕ 400 V line-to-line European grid connection, the PFC can safely supply a DC voltage up to 870V with conventional two- or three-level voltage source converters, and the DC voltage requirement can be satisfied. For the Rx side, the traction battery voltage is commonly around 400V for the light-duty EVs, and a back-end buck converter becomes necessary. However, the battery voltage increases to 800V for electric buses due to the higher demand for traction power [91]. Thus, it is also viable to remove the back-end DC-DC converter for the battery charging of electric buses. To focus more on the AC link design, the DC-DC converter is not studied in this chapter. As highlighted in Fig. 3.4, the studied IPT system includes the inverter, AC link and rectifier.

Provided the alignment condition and ω_{s} is fixed, the AC equivalent optimal load resistance is determined as [36]

$$R_{\mathrm{L,opt}} \approx \omega_{\mathrm{s}} M \sqrt{\frac{R_{\mathrm{ac,2}}}{R_{\mathrm{ac,1}}}} \tag{3.8}$$

where $R_{\mathrm{ac,i}}$ (subscript = 1, 2 stands for the Tx and Rx sides of the IPT system, respectively) is the equivalent AC resistance of the AC link. To achieve the maximum system efficiency, the DC voltage $U^*_{\mathrm{dc,i}}$ under rated output power can be estimated as

$$\begin{cases} U^*_{\mathrm{dc,2}} \approx \dfrac{\pi}{4}\sqrt{2P_{\mathrm{out}}\omega_{\mathrm{s}}M}\sqrt[4]{\dfrac{R_{\mathrm{ac,2}}}{R_{\mathrm{ac,1}}}} \\ U^*_{\mathrm{dc,1}} \approx \dfrac{\pi}{4}\sqrt{2P_{\mathrm{out}}\omega_{\mathrm{s}}M}\sqrt[4]{\dfrac{R_{\mathrm{ac,1}}}{R_{\mathrm{ac,2}}}} \end{cases} \tag{3.9}$$

3

3.3 Multi-Objective Optimization

Table 3.1: Design requirements of the system

Items	Symbol	Unit	Value
Output power	P_{out}	kW	20
Air gap distance	δ	mm	150
Operation frequency	f_{s}	kHz	85
DC voltage limit	$U_{\mathrm{dc,max}}$	V	850
Lateral misalignment	Δx	mm	150

The objectives of the optimization are to maximize the power transfer efficiency under aligned η_{al} and misaligned η_{mis} conditions, and the power density in terms of the Rx pad area ρ_{A} and total weight of the coupler ρ_{G}. The design requirements of the IPT system are listed in Table 3.1. The air gap distance and operating frequency are selected to comply with the SAE J2954 standard [50]. For the SS compensated IPT system, when the losses in the compensation capacitors are much less than the charging pads, the maximum efficiency η_{max} of the IPT system increases when FOM becomes large as [27]

$$\eta_{\mathrm{max}} = \frac{FOM_1 FOM_2}{(1+\sqrt{1+FOM_1 FOM_2})^2} \tag{3.10}$$

where subscript = 1, 2 stands for the Tx and Rx sides. Eq. (3.10) proves that increasing the magnetic coupling can improve the power efficiency of an IPT system. Correspondingly, the DC voltage limit has to be increased to transfer the rated power based on (3.9). Meanwhile, the battery voltage for electric passenger vehicles can reach above 800 V [91]. Therefore, the DC voltage limit is selected to be 850 V. The lateral misalignment is set to be 150 mm which is larger than the recommended misalignment test value 100 mm in the SAE J2954 standard [50]. The design variables and their search space are listed in Table 3.2.

For each set of a feasible design of magnetic coupler, the performance of the IPT system is computed according to Fig. 3.5. The steps are as follows:

- Step 1: Build a 3D symmetrical FE model to extract the self-inductances, DC ohmic resistances, and aligned mutual inductance of the magnetic coupler.
- Step 2: Calculate $R_{\mathrm{L,opt}}$, $U^*_{\mathrm{dc,1}}$ and $U^*_{\mathrm{dc,2}}$ using the DC ohmic resistances and mutual inductance according to (3.8) and (3.9). The winding currents can be calculated according to (2.12).

Table 3.2: Design variables and search space

Variables	Symbol	Unit	Range
Number of turns	N	-	10-35
Number of ferrites	n_{fe}	-	5-9
Inner length	l_{in}	mm	25-300
Inner width	w_{in}	mm	25-300
Ferrite thickness	h_{fe}	mm	5-35
Ferrite width	w_{fe}	mm	15-45
Relative ferrite length	$l_{\mathrm{fe,r}}$	%	50-150
Relative gap between ferrites	$w_{\mathrm{ag,r}}$	%	10-100
Gap between coil and ferrites	g_{cf}	mm	0.1-5
Gap between ferrites and shielding	g_{fa}	mm	1-20
Gap between coil turns	g_{turn}	mm	1-3

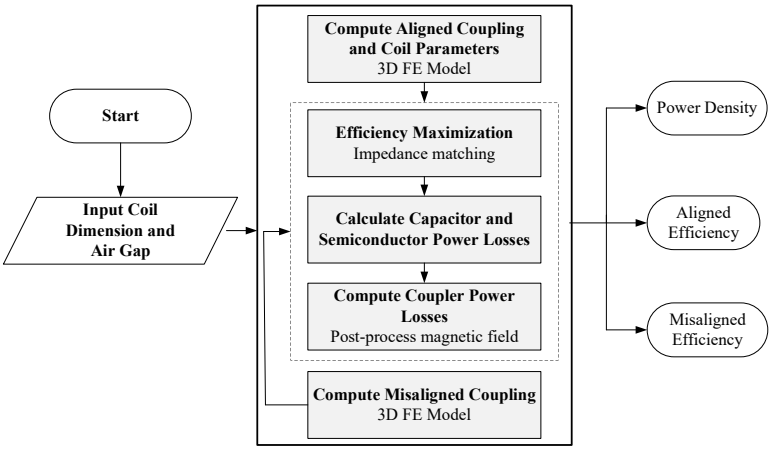

Figure 3.5: Computation flowchart for a specific design of magnetic coupler in the optimization loop.

- Step 3: Analyze the power losses of the compensation capacitors according to (3.4), and the inverter and rectifier according to (3.5).
- Step 4: Apply the winding currents to a 3D FE model to compute the magnetic field and calculate the power losses of the magnetic coupler analytically according to (3.1), (3.2) and (3.3).
- Step 5: Compute the misaligned mutual inductance and repeat Step 2-4.
- Step 6: Calculate the power density, aligned and misaligned power efficiency.

The optimization results are presented in Fig. 3.6 and 3.7 where each point represents a unique design of the IPT system. η_{al} and η_{mis} include the power losses in the power converters, compensation capacitors and charging pads. η_{mis} is calculated when the lateral offset Δx is 150 mm. For the SS compensated IPT system, the winding current stress

increases as the coupling declines due to the offset. The winding current density is limited below 5A/mm^2 for the thermal safety. The maximum magnetic field density in the ferrites is set to be 350 mT to avoid the saturation of the ferrite cores. The color of points indicates *FOM* of each design. A trade-off emerges between the power transfer efficiency and the power density. A trend can be seen that decreasing the power density, by increasing either the total weight or the Rx pad surface area, can improve the power transfer efficiency.

As proved by (3.10), $\eta_{\max}$ becomes higher as the *FOM* increases. Given that f_s is fixed, one of the ways to improve *FOM* is to increase the coil number of turn N for a higher coil quality factor Q. It is because $R_{\mathrm{dc,i}} \propto N_{\mathrm{i}}$ and $L_{\mathrm{i}} \propto N_{\mathrm{i}}^2$. This can explain why designs with lower ρ_{G} could reach a larger *FOM* and also a higher η_{al}, which is shown in Fig. 3.6(a) and 3.7(a). However, as Q goes high, the losses in the compensation capacitors become comparable with that of the charging pads. It is reported in [35] that the calculated loss in the capacitor is comparable with that in charging pads. The power loss factor $tan\delta$ of commercial film capacitors can be 0.2%. In that case, the charging pad with Q above 500 theoretically produces less power loss than the corresponding compensation capacitor. As a result, designs with high Q using more copper to gain a higher *FOM* cannot always guarantee a higher efficiency.

FOM can also be improved by applying more ferrite cores. As shown in Fig. 3.8(b), the average magnetic field density B_{avg} within the ferrite cores decreases as the weight percentage of the ferrite cores p_{fe} increases. It suggests a lower ferrite core loss density according to (3.2). As per Fig. 3.8(a), η_{al} generally increases as a higher p_{fe} is applied when M is approximately the same. On one hand, designs with a higher p_{fe} tend to have a lower B_{avg} and less amount of copper, implying a lower R_{ac}. On the other hand, the winding currents are decided by M based on (2.23). Thus, it is advantageous to increase the usage of ferrites to reach a large M whose feasible range is decided by the DC voltage limit as

$$M \leq \frac{8U_{\mathrm{dc,max}}^2}{\pi^2 \omega_{\mathrm{s}} P_{\mathrm{out}}} \tag{3.11}$$

When M is beyond the range in (3.11), the IPT system is incapable of delivering the rated power.

Based on the Pareto fronts in Fig. 3.6 and 3.7, a design with $\rho_{\mathrm{G}} = 0.84$ kW/kg and $\rho_{\mathrm{A}} = 0.69$ kW/dm^2 is chosen and highlighted with a star. The highlighted design is on the Pareto fronts in Fig. 3.6 with a high aligned efficiency of 97.5%. Under the misaligned condition, this design delivers an efficiency of 94.1% which is close to but not on the Pareto front of Fig. 3.7. When comparing Fig. 3.6 and 3.7, the maximum value of *FOM* generally drops by half due to the decreased coupling caused by the misalignment. To improve the misalignment coupling, charging pads with a larger area and more cost of material are preferred, thus resulting in a noncompetitive *FOM*. Consequently, a trade-off might be made between η_{al} and η_{mis}. Since the design target is the static charging application, the misalignment between the Tx and Rx pads is commonly within a narrow range, so it is prioritized to have a high η_{al}. Besides, the size of the Rx pad is 544.8mm $*$ 562.7mm which is also acceptable. Thus, the highlighted design is selected for prototyping.

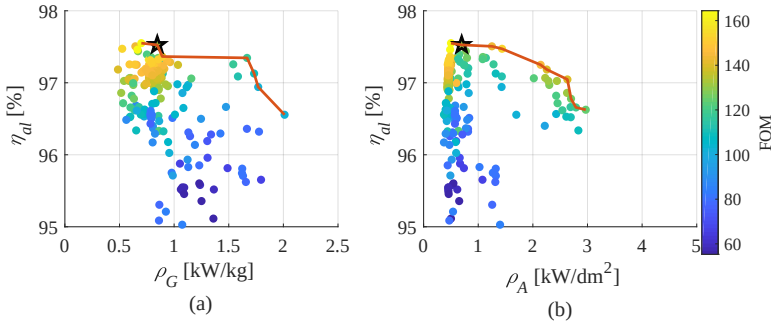

Figure 3.6: Pareto optimal fronts between η_{al} and (a) ρ_{G} and (b) ρ_{A} with the color indicating the value of *FOM*.

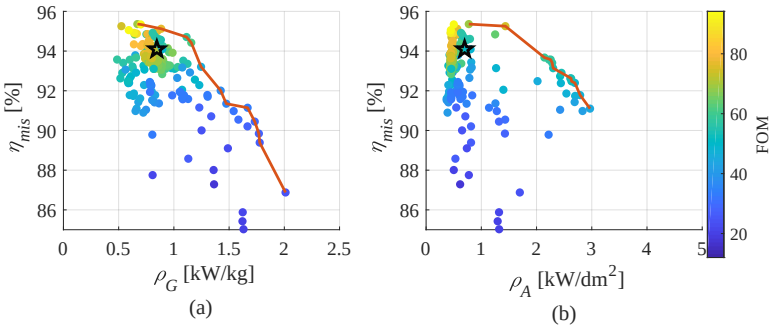

Figure 3.7: Pareto optimal fronts between η_{mis} and (a) ρ_{G} and (b) ρ_{A} with the color indicating the value of *FOM*.

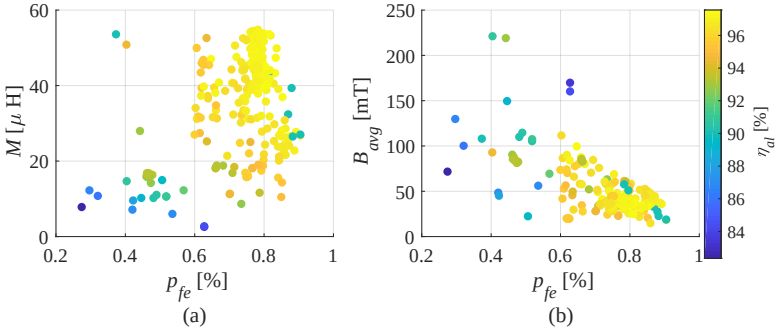

Figure 3.8: Influence of p_{fe} on (a) M and (b) B_{avg} with the color indicating η_{al}.

3.4 Experimental Verification

To verify the performance of the optimal design, an IPT system is built, consisting of the full-bridge inverter and rectifier, the compensation capacitor boards, and the Tx and Rx pads, as depicted in Fig. 3.9. The DC-DC power transfer efficiency is measured under the aligned and 150 mm lateral misalignment conditions.

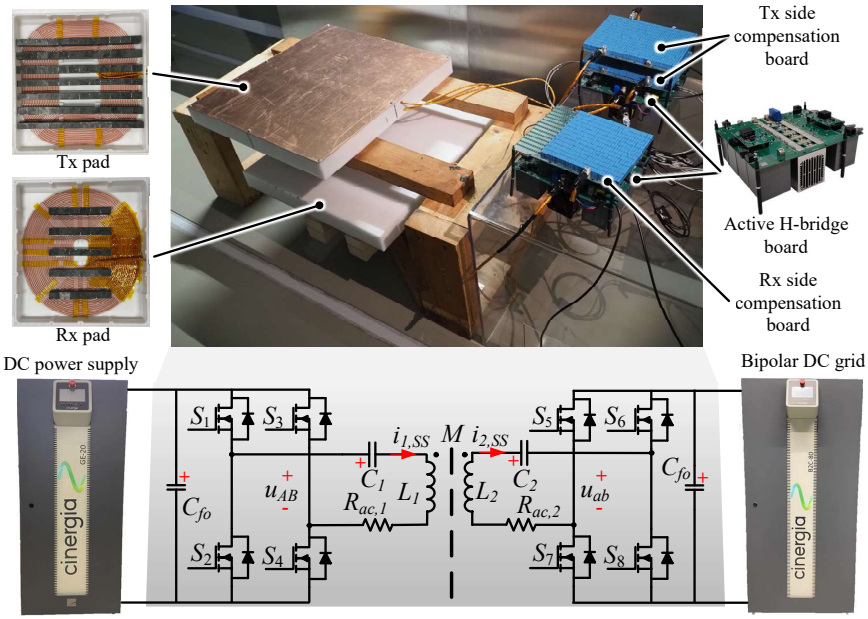

Figure 3.9: Pictures and circuit schematics of the developed IPT system.

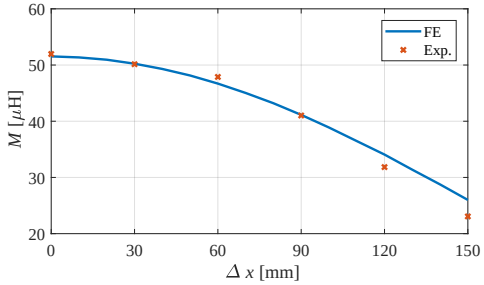

Figure 3.10: Comparison of M obtained from FE models and experiments.

3.4.1 Accuracy of FE Models

The specifications of the optimal design are illustrated in Table 3.3. The structure of the charging pads is presented in Fig. 3.9, where the copper shielding plates are removed. According to the size of the Rx pad, the prototype has an area power density of 69.1 kW/m^2. The protective housing is made of polyoxymethylene (POM). The thickness of the bottom and wall of the POM housing is designed to be 10 mm for minimal deformation while supporting the weight of the litz wire and ferrite cores. To reduce the fabricating labor, channels are milled in the POM housing to guide the litz wire. The barriers of channels can improve the insulation level between adjacent coil turns and the height is used to maintain the gap between the coil and ferrite cores. The strand diameter of the litz wire is selected to be 71 μm to minimize the skin effect at 85 kHz. To limit the current density through

Table 3.3: Specifications of the selected design

Variables	Symbol	Unit	Tx/Rx
Number of turns	N	-	23/31
Number of ferrites	n_{fe}	-	7/5
Inner length	l_{in}	mm	184.7/66.2
Inner width	w_{in}	mm	220.8/114.2
Ferrite thickness	h_{fe}	mm	28.8
Ferrite width	w_{fe}	mm	27.7
Ferrite length	l_{fe}	mm	515.3/243.1
Gap between ferrites	w_{ag}	mm	41.8/69.3
Gap between coil and ferrites	g_{cf}	mm	3.9/1
Gap between ferrites and shielding	g_{fa}	mm	10.6/15.0
Gap between coil turns	g_{turn}	mm	2.2

the coils, the litz wire has 2200 strands. It is shown in Fig. 2.12 that the voltage stress can reach around 8 kV which is the voltage between the inner turn and the outer turn of the charging pads. Thus, special attention is paid to the insulation of the litz wire segment stretching from the inner turn to the edge of the POM housing, and extra insulation tape is wrapped on this litz wire segment, as shown in Fig. 3.9. The charging pad dimension and the total weight including the housing material are $516 * 552 * 60$ mm^3/25 kg for the Tx side and $514 * 562 * 60$ mm^3/21 kg for the Rx side. Correspondingly, the gravimetric and volumetric power density are 0.435 kW/kg and 581 kW/m^3, respectively.

The comparison of M between the FE models and experiments is depicted in Fig. 3.10. The maximum relative error is 12% and occurs at 150 mm lateral offset. Considering the possible spatial location error, the difference between the measurements and FE analysis is mostly acceptable. L_1 and L_2 are measured to be 292.3 μH and 199.6 μH, respectively. Based on the tuning method in (2.10), C_1 and C_2 are designed to be 11.99 nF and 17.57 nF. Each capacitor unit has 6.7 nF and 400 V rms limit. Considering the rms voltage limit of 8 kV, the capacitor boards are designed as $n_{\mathrm{s},1} = 26$, $n_{\mathrm{p},1} = 45$, $n_{\mathrm{s},2} = 13$ and $n_{\mathrm{p},2} = 34$.

3.4.2 Power Transfer Efficiency

According to the load matching method described in Section IV, the output power is regulated by changing $U_{\mathrm{dc},1}$ while $U_{\mathrm{dc},2}$ is controlled by a back-end DC-DC converter to achieve load matching for the maximum efficiency. Since the DC-DC converter design may change for EVs with different battery voltages, the DC-DC power transfer efficiency discussed in this chapter does not include the PFC front-end circuit and back-end DC-DC converter. To test the performance of the designed prototype, the DC power supply (CINERGIA GE20) is used to provide the DC power with the voltage range of $0-750$V. The bipolar DC grid (CINERGIA B2C80) with the voltage range of $0-1500$ V and the current range of $0-41$ A is utilized as an electronic load with regenerative power injection. The DC grid is controlled to operate as a constant electronic resistor which is set to be 34 Ω and 15 Ω for the aligned and misaligned conditions, respectively.

The full-bridge converter and series compensation circuit are illustrated in Fig. 3.11.

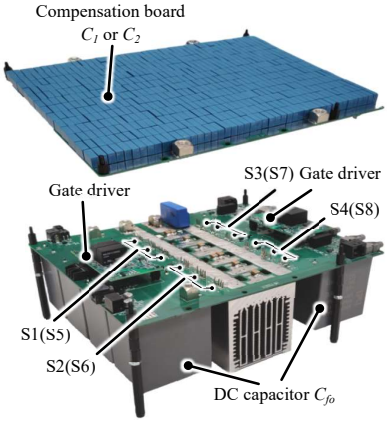

Figure 3.11: Full-bridge converter with the series compensation capacitor board.

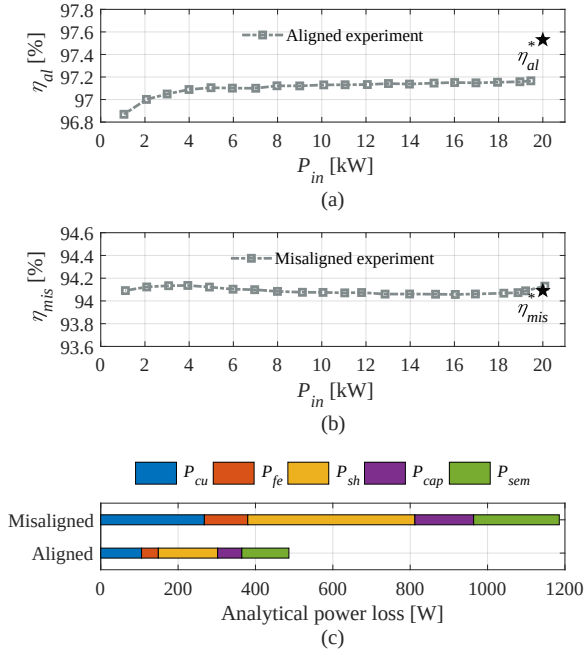

Figure 3.12: Measured power transfer efficiency at different power levels under (a) aligned and (b) misaligned conditions, and (c) power losses calculated by using the proposed analytical losses model at 20 kW P_{in}.

The Tx and Rx sides use identical full-bridge converters, but different series compensation capacitor boards. Considering the high operating frequency of 85 kHz, the commercially available SiC MOSFETs IMZ120R030M1H rated to a maximum blocking voltage of 1200 V and maximum recommended constant current of 56 A is used. At 25 °C, the on-state resistance is 30 mΩ. To reduce the conduction losses, three MOSFETs are connected in

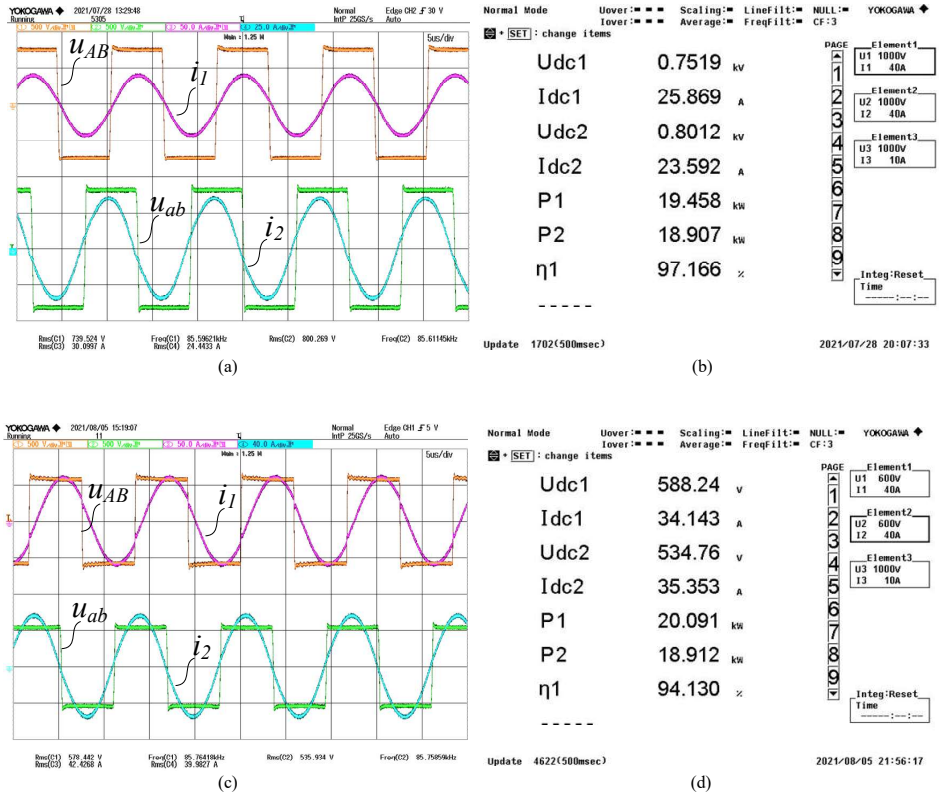

Figure 3.13: Measured waveforms and power transfer efficiency at the rated power under (a) and (b) aligned, (c) and (d) misaligned conditions.

parallel for each functional switch of the full bridge converter.

By adjusting $U_{\mathrm{dc},1}$, the power transfer efficiency with P_{in} ranging from $1-20$ kW is presented in Fig. 3.12(a) and 3.12(b). The DC-DC power transfer efficiency is measured by a power analyser (YOKOGAWA WT500). As shown in Fig. 3.12(a), η_{al} increases from 96.9% to 97.2% as P_{in} increases from 1kW to 20 kW. The designed aligned efficiency η^*_{al} is 97.5% which is just 0.3% higher than the measurement at 20kW. The power transfer efficiency under misaligned conditions is shown in Fig. 3.12(b), where η_{mis} fluctuates in a small range. At the rated operation condition, η_{mis} is 94.1% which is almost equal to the designed value η^*_{mis}. The analytical power losses of different components at 20 kW P_{in} is depicted in Fig. 3.12(c). The major part of the power losses is P_{sh}, followed by P_{cu} and P_{sem}.

The measured waveforms and power transfer efficiency at the rated power are illustrated in Fig. 3.13. It can be seen in both Fig. 3.13(a) and 3.13(c) that u_{AB} leads i_1 by a certain degree, thus ensuring the ZVS operation of the full-bridge inverter. It should be noticed that the angle of the input impedance is larger in Fig. 3.13(c), because L_1 increases slightly from 292.3 μH to 300.7 μH due to the misalignment.

3.5 Conclusions

This chapter has presented the detailed design guideline and demonstration of a highly efficient 20 kW IPT system. The developed prototype has a higher efficiency under the aligned and misaligned condition than the 20kW+ IPT systems used for the charging of EVs in the IEEE literature. To provide a clear guideline on the system design, the optimization of the charging pads is detailed. To find the optimal design of the charging pads, a MOO design method is presented. The MOO design involves both the analytical and FE models to calculate the power losses of the IPT system. Taking the aligned/misaligned efficiency and area/gravimetric power density as the objectives, the optimal Pareto fronts are obtained, and a design theoretically delivering an aligned efficiency of 97.5% and a misaligned efficiency of 94.1% is selected for prototyping. Finally, a prototype with an area power density of 69.1 kW/m^2 is built. The efficiency is measured to be 97.2% at the aligned condition and 94.1% at the misaligned condition.

4

Dynamic Modeling and Control

Resonant circuits are commonly used in inductive power transfer (IPT) systems for the charging of electric vehicles because of their high power efficiency. Transient behaviors of the resonant circuits, which play a significant role in the design and analysis of IPT systems, are cumbersome to model analytically because of the high order. This article develops a reduced-order continuous dynamic model based on the energy interactions among the resonant tanks. By applying the proposed energy balancing method (EBM), the order of the dynamic model is reduced to half of the number of the passive components in the resonant circuits. To show the accuracy of the EBM, the dynamics of a series–series (SS) compensated IPT system is modeled using Laplace phasor transformation (LPT) and EBM separately and the results are compared. The order of the EBM is found to be one-fourth of that of the LPT method. The sensitivity of the EBM to the switching frequency is discussed when the zero voltage switching turn-on operation is attained. Besides, to prove the advantage of reducing the order of the dynamic model, model predictive controls (MPCs) based on EBM and LPT are developed. The transient performances of the MPC controllers are simulated and the control inputs are applied to an experimental setup. Finally, experiments are conducted to verify the accuracy of the proposed EBM under zero and nonzero conditions and the effectiveness of the developed MPC controller.

This chapter is based on:

- W. Shi, J. Dong, T. B. Soeiro, J. Deng, C. Riekerk, P. Bauer, *"Continuous Reduced-Order Dynamic Model Based on Energy Balancing for Inductive Power Transfer Systems"*, *IEEE Transactions on Power Electronics*, 37(8):9959-9971.

4.1 Introduction

In dynamic IPT (DIPT) systems, several transmitter pads (Tx) are mounted under the road, allowing EVs to pick up power while they are moving. Thus, the driving range of EVs can be extended. One of the main challenges of the DIPT application is the common variation of the mutual coupling between Tx and the EV receiver pad (Rx) due to the misalignment caused by the EV movement, i.e., as the EV moves toward the perfect alignment condition the mutual coupling changes from the minimum to the maximum [37, 92, 93]. Consequently, the operation state of the power electronic converters will continuously change and the power picked up by the EV battery charger may fluctuate. Also, the start-up transients of the IPT systems should be regulated to avoid any over-current or -voltage problems [94, 95]. Moreover, the disturbances in the DC source may lead to an unstable output of the IPT systems. To address these dynamic challenges, it is essential to have a dynamic model for the design of IPT systems.

Due to the presence of switching converters, the instantaneous model of the IPT system is discontinuous and time-variant. To study a specific design, the instantaneous model can be processed numerically to evaluate its dynamic characteristics [39]. However, the instantaneous model offers limited insights into the design of the feedback controller and the optimization of the resonant circuit components. To overcome the discontinuity and time-variance of the instantaneous model and to derive analytic solutions, the oscillating state variables can be transformed into slowly varying variables, based on the short-time Fourier transform. Existing studies report dynamic modeling methods including generalized state-space averaging (GSSA) [40, 41], Laplace phasor transformation (LPT) [42–44], extended describing function (EDF) [45] and coupled model theory (CMT) [46, 47]. However, these methods cannot deliver a dynamic model simple enough for researchers to gain insights into the transient behaviors of an IPT system [44]. Besides, it obstructs the applications of control strategies where the analytical dynamic model is required. The model predictive control (MPC), a discrete optimal control strategy, applies the system analytic model to periodically predict its future behaviors. The MPC is insensitive to disturbances [96] and can provide fast dynamic response [97]. Since the continuous dynamic model of the IPT systems is complex, the MPC is mainly designed based on the static model of the AC link to control the H-bridge converters [98] or based on the dynamic model of the DC-DC converters to control the secondary side converter. Without the dynamic model of the AC-link, these control methods cannot improve the transient behaviors inside the AC-link, which may cause a large overshoot.

In summary, the existing dynamic modeling methods can only deliver continuous dynamic models whose order is equal to or higher than the number of passive components. To simplify the transient analysis and facilitate the application of control strategies relying on the analytical system model, it becomes essential to describe IPT systems using a continuous, time-invariant, and low-order state-space model. Therefore, this chapter proposes a new dynamic modeling approach - an energy balancing method (EBM) based on the energy interactions between the resonant tanks for loosely coupled IPT systems using SS capacitive compensation. The order of the dynamic model using EBM is half the number of the passive components in the resonant circuits. A MPC controller is developed to prove the advantage of the proposed EBM.

This chapter first introduces the derivation of the EBM for various resonant tanks. Then,

the proposed EBM is compared with the LPT method in analyzing the transient behavior of a SS compensated IPT system. It is shown that the order of the resonant circuits dynamic model using the EBM is one-fourth that of the resulting model derived with the LPT. The sensitivity of the EBM to the switching frequency of the inverter is also discussed. Later, the MPC controllers based on the EBM and LPT methods are developed and their transient behaviors are compared. Finally, experiments are conducted to verify the accuracy of the dynamic models using EBM and the effectiveness of the developed MPC controller.

4.2 Dynamic Modeling Method Based on Energy Balancing

In this section, the energy balancing model of the LC and coupled LC resonant tanks are derived.

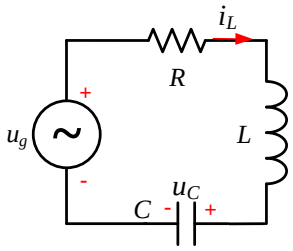

Figure 4.1: LC resonant tank.

4.2.1 Energy of A LC Resonant Tank

The LC resonant tank is presented in Fig. 6.2. The resonant frequency of the LC tank ω_s is

$$\omega_s = \frac{1}{\sqrt{LC}} \tag{4.1}$$

The LC circuit operating under resonance can be modeled as

$$\begin{bmatrix} i'_L \\ u'_C \end{bmatrix} = \begin{bmatrix} -\frac{R}{L} & -\frac{1}{L} \\ \frac{1}{C} & 0 \end{bmatrix} \begin{bmatrix} i_L \\ u_C \end{bmatrix} + \begin{bmatrix} \frac{1}{L} \\ 0 \end{bmatrix} u_g \tag{4.2}$$

where the prime in the symbols represents the time differential. To investigate the step response of the LC tank, the voltage source $u_g = U_g \cos(\omega t)$ is applied at t_0, where U_g is constant. Provided $R < 2\omega_s L$, the state-space model in (6.2) can be solved as

$$i_L = U_g \frac{1}{R} \cos(\omega_s t) + e^{-\frac{R}{2L}t} \left(\frac{i_L(0)R - U_g}{R} \cos\left(\frac{H}{2L}t\right) - \frac{i_L(0)R + 2u_C(0) - U_g}{H} \sin\left(\frac{H}{2L}t\right) \right) \tag{4.3}$$

$$u_C = U_g \frac{\omega_s L}{R} \sin(\omega_s t) + e^{-\frac{R}{2L}t} \left(u_C(0) \cos\left(\frac{H}{2L}t\right) + \frac{2{\omega_s}^2 L^2 (i_L(0)R - U_g) + u_C(0)R^2}{RH} \sin\left(\frac{H}{2L}t\right) \right) \tag{4.4}$$

$$H = \sqrt{4{\omega_s}^2 L^2 - R^2} \tag{4.5}$$

As shown in (6.3) and (6.4), the decay rate of the state variables is $\tau_{LC} = -\frac{R}{2L}$. By increasing R, the LC resonant tank can rapidly reach a steady state, and the transients can be mostly neglected. Given $R = \omega_s L$, for example, the transient components in (6.3) and (6.4) decay to below 5% within one switching cycle. In contrast, the transient response of the LC tank deteriorates as R decreases. When $R << \omega_s L$, $H \approx 2\omega_s L$, and the solutions under zero conditions become

$$i_L \approx U_g \frac{1}{R} \cos(\omega_s t)(1 - e^{-\frac{R}{2L}t}) \tag{4.6a}$$

$$u_C \approx U_g \frac{\omega_s L}{R} \sin(\omega_s t)(1 - e^{-\frac{R}{2L}t}) \tag{4.6b}$$

The total energy in the LC resonant tank W_{LC} is

$$W_{LC} = \frac{1}{2} L i_L^2 + \frac{1}{2} C u_C^2 \tag{4.7}$$

By substituting (6.6) to (6.7), the time domain solution of W_{LC} under resonance can be obtained

$$W_{LC} = \frac{L U_g^2}{2R^2}(1 + e^{-\frac{R}{L}} - 2e^{-\frac{R}{2L}}) \tag{4.8}$$

As per in (6.8), W_{LC} is a slow-varying positive variable that does not contain any oscillating component. Meanwhile, (6.6) proves that i_L peaks when u_C becomes zero, which means the total energy of the LC tank is stored in the inductor as i_L reaches the peak, and vice versa. Therefore, the amplitude of i_L and u_C, I_L and U_C, can be expressed as (6.9). By introducing (6.9), I_L and U_C can be calculated by solving W_{LC} instead of i_L and u_C which are cumbersome to solve due to their oscillating nature.

$$I_L = \sqrt{\frac{2W_{LC}}{L}}, U_C = \sqrt{\frac{2W_{LC}}{C}} \tag{4.9}$$

4.2.2 Energy Balancing Model for A LC Resonant Tank

The energy injected from the voltage source will either increase W_{LC} or be consumed by the load. The phase angle between u_g and i_L is negligible as per (6.6). Thus, based on the balance of energy, the LC resonant tank can be modeled as

$$W'_{LC} = L I_L I'_L = \frac{1}{2} U_g I_L - \frac{1}{2} I_L^2 R \tag{4.10}$$

Based on (6.10), the dynamic model of the LC resonant tank using the EBM can be derived

$$I'_L = -\frac{R}{2L} I_L + \frac{1}{2L} U_g \tag{4.11}$$

U_C can be obtained from (6.9). Compared with the dynamic model in (6.2), the model applying the EBM in (6.11) applies the amplitude of the oscillating variable to model the LC resonant tank instead of the oscillating variables themselves. As a result, the order of the dynamic model is reduced by half and the state variables are real-value.

4.2.3 Energy Balancing Model for Two Coupled LC Resonant Tanks

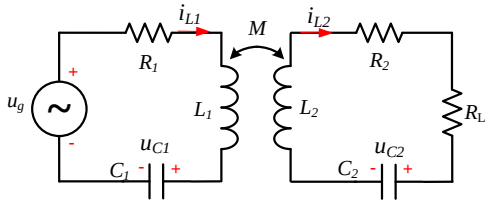

Figure 4.2: Two coupled LC resonant tanks.

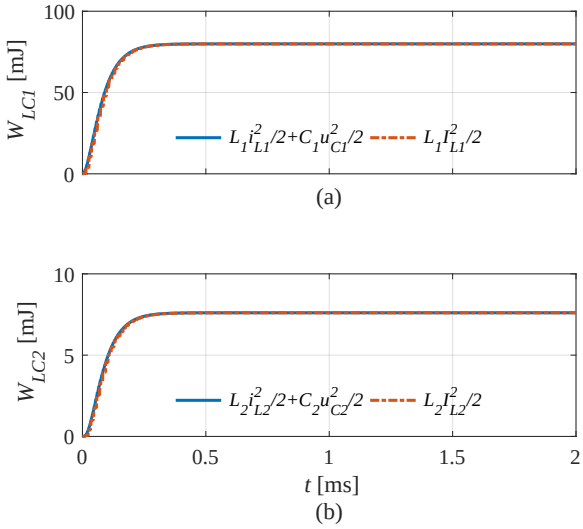

Figure 4.3: The total energy stored in the LC resonant tanks during transients, (a) LC1 and (b) LC2, where $L_1 = 63.35\mu$H, $L_2 = 43.53\mu$H, $M = 6.1\mu$H, $R_1 = 0.2\Omega$, $R_2 = 0.3\Omega$, and $R_L = 20\Omega$.

The EBM can also be applied to model two coupled LC resonant tanks, L_1C_1 (as LC1) and L_2C_2 (as LC2), as shown in Fig. 6.3. Fig. 6.4 presents agreement between the total energy calculated based on the instantaneous winding current and the capacitor voltage, and the amplitude of the winding current. This means the phase angle between i_{L1} (i_{L2}) and u_{c1} (u_{c2}) maintains to be $\frac{\pi}{2}$ as in (6.6). Assuming that the resonant frequency of both resonant tanks is equal to ω_s, the energy of the resonant tanks can be expressed as

$$W_{LC1} = \frac{1}{2} L_1 I_{L1}^2 \tag{4.12a}$$

$$W_{LC2} = \frac{1}{2} L_2 I_{L2}^2 \tag{4.12b}$$

In EV charging applications employing IPT systems, the presence of an air gap between charging pads causes the coupling coefficient to be relatively low. Thus, the phase angle between u_g and i_{L1} can be neglected as proved by (6.6). The energy interaction between LC1 and LC2 can be calculated with

$$W'_{LC1} = L_1 I_{L1} I'_{L1} = \frac{1}{2} U_g I_{L1} - \frac{1}{2} I_{L1}^2 R_1 - \frac{1}{2} \omega_s M I_{L1} I_{L2} \tag{4.13a}$$

$$W'_{LC2} = L_2 I_{L2} I'_{L2} = \frac{1}{2} \omega_s M I_{L1} I_{L2} - \frac{1}{2} I_{L2}^2 (R_L + R_2) \tag{4.13b}$$

where I_{L1} and I_{L2} are the amplitude of i_{L1} and i_{L2}, respectively. Based on (4.13a) and (4.13b), the dynamic model using EBM can be obtained

$$\begin{bmatrix} I'_{L1} \\ I'_{L2} \end{bmatrix} = \begin{bmatrix} -\frac{R_1}{2L_1} & -\frac{\omega_s M}{2L_1} \\ \frac{\omega_s M}{2L_2} & -\frac{(R_2+R_L)}{2L_2} \end{bmatrix} \begin{bmatrix} I_{L1} \\ I_{L2} \end{bmatrix} + \begin{bmatrix} \frac{1}{2L_1} \\ 0 \end{bmatrix} U_g \tag{4.14}$$

The solutions from the instantaneous model and EBM are presented in Fig. 6.5, where the amplitude of waveforms obtained from EBM matches the envelopes of waveforms from the instantaneous model.

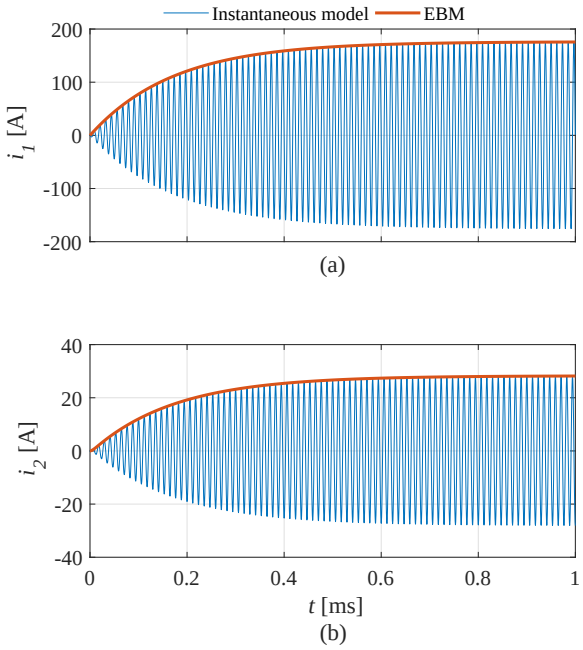

Figure 4.4: Time domain solutions of two coupled LC resonant tanks from the instantaneous model and EBM, where $U_g = 100$V and the circuit parameters are the same as Fig. 6.4.

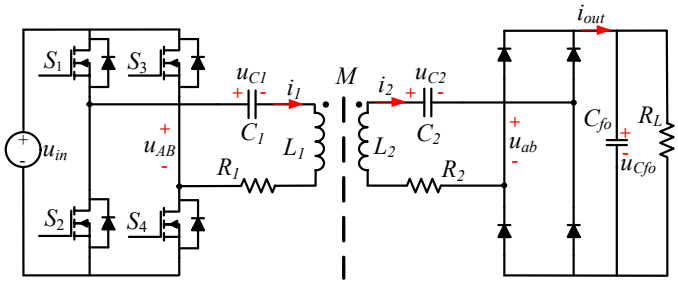

Figure 4.5: Schematic of the SS compensated IPT system.

4.3 Dynamic Models of IPT System

4

This section presents the modeling procedure of a SS compensated IPT system using the developed EBM. To highlight the advantage of EBM in reducing the dynamic model order of the IPT system, the dynamic model using LPT is also derived for comparison purposes.

4.3.1 SS Compensated IPT Systems

The schematic of the studied IPT system is presented in Fig. 6.6. The main power stage consists of a DC voltage source, an H-bridge inverter, a primary and a secondary resonant circuit, an H-bridge diode rectifier and an equivalent modeled resistive load with a capacitive filter in parallel. The DC voltage u_{in} is converted into the AC voltage u_{AB} by the inverter. u_{AB} is a square waveform with the fundamental harmonic angular frequency as ω_{s}. The resonant circuits on both sides includes the inductances L_1 and L_2, the capacitances C_1 and C_2 and the equivalent parasitic series AC resistances R_1 and R_2. The mutual inductance between the Tx and Rx is M. The voltages across C_1 and C_2 are u_{C1} and u_{C2} respectively. The rectifier converts i_2 into the DC current i_{out} which feeds power to the filter capacitor C_{fo} and equivalent resistive load R_{L}. To reduce the voltage ripple across the load voltage u_{Cfo}, a large filter capacitor C_{fo} is connected in parallel with R_{L}.

The SS compensation is one of the basic compensation topologies that use a single capacitor in each coil side to form the resonant circuits in the IPT systems. The AC link of the SS compensated IPT system is of the fourth order, so its instantaneous state-space model will also be of the same order. To deal with the discontinuity of the instantaneous model, the state variables are replaced by their Fourier series coefficient. As the resonant circuits operate as a low-pass filter, fundamental harmonics approximation can deliver an accurate estimation of the system performances.

4.3.2 Dynamic Model Using LPT

The inverter and rectifier stages can be analysed by using the equivalent turns ratio [42]. Assuming that the dead time of the H-bridge inverter PWM signal is negligible, the equivalent turns ratio of the inverter s_1 and rectifier s_2 can be expressed as

$$s_1 = \text{sgn}[\cos(\omega t)], u_{\text{AB}} = s_1 u_{\text{in}} \tag{4.15a}$$

$$s_2 = \text{sgn}[i_2], u_{\text{ab}} = s_2 u_{\text{Cfo}}, i_{\text{out}} = s_2 i_2 \tag{4.15b}$$

By using the instantaneous variables, the 5th-order instantaneous state space model of the SS compensated IPT system is given by

$$\begin{cases} \begin{bmatrix} i_1' \\ u_{C1}' \\ i_2' \\ u_{C2}' \\ u_{Cfo}' \end{bmatrix} = \mathbf{A}_{p1} \begin{bmatrix} i_1 \\ u_{C1} \\ i_2 \\ u_{C2} \\ u_{Cfo} \end{bmatrix} + \mathbf{B}_{p1} s_1 u_{in} \\ \mathbf{A}_{p1} = \begin{bmatrix} -\frac{L_2 R_1}{F} & -\frac{L_2}{F} & \frac{M R_2}{F} & \frac{M}{F} & -\frac{M s_2}{F} \\ \frac{1}{C_1} & 0 & 0 & 0 & 0 \\ \frac{M R_1}{F} & \frac{M}{F} & -\frac{L_1 R_2}{F} & -\frac{L_1}{F} & \frac{L_1 s_2}{F} \\ 0 & 0 & \frac{1}{C_2} & 0 & 0 \\ 0 & 0 & -\frac{s_2}{C_{fo}} & 0 & -\frac{1}{R_L C_{fo}} \end{bmatrix} \\ \mathbf{B}_{p1} = \begin{bmatrix} \frac{L_2}{F} \\ 0 \\ -\frac{M}{F} \\ 0 \\ 0 \end{bmatrix} \\ F = L_1 L_2 - M^2 \end{cases} \tag{4.16}$$

In the phasor dynamic model, U_{in}, U_{Cfo} and I_{out} are the averaged values of the variables u_{in}, u_{Cfo} and i_{out}, $\mathbf{I}_1$, $\mathbf{I}_2$, $\mathbf{U}_{C1}$ and $\mathbf{U}_{C2}$ are dynamic phasors of the AC variables i_1, i_2, u_{C1} and u_{C2}, $\mathbf{S}_1$ and $\mathbf{S}_2$ are the complex turns ratio of the inverter and the rectifier, respectively. To regulate the power flow, the phase shift control is used to control the inverter output voltage by adjusting its conduction angle $\theta \in [0, \pi]$ [41]. Taking the phase angle of $\mathbf{U}_{AB}$ as reference, the complex turns ratio $\mathbf{S}_1$ and $\mathbf{S}_2$ can be expressed as

$$\mathbf{S}_1 = \frac{2\sqrt{2}}{\pi} e^{j0} \sin\frac{\theta}{2}, \mathbf{U}_{AB} = \mathbf{S}_1 U_{in} \tag{4.17a}$$

$$\mathbf{S}_2 = \frac{2\sqrt{2}}{\pi} e^{j[\arg(\mathbf{I}_2)]}, \mathbf{U}_{ab} = \mathbf{S}_2 U_{Cfo}, I_{out} = Re[\mathbf{S}_2^* \mathbf{I}_2] \tag{4.17b}$$

Since the phase angle of $\mathbf{S}_2$ is the same as that of $\mathbf{I}_2$, I_{out} can also be calculated as $I_{out} = |\mathbf{S}_2| e^{-j[\arg(\mathbf{I}_2)]} \mathbf{I}_2$.

The relation between the instantaneous variable x and its dynamic phasor $\mathbf{X}$ is given as

$$x = Re[\sqrt{2} \mathbf{X} e^{j\omega_s t}] \tag{4.18}$$

Based on (4.17a), (4.17b) and (4.18), (4.16) can be rewritten as

$$\begin{cases} \begin{bmatrix} (\mathbf{I}_1{}' + j\omega_s\mathbf{I}_1)e^{j\omega_s t} \\ (\mathbf{U}_{C1}{}' + j\omega_s\mathbf{U}_{C1})e^{j\omega_s t} \\ (\mathbf{I}_2{}' + j\omega_s\mathbf{I}_2)e^{j\omega_s t} \\ (\mathbf{U}_{C2}{}' + j\omega_s\mathbf{U}_{C2})e^{j\omega_s t} \\ U'_{Cfo}e^{j\omega_s t} \end{bmatrix} = \mathbf{A}_{p2} \begin{bmatrix} \mathbf{I}_1 e^{j\omega_s t} \\ \mathbf{U}_{C1}e^{j\omega_s t} \\ \mathbf{I}_2 e^{j\omega_s t} \\ \mathbf{U}_{C2}e^{j\omega_s t} \\ U_{Cfo}e^{j\omega_s t} \end{bmatrix} \\ \qquad\qquad + \mathbf{B}_{p1}\left[\mathbf{S}_1 e^{j\omega_s t} U_{in}\right] \\ \mathbf{A}_{p2} = \begin{bmatrix} -\frac{L_2R_1}{F} & -\frac{L_2}{F} & \frac{MR_2}{F} & \frac{M}{F} & -\frac{M\mathbf{S}_2}{F} \\ \frac{1}{C_1} & 0 & 0 & 0 & 0 \\ \frac{MR_1}{F} & \frac{M}{F} & -\frac{L_1R_2}{F} & -\frac{L_1}{F} & \frac{L_1\mathbf{S}_2}{F} \\ 0 & 0 & \frac{1}{C_2} & 0 & 0 \\ 0 & 0 & \frac{|\mathbf{S}_2|e^{-jarg[\mathbf{I}_2]}}{-C_{fo}} & 0 & -\frac{1}{R_L C_{fo}} \end{bmatrix} \end{cases} \tag{4.19}$$

$$\begin{cases} \begin{bmatrix} \mathbf{I}_1{}' \\ \mathbf{U}_{C1}{}' \\ \mathbf{I}_2{}' \\ \mathbf{U}_{C2}{}' \\ U'_{Cfo} \end{bmatrix} = \mathbf{A}_{p3} \begin{bmatrix} \mathbf{I}_1 \\ \mathbf{U}_{C1} \\ \mathbf{I}_2 \\ \mathbf{U}_{C2} \\ U_{Cfo} \end{bmatrix} + \mathbf{B}_{p1}\left[\mathbf{S}_1 U_{in}\right] \\ \mathbf{A}_{p3} = \mathbf{A}_{p2} - j\omega_s \begin{bmatrix} \mathbf{I}_{4\times4} & \\ & 0 \end{bmatrix} \end{cases} \tag{4.20}$$

By eliminating the term $e^{j\omega_s t}$ on both sides of (4.19), the 5th order complex phasor dynamic model of the SS compensated IPT system is obtained in (4.20).

To derive the solutions of the dynamic phasor variables, the 9th-order real-valued dynamic model can be expressed as

$$\begin{cases} \mathbf{x}_{LPT} = [\mathbf{I}_{1,re}, \mathbf{U}_{C1,re}, \mathbf{I}_{2,re}, \mathbf{U}_{C2,re}, \\ \qquad \mathbf{I}_{1,im}, \mathbf{U}_{C1,im}, \mathbf{I}_{2,im}, \mathbf{U}_{C2,im}, U_{Cfo}]^T \\ \mathbf{x}'_{LPT} = \mathbf{A}_{p4}\mathbf{x}_{LPT} + \mathbf{B}_{p2}\begin{bmatrix} \mathbf{S}_{1,re}U_{in} \\ \mathbf{S}_{1,im}U_{in} \end{bmatrix} \\ \mathbf{B}_{p2} = \begin{bmatrix} \frac{L_2}{F} & 0 & -\frac{M}{F} & 0 & 0 & 0 & 0 & 0 & 0 \\ 0 & 0 & 0 & 0 & \frac{L_2}{F} & 0 & -\frac{M}{F} & 0 & 0 \end{bmatrix}^T \end{cases} \tag{4.21}$$

where $\mathbf{A}_{p4}$ is written in (4.22). In the transient state, the phase of $\mathbf{I}_2$ changes. $\mathbf{S}_{2,re}$, which is in phase with $\mathbf{I}_2$, becomes a time-varying variable. Therefore, the phasor dynamic model in (4.21) is still time-varying.

$$\mathbf{A}_{\mathrm{p4}}=\begin{bmatrix} -\frac{L_2R_1}{F} & -\frac{L_2}{F} & \frac{MR_2}{F} & \frac{M}{F} & \omega_{\mathrm{s}} & & & & -\frac{MS_{2,\mathrm{re}}}{F} \\ \frac{1}{C_1} & & & & & \omega_{\mathrm{s}} & & & \\ \frac{MR_1}{F} & \frac{M}{F} & -\frac{L_1R_2}{F} & -\frac{L_1}{F} & & & \omega_{\mathrm{s}} & & \frac{L_1S_{2,\mathrm{re}}}{F} \\ & & \frac{1}{C_2} & & & & & \omega_{\mathrm{s}} & \\ -\omega_{\mathrm{s}} & & & & -\frac{L_2R_1}{F} & -\frac{L_2}{F} & \frac{MR_2}{F} & \frac{M}{F} & -\frac{MS_{2,\mathrm{im}}}{F} \\ & -\omega_{\mathrm{s}} & & & \frac{1}{C_1} & & & & \\ & & -\omega_{\mathrm{s}} & & \frac{MR_1}{F} & \frac{M}{F} & -\frac{L_1R_2}{F} & -\frac{L_1}{F} & \frac{L_1S_{2,\mathrm{im}}}{F} \\ & & & -\omega_{\mathrm{s}} & & & \frac{1}{C_2} & & \\ & & -\frac{S_{2,\mathrm{re}}}{C_{\mathrm{fo}}} & & & & -\frac{S_{2,\mathrm{im}}}{C_{\mathrm{fo}}} & & -\frac{1}{R_{\mathrm{L}}C_{\mathrm{fo}}} \end{bmatrix} \tag{4.22}$$

4

4.3.3 Dynamic Model Using EBM

In the EBM, the state variables are the fundamental harmonics amplitude of the oscillating instantaneous variables. I_1, I_2, U_{AB} and U_{ab} are the amplitude of i_1, i_2, u_{AB} and u_{ab} at the resonant angular frequency ω_{s}. The equivalent turns ratios of the inverter S_1 and rectifier S_2 can be expressed as

$$S_1=\frac{4}{\pi}sin\frac{\theta}{2},U_{\mathrm{AB}}=S_1U_{\mathrm{in}} \tag{4.23a}$$

$$S_2=\frac{4}{\pi},U_{\mathrm{ab}}=S_2U_{\mathrm{Cfo}},I_{\mathrm{out}}=\frac{1}{2}S_2I_2 \tag{4.23b}$$

The resonant frequency of the resonant circuit ω_{r} is assumed equal to ω_{s}. The output filter capacitor C_{fo} can be modeled by

$$U'_{\mathrm{Cfo}}=\frac{S_2I_2}{2C_{\mathrm{fo}}}-\frac{U_{\mathrm{Cfo}}}{C_{\mathrm{fo}}R_{\mathrm{L}}}. \tag{4.24}$$

The energy balance of the secondary resonant circuits can be expressed as

$$L_2I'_2=\frac{\omega_{\mathrm{s}}MI_1}{2}-\frac{R_2I_2}{2}-\frac{S_2U_{\mathrm{Cfo}}}{2}. \tag{4.25}$$

Based on (4.14), (4.24) and (4.25), the EBM dynamic model of the SS compensated IPT system is obtained as

$$\begin{cases} \mathbf{x}_{\mathrm{EBM}}=[I_1,I_2,U_{\mathrm{Cfo}}]^T \\ \mathbf{x}_{\mathrm{EBM}}{}'=\mathbf{A}_{\mathrm{e1}}\mathbf{x}_{\mathrm{EBM}}+\mathbf{B}_{\mathrm{e1}}S_1U_{\mathrm{in}} \\ \mathbf{A}_{\mathrm{e1}}=\begin{bmatrix} -\frac{R_1}{2L_1} & -\frac{\omega_{\mathrm{s}}M}{2L_1} & 0 \\ \frac{\omega_{\mathrm{s}}M}{2L_2} & -\frac{R_2}{2L_2} & -\frac{S_2}{2L_2} \\ 0 & \frac{S_2}{2C_{\mathrm{fo}}} & -\frac{1}{C_{\mathrm{fo}}R_{\mathrm{L}}} \end{bmatrix} \\ \mathbf{B}_{\mathrm{e1}}=\begin{bmatrix} \frac{1}{2L_1} \\ 0 \\ 0 \end{bmatrix} \end{cases} \tag{4.26}$$

4.3.4 Frequency Sensitivity of EBM when $\omega_s \neq \omega_r$

The developed EBM method is based on the assumption that ω_r is equal to ω_s. However, in real practice, ω_s might be tuned to make the input impedance of the resonant circuit slightly inductive, such that the zero voltage switching (ZVS) operation can be achieved in the inverter [82]. In the SS compensated IPT system, ω_s should be slightly larger than ω_r when the system works in non-bifurcation region [99]. Therefore, the sensitivity of the proposed EBM is discussed when $\omega_s \neq \omega_r$.

For the phase angle α_1 that represents the lagging of the waveform of i_1 in relation to u_{AB}, the average power injected into the primary resonant circuit becomes $\frac{1}{2} I_1 U_{AB} \cos(\alpha_1)$. Similarly, the power transferred to the secondary side is $\frac{1}{2}\omega M I_1 I_2 \cos(\alpha_2)$, where α_2 is the phase angle between i_2 and the secondary induced voltage. The revised dynamic model using EBM can be obtained as

$$\begin{cases} \mathbf{x}_{EBM}{}' = \mathbf{A}_{e2}\mathbf{x}_{EBM} + \mathbf{B}_{e2}U_{in} \\ \mathbf{A}_{e2} = \begin{bmatrix} -\frac{R_1}{2L_1} & -\frac{\omega_s M cos(\alpha_2)}{2L_1} & 0 \\ \frac{\omega_s M cos(\alpha_2)}{2L_2} & -\frac{R_2}{2L_2} & -\frac{S_2}{2L_2} \\ 0 & \frac{S_2}{2C_{fo}} & -\frac{1}{C_{fo}R_L} \end{bmatrix} \\ \mathbf{B}_{e2} = \begin{bmatrix} \frac{S_1 cos(\alpha_1)}{2L_1} \\ 0 \\ 0 \end{bmatrix} \end{cases} \tag{4.27}$$

The predicted results from EBM and LPT are compared with circuit simulations as shown in Fig. 4.6.

In Fig. 4.6(c) and 4.6(f), the transient behaviours of α_1 and α_2 are presented. Both α_1 and α_2 exhibit rapid transient responses which last less than 0.25 ms when ω_s is below 86 kHz. Besides, their absolute values are mostly below 20 degree. This means the primary and secondary resonant circuits are operating close to the resonance and (6.9) is still acceptably accurate. Consequently, it is reasonable for EBM to simplify the dynamic model by assuming that α_1 and α_2 keep at their steady states throughout the transients when ω_s is below 86 kHz. In Fig. 4.6(a) and 4.6(b) where $\omega_s = \omega_r$, the predicted results from the EBM and LPT match the simulated waveforms well. The transient and steady states are both accurately evaluated. When ω_s = 86kHz, the steady state value of α_1 is around 20 degree which can ensure ZVS operation of the inverter. As shown in Fig. 4.6(d) and 4.6(e), the predicted curves from the EBM and LPT both slightly deviate from the envelope of the simulated waveforms, while the estimation of the transient time and steady state values is still accurate.

However, as ω_s becomes larger than 87 kHz as shown in Fig. 4.6(i), the transient time of α_1 and α_2 increases. Although the absolute value of α_2 maintains less than 9 degree over a large region, the steady state absolute value of α_1 is around 37 degree. This proves the primary resonant circuits drift away from the resonance operation, and thus (6.9) and the EBM become inaccurate. As presented in Fig. 4.6(g) and 4.6(h), the curves from the LPT match the simulated waveforms at the beginning of the transients, while fluctuating around the envelope of the waveforms with a small error. By contrast, the EBM constantly underestimates the amplitude of the waveforms during transient.

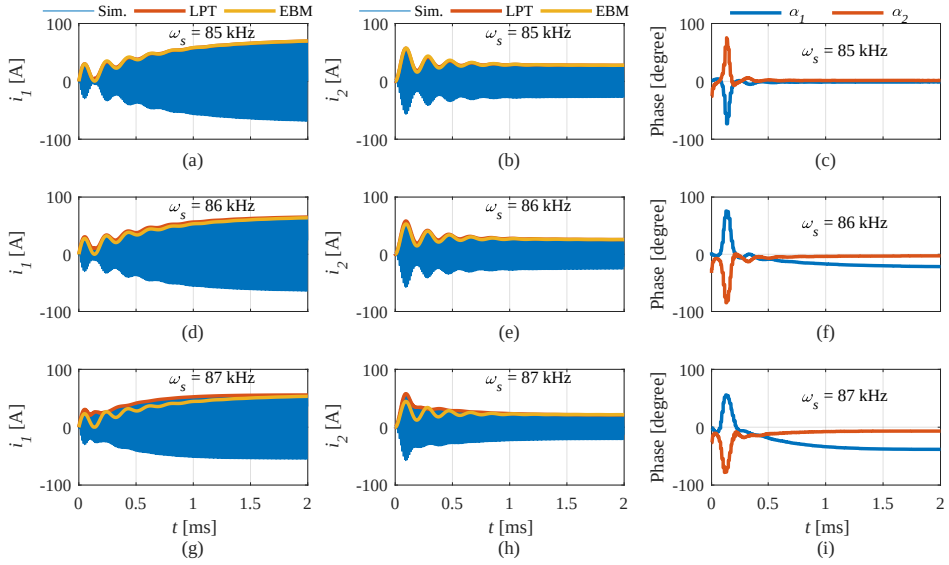

Figure 4.6: Comparison between dynamic models using EBM and circuit simulations, where $u_{\text{in}} = 100\text{V}$, $\omega_{\text{r}} = 85\text{kHz}$, $C_{\text{fo}} = 80\mu\text{F}$ and the rest of the circuit parameters are the same as Fig.6.4.

.

The power flow of IPT systems is commonly regulated via a natural resonant frequency tracking method that will tune the inverter operating frequency to an equivalent fixed-frequency control strategy, particularly because of the nonlinear relation of the output power to ω_{s}. Besides, by applying an equivalent fixed-frequency control strategy [96, 100, 101], the resonant circuit can operate at its natural optimum efficiency with minimum switching losses in the full-bridge inverter [12]. Indeed, it is normal for high-efficiency IPT systems employing optimal load matching that ω_{s} is tuned for the ZVS turn-on operation of the H-bridge inverter and is close to the resonant frequency of the IPT systems. Therefore, the EBM is suitable to model IPT systems oriented for EV charging applications.

4.4 Model Predictive Control

MPC formulates an optimization problem based on a cost function. To evaluate the cost function at a certain control input, the dynamic model of the target system and the measurements of the state variables are required. By traversing the search space of the control signal, MPC can find the optimal control input minimizing the cost function at each control period. As the order of the system increases, difficulties arise in computing the optimization loop and sampling the state variables. In IPT EV charging applications, the switching frequency ranges from 79-90 kHz, and the order of the AC link is above four, which poses challenges to finishing the optimization loop within one switching cycle. Simplifying the dynamic model becomes vital to facilitate the application of the MPC. To highlight the advantage of reducing the order of the dynamic model, MPC controllers are designed based on (4.21) and (4.27), respectively.

In both EBM and LPT methods, the state variables are derived from the first-order Fourier coefficient. As a discrete control strategy, the state variables have to be sampled at each control period. Considering the principle of phase shift control, the control period should be an integral multiple of the switching cycle T_s. In this section, the control period is set equal to T_s such that the control input can be updated at the start of each switching cycle. Based on the forward Euler method, the discrete predictive model can be obtained as

$$\mathbf{x}_{\mathrm{EBM}}(k+1) = (T_s\mathbf{A}_{e1} + \mathbf{I}_{3\times3})\mathbf{x}_{\mathrm{EBM}}(k) + T_s\mathbf{B}_{e1}S_1U_{\mathrm{in}} \tag{4.28a}$$

$$\mathbf{x}_{\mathrm{LPT}}(k+1) = (T_s\mathbf{A}_{p4}(k) + \mathbf{I}_{9\times9})\mathbf{x}_{\mathrm{LPT}}(k) + T_s\mathbf{B}_{p2}\begin{bmatrix}\mathbf{S}_{1,\mathrm{re}}U_{\mathrm{in}}\\ \mathbf{S}_{1,\mathrm{im}}U_{\mathrm{in}}\end{bmatrix} \tag{4.28b}$$

It should be noticed that the matrix $\mathbf{A}_{p4}$ is dependent on $\mathbf{x}_{\mathrm{EBM}}(k)$ according to (4.17b).

As shown in (4.28), the MPC based on the LPT method requires measurements of nine state variables. Regarding the measurements of the amplitude and phase of the oscillating variables, the sampling sequence is illustrated in Fig.6.8, where u_{AB} is taken as the phase reference.

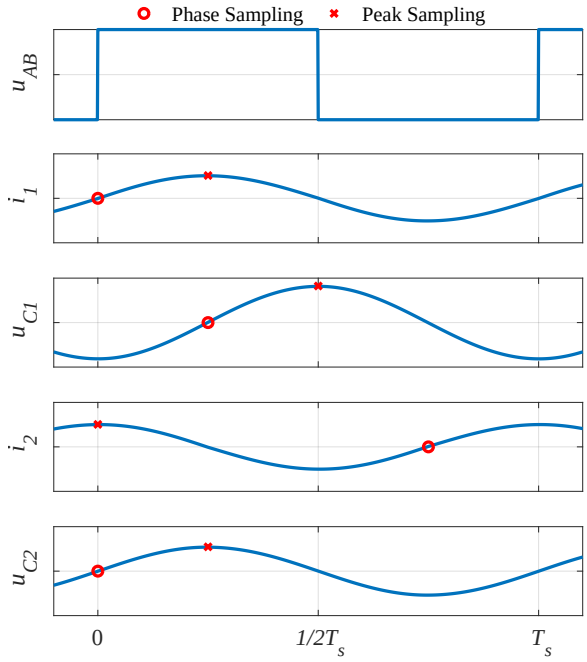

Figure 4.7: Sampling sequence of the oscillating variables.

To control the power flow of the IPT system, u_{Cfo} is taken as the control target. However, the predictive models in (4.28) cannot convey an explicit function between the control input and the target. Thus, multiple iterations are required to obtain the response of u_{Cfo} under a certain θ. According to the matrix $\mathbf{B}_{e1}$ and $\mathbf{B}_{p2}$, the predictive models based on the EBM and LPT require three steps in each optimization loop. For example, at the k_{th}

switching cycle, $U_{\mathrm{Cfo}}(k+3)$ is calculated to compute the cost function for the MPC based on the EBM. In order to constrain the overshoot of i_1 and i_2, and to minimize the output ripple in the steady state, the cost functions are defined as

$$G_{\mathrm{EBM}} = w_1 \left|U^*_{\mathrm{Cfo}} - U_{\mathrm{Cfo}}(k+3)\right| + w_2 \left|I^*_2 - I_2(k+2)\right| + w_3 \left|I^*_1 - I_1(k+1)\right| \tag{4.29a}$$

$$G_{\mathrm{LPT}} = w_4 \left|U^*_{\mathrm{Cfo}} - \sqrt{2}U_{\mathrm{Cfo}}(k+3)\right| + w_5 \left|I^*_2 - \sqrt{2}|\mathbf{I}_2(k+2)|\right| + w_6 \left|I^*_1 - \sqrt{2}|\mathbf{I}_1(k+1)|\right| \tag{4.29b}$$

where w_1, w_2, w_3, w_4, w_5 and w_6 are the weight factors.

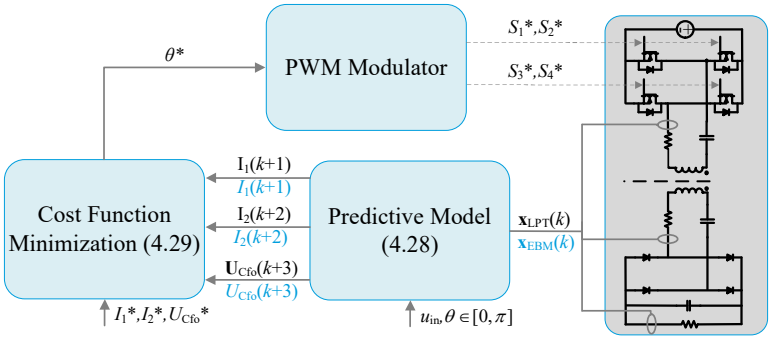

Figure 4.8: Diagram of the proposed MPC controller.

The structure of the MPC controllers is depicted in Fig. 6.9. Based on the measurements of the state variables, the predictions can be obtained by using (4.28). The predictions are evaluated by applying the cost functions in (4.29). The cost function minimization block can find the optimal control input θ^* under the current switching cycle. Although both the MPC controllers based on EBM and LPT methods execute three iterations for each given θ, the number of equations to be solved is three times larger in the controller based on the LPT strategy due to its high order of the dynamic model. To finish the MPC optimization within one switching cycle, it is essential to reduce the computation labor, which makes the EBM more advantageous.

To compare the computation time of the developed MPC controllers, the optimization cycle is conducted in Matlab on a computer with an Intel(R) Xeon(R) W-2123 CPU. In each optimization cycle, 50 different values of θ in the range of $[0, \pi]$ are assigned to the predictive model whose results are compared according to the defined cost function. By conducting the optimization cycle 100 000 times, the average computation time of one optimization cycle is 0.0037 ms for the EBM and 1.6 ms for the LPT. This can prove that the MPC controller based on EBM is more practical to control IPT systems.

Fig. 6.10 presents the closed-loop transient response of the proposed MPC controllers. To investigate the impacts of the feedback measurement error, band-limited white noise (peak value less than 10 % of the signal's steady state value, sampling frequency at 86.3 kHz) is added to the feedback signals. When the noise is absent, the MPC controllers using both the EBM and LPT methods can effectively regulate u_{Cfo}, while the MPC controller based on the EBM strategy shows superiority in terms of the transient time, overshoot and steady state ripple. The waveform of the MPC controller based on the LPT method

presents a relatively large ripple, which mainly results from the error of measurements. As per Fig. 6.8, the sampling time of the phase and peak is not synchronized, and thus there will be an error between the sampled values of the state variables and their real values when the optimization starts running. Since there are eight state variables sampled from the oscillating waveform, the sampling error could accumulate on the predicted results. By contrast, the MPC controller based on the EBM requires two state variables from the waveform which makes it more reliable. Moreover, peak sampling is easier to realize in software or hardware than phase sampling in practice. When the noise is added to the feedback signals, the MPC controller based on EBM delivers almost the same transient response, while the transient behaviors of the controller based on the LPT method have a longer transient time and a larger ripple.

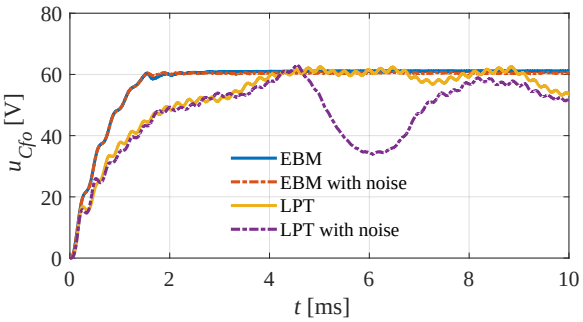

Figure 4.9: Close-loop transient response of the MPC controllers and impacts of the feedback noise, where $u_{\text{in}} = 100\text{V}$, $U^*_{\text{Cfo}} = 60\text{V}$, the circuit parameters are listed in Table I.

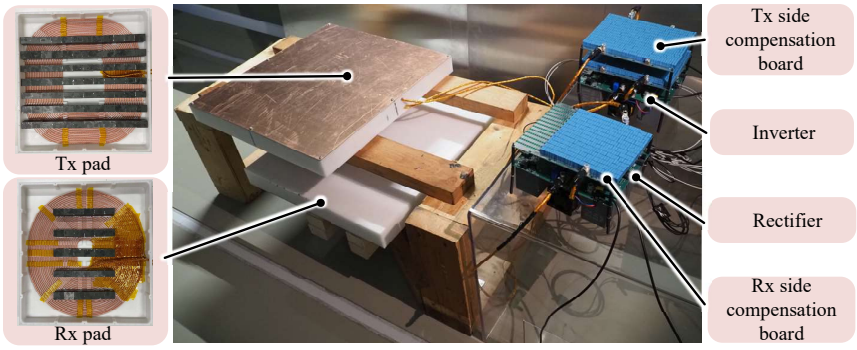

Figure 4.10: Picture of the IPT system.

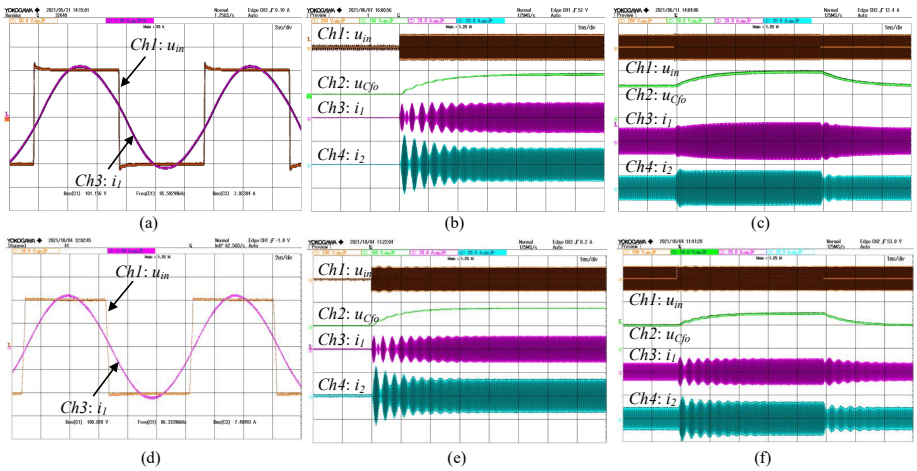

Figure 4.11: Experimental waveforms for case A ((a)-(c)) and case B ((d)-(f)), (a) and (d): ZVS turn-on operation of the H-bridge inverter; (b) and (e): start-up response of the IPT system; (c) and (f): step response starting from nonzero conditions.

4.5 Experimental verification

To verify the developed EBM and MPC controller, experiments are conducted in the IPT system shown in Fig. 6.11. Two cases (case A and case B) of experiments are conducted to show the accuracy of the proposed EBM under different switching frequencies. The experimental system parameters for these two cases are listed in Table I where ω_s and the resonant frequency for the Tx $\omega_{r,1}$ and Rx $\omega_{r,2}$ sides are included. In both cases, the ZVS turn-on operation of the H-bridge inverter is achieved. Compared with case A, case B operates closer to the natural resonance of the IPT system, and the EBM thus delivers a higher prediction accuracy for case B. u_{in} is set to be constant and equal to 100 V in all the experiments.

4.5.1 Start-up Response

The start-up waveforms that are illustrated in Fig. 6.12(b) and 6.12(e) are measured when θ steps from zero to π. Fig. 6.12(a) and 6.12(d) show that i_1 slightly lags u_{in} and the ZVS operation of the inverter is guaranteed. By applying the same conditions, u_{Cfo}, i_1 and i_2 predicted by the LPT in (4.21) and by the EBM in (4.27) are compared with the experimental results, as depicted in Fig. 6.13. Since $|\mathbf{I}_1|$ and $|\mathbf{I}_2|$ represent the RMS value of i_1 and i_2 at the fundamental frequency in the LPT method, the curves from the LPT dynamic model indicates the value of $\sqrt{2}|\mathbf{I}_1|$ and $\sqrt{2}|\mathbf{I}_2|$.

In Fig. 6.13, a better agreement between the analytical and experimental results can be observed in case B, because the operation frequency of case B is closer to the resonance than case A. In Fig. 6.13(a) and 6.13(d), the analytical models accurately predict the transients of u_{Cfo}. In Fig. 6.13(e) and 6.13(f), the ripples of the waveform envelop are accurately predicted by the EBM. Although the predicted curves show a small error in the later stage of the transients in Fig. 6.13(b) and 6.13(c), the EBM can accurately predict the early stage

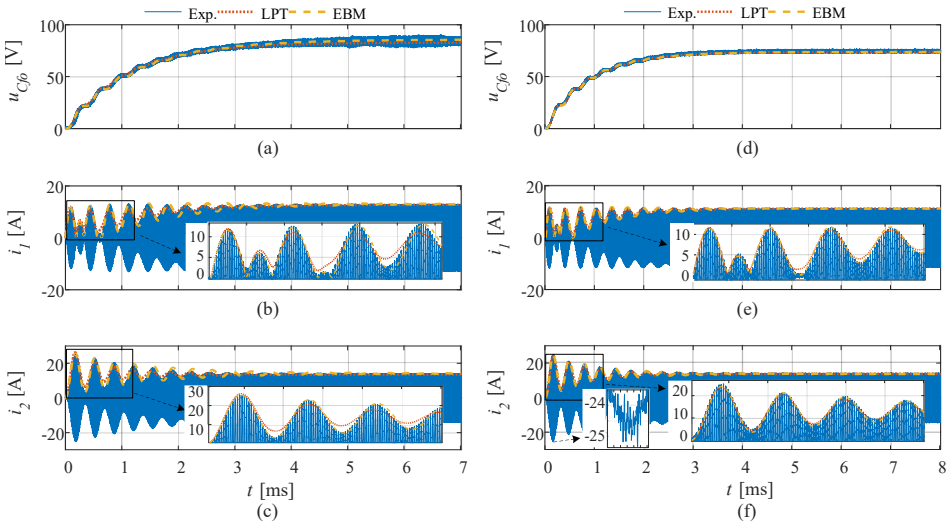

Figure 4.12: Comparison of the start-up responses between the experimental results and the solutions derived from the analytical dynamic models for case A ((a)-(c)) and case B ((d)-(f)).

Table 4.1: Circuit parameters of the SS compensated IPT system

Variables	Unit	Case A Value	Case B Value
L_1	μH	301.65	292.77
L_2	μH	202.17	199.18
M	μH	15.69	17.21
C_1	nF	11.70	11.69
C_2	nF	17.12	17.11
C_{fo}	μF	100	100
R_1	Ω	0.1	0.1
R_2	Ω	0.5	0.7
R_{L}	Ω	10	8.6
$\omega_{\mathrm{r},1}$	kHz	84.7	86.0
$\omega_{\mathrm{r},2}$	kHz	85.5	86.2
ω_{s}	kHz	85.6	86.3

of the step response as shown in the zoomed-in views, which ensures that the overshoot can be accurately estimated.

Both EBM and LPT models can mostly match the peaks of i_1 and i_2, and the EBM becomes more accurate when the IPT system operates closer to its resonance point. It proves that the EBM can accurately predict the transients of the SS compensated IPT system starting from zero conditions.

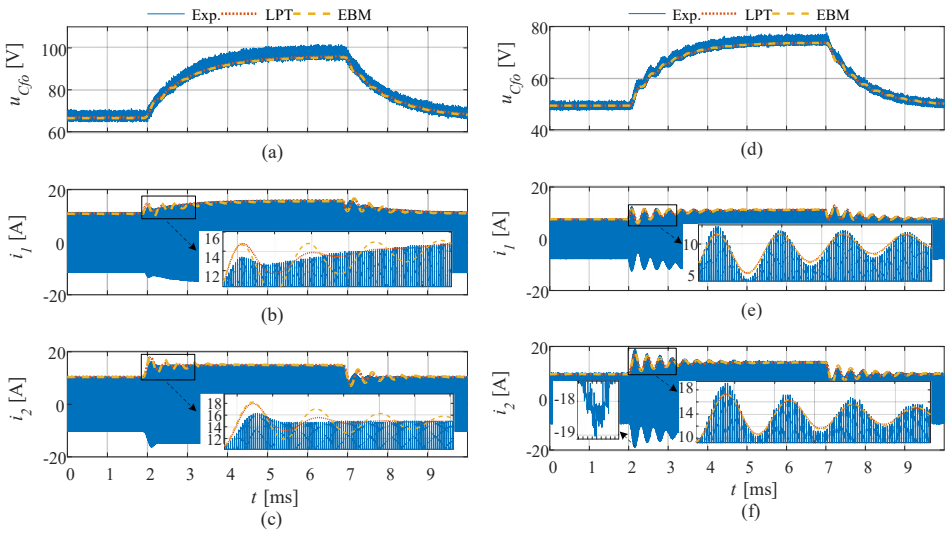

Figure 4.13: Comparison of the step responses starting from nonzero conditions between the experimental results and the solutions derived from the analytical dynamic models for case A ((a)-(c)) and case B ((d)-(f)).

4.5.2 Step Response Starting under Nonzero Conditions

To test the accuracy of the proposed EBM model, step responses under nonzero conditions are measured on the IPT system. When the system reaches steady state with θ equal to $\frac{\pi}{2}$, a step of $\frac{\pi}{2}$ is added to θ. After 5 ms, a step of $-\frac{\pi}{2}$ is added to θ. The measured waveforms are presented in Fig. 6.12(c) and 6.12(f). By applying the same operating conditions, the predicted curves from the EBM and LPT methods are compared with the measured waveforms in Fig. 6.14.

Similar to the step response, the prediction accuracy of case B is generally higher than case A because the operating frequency of case B is close to the resonant frequency of the IPT system. In Fig. 6.14(a) and 6.14(d), the analytical results of u_{Cfo} match the measurements well, which implies that the proposed EBM can be used to design a controller for the output power regulation. In the prediction of i_1 and i_2 in case A, the EBM and LPT methods both overestimate the overshoot, and the curves from the EBM take a longer time to reach the steady state, as shown in Fig. 6.14(b) and 6.14(c). By contrast, the prediction accuracy in case B is obviously higher, and the curves of the EBM and the LPT method overlap mostly. Therefore, the EBM strategy is proved to be able to accurately predict the system transient responses starting from nonzero conditions.

4.5.3 Transient Response with MPC

To prove the advantage of the presented EBM in reducing the order of the dynamic model, the MPC controllers are developed in Section IV. Since the main idea of this chapter is the proposed dynamic modeling method, the MPC controllers are not physically implemented on the IPT system. Instead of building the real feedback controller, a lookup table of the control input, generated from circuit simulations, is applied to control the IPT system. The

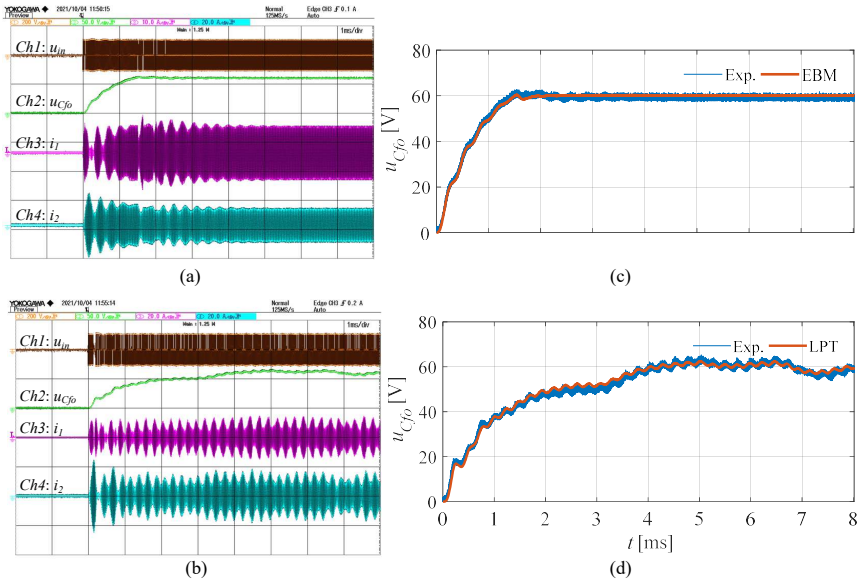

Figure 4.14: Measured transient response using MPC methods based on (a) EBM and (b) LPT strategies. The comparison between the measurements and simulations is presented in (c) and (d).

circuit simulation model utilizes the same parameters of case B as listed in Table I. The reference voltage is set to be 60 V. The control input is obtained from simulations using MPC based on the EBM and LPT methods.

The experimental waveforms are illustrated in Fig. 6.15(a) and 6.15(b). The MPC based on the EBM can effectively regulate u_{Cfo}, while the MPC based on the LPT method shows obvious ripples in u_{Cfo} and the envelopes of the winding currents also oscillate. The experimental results are also compared with the simulations in Fig. 6.15(c) and 6.15(d). The simulated curves match the measurements well, which proves the simulation models can accurately reflect the transients of the IPT system. In Fig. 6.15(c), the MPC based on the EBM delivers good dynamic performances. u_{Cfo} reaches steady state in 1.5 ms with almost no overshoot. By contrast, the transient time is longer and u_{Cfo} fluctuates in the steady state in Fig. 6.15(d). This is because the MPC based on LPT requires feedback signals of nine state variables. The sampling timing cannot be synchronized as illustrated in Fig. 6.8, leading to errors in the feedback signals. As a result, the predicted results are inaccurate in each optimization cycle of the MPC controllers based on the LPT method. The developed MPC based on the EBM is proven to be effective in regulating the output voltage of the IPT system. Meanwhile, it is also evidence that the proposed EBM can accurately model the dynamics of the IPT system.

4.6 Conclusions

This chapter develops a dynamic modeling method for IPT systems based on the energy interactions between the resonant tanks. To verify the accuracy of the proposed EBM, the

dynamic models of a SS compensated IPT system are built based on the EBM and LPT methods. By using the EBM, the dynamic model of the AC-link is of second order which is one-fourth that of the LPT strategy. To prove the accuracy of the EBM when the switching frequency deviates from the resonant frequency, the transient behavior of the IPT system is studied in the switching frequency range of 85 −87 kHz. To further show the advantage of the EBM, the EBM and LPT methods are applied to design MPC controllers. The MPC controller based on the EBM requires just three feedback signals and less computation time, and delivers a better transient response than the LPT strategy. Finally, experiments are conducted to validate the accuracy of the EBM and the effectiveness of the developed MPC controller based on the EBM.

In this chapter, a lookup table of the control input is used to regulate the IPT system. It is valuable to further investigate the impact of the sampling delay and computation time on the transient performance of the developed MPC controller. We will physically build a MPC controller to control the IPT system in our future work.

5

Power Fluctuation Reduction

One of the challenges of dynamic wireless power transfer (DIPT) systems for electric vehicle (EV) charging applications is to reduce pick-up power fluctuation. Building a multiphase transmitter (Tx) is proven to be effective in stabilizing the pick-up power in literature, while the major drawback is a significant increment in the material cost on the Tx side. This paper proposed a new magnetic coupler mechanism that can achieve a low-ripple pick-up power without increasing the material cost on the Tx side. The operating principle of the proposed DIPT system is explained in detail. Besides, an optimization method is introduced to find the optimal deployment of Tx and receiver (Rx) coils, and the optimal ripple of the Rx induced voltage is below 17.1%. *Finally, a prototype is built according to the optimization results and the measured curve of the direct current (DC) voltage across the load resistor has the same pattern as the calculated results with a* 7.8% *higher ripple due to the fabricating error of the coils.*

This chapter is based on:

- W. Shi, J. Dong, G. Yu, G. Zhu, P. Bauer, *"Low Output Power Ripple Dynamic Wireless Power Transfer based on Dual-Phase Non-Overlapped Transmitters", preprint.*

5.1 Introduction

Inductive power transfer (IPT) technology is applied to the EV battery charging applications as an alternative to the conductive charging method [20, 28, 77, 82, 93, 102, 103]. IPT technology can automize the charging procedure and thus save the labor of the EV users. It is also promising to build dynamic IPT charging roads where EVs can pick up power while traveling [20, 37, 96, 102, 104], thereby contributing to the reduction in the requirement of the traction batteries' capacity as well as the extension of the driving range.

One of the challenges of DIPT systems is to keep a stable pick-up power which is mainly determined by the structure and deployment of the magnetic coupler. The widely studied magnetic couplers for DIPT systems are illustrated in Tab. 5.1. For segmented DIPT systems, the magnetic coupling curve is seamed unless Tx coils are deployed tightly [105, 106]. As a result, the building cost of the segmented DIPT system increases dramatically. When DD-DD (length direction) or DD-Rect (length direction) is used for a segmented DIPT system, null power points cannot be avoided. To solve this problem, a multiphase Rx pad consisting of rectangular and DD coils has been proposed [28]. Since the induced voltages of the DD coil and rectangular coil may cancel each other at a certain area, these two coils on a multiphase Rx side are connected to two different rectifiers, which also increases the component cost of the segmented DIPT system. Provided the magnetic coupling curve is seamless, the induced voltage on the Rx side still fluctuates seriously as indicated in Tab. 5.1. Therefore, a back-end DC/DC converter has to be adopted to ensure a stable output power into batteries [96].

For elongated DIPT systems applying BC-DD (width direction) and UC-Rect magnetic couplers as presented in Tab. 5.1, a stable pick-up power over a large area can be achieved simply by extending the length of elongated coils. Apart from the high magnetic field radiation, extending the length of elongated coils also leads to higher Tx side power losses and voltage stresses over resonant components. Besides, multiple Rx coils may be coupled with one long elongated coil, and thick Litz wires have to be used for windings to allow for a large power capacity [71]. To eliminate the impact of the decreased magnetic coupling near the Tx coils' edge, adjacent Tx coils are overlapped [107, 108], or flat compensation inductors are deployed on the Tx coils' edge to compensate for the main magnetic coupling drop[109].

Elongated DIPT systems using BC-DD (length direction) and BC-Rect magnetic couplers have a sinusoidal magnetic coupling curve as depicted in Tab. 5.1. The period of the sinusoidal curve is equal to twice the pole length of the elongated DD coil. To avoid null power points, there are studies proposing multiphase Rx side [72, 73]. However, the pick-up power still fluctuates considerably and extra rectifiers are required in DIPT systems using the multiphase Rx side. To realize a stable pick-up power, the multiphase Tx track is proven to be a reliable solution for elongated DIPT systems with a sinusoidal magnetic coupling curve [74–76]. In the multiphase Tx track, multiple identical elongated BC coils are overlapped with a spatial offset in the driving direction. These elongated BC coils are powered by alternating current (AC) power sources with a certain phase shift. By employing the multiphase Tx track, the pick-up power of the elongated DIPT system becomes independent of the Rx coil's position in the driving direction owing to the sinusoidal magnetic coupling curve, so a stable output power is obtained.

Based on the above literature study, it can be summarized that the multiphase Tx

Table 5.1: Widely studied coil topology for DIPT applications

Segmented Track			
DD-DD (length)	DD-DD (width)	DD-Rect. (length)	Rect.-Rect.
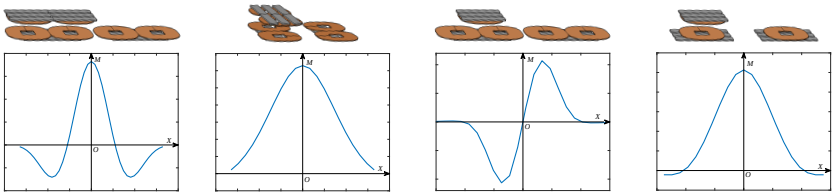			
Elongated Track			
BC-DD (length)	BC-DD (width)	BC-Rect. (length)	UC-Rect.
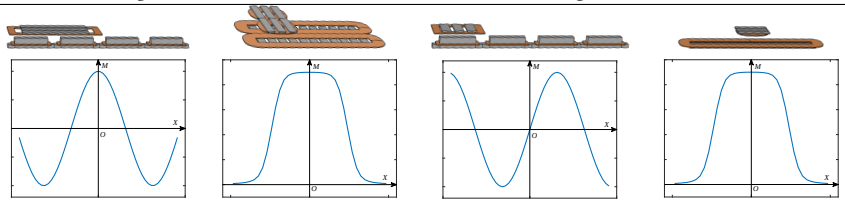			

method outperforms other methods in terms of the stability of the output power without the control of a back-end DC/DC converter. However, the material cost of the multiphase Tx track is too high since the total copper used for the Tx track is equal to the product of that of a single-phase coil multiplied by the number of the system phases. To address this issue, this study presents the design of a segmented DIPT system where a multiphase Tx track is built by using non-overlapped and loosely-deployed segmented Tx coils for the first time. The proposed segmented DIPT system can deliver a low-ripple pick-up power without increasing the copper cost on the Tx side.

This chapter will first introduce the operating principle of achieving stable pick-up power for both elongated and segmented DIPT systems. Then, the optimization design of the proposed segmented DIPT system is presented. Finally, based on the optimization results, a DIPT prototype is built and tested on a moveable platform and the measurements verify the performances of the proposed DIPT system.

5.2 DIPT Systems with A Multiphase Tx Side

The goal of building the multiphase Tx side is to maintain a stable pick-up power while the Rx side moves along the driving direction [74, 76]. However, a vital condition to achieve this goal is that the magnetic coupling curve of the DIPT system is sinusoidal, and only elongated DIPT systems applying BC-DD (length direction) and BC-Rect (length direction) can meet this condition according to Tab. 5.1. This section will introduce the operation principles of DIPT systems with a multiphase Tx side.

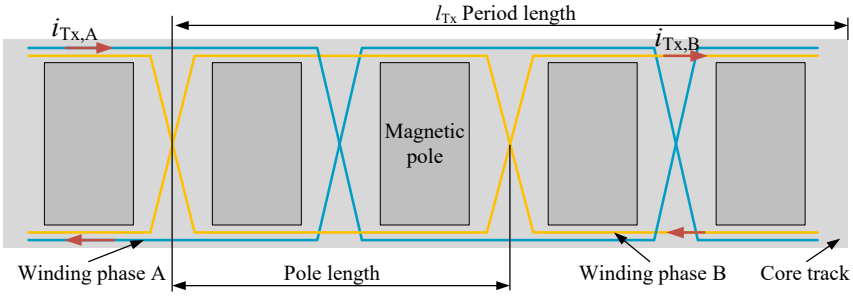

Figure 5.1: A dual-phase Tx track of an elongated DIPT system.

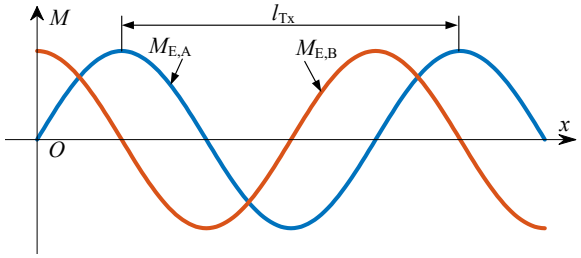

Figure 5.2: Magnetic coupling curves of an elongated DIPT system.

5.2.1 Conventional Dual-phase Elongated DIPT Systems

An elongated DIPT system employing the dual-phase Tx coils is illustrated in Fig. 5.1. There are two magnetic poles within a pole length. The Rx side can use either a DD or a rectangular coil. When the Rx side moves in the driving direction, the magnetic coupling changes in a sinusoidal form. The Tx side has two identical windings which are powered by two separate AC sources phase A and phase B. There is a $\frac{\pi}{2}$ phase difference between these two phases. The windings are overlapped and deployed with a spatial offset. The spatial offset is designed to be a quarter of the period length. This spatial offset determines the phase difference of the magnetic coupling curves, $M_{E,A}$ for the phase A winding and $M_{E,B}$ for the phase B winding. The magnetic coupling curves $M_{E,A}$ and $M_{E,B}$ are depicted in Fig. 5.2, and can be expressed as

$$M_{E,A} = M_0 sin(\frac{2\pi x}{l_{Tx}}), M_{E,B} = M_0 sin(\frac{2\pi x}{l_{Tx}} + \frac{\pi}{2}), \tag{5.1}$$

where M_0 is the peak magnetic coupling. The x axis in Fig. 5.2 is defined to be the driving direction. The phasors of currents through the winding phase A and the winding phase B are $\mathbf{I}_{Tx,A}$ and $\mathbf{I}_{Tx,B}$, respectively. $\mathbf{I}_{Tx,A}$ and $\mathbf{I}_{Tx,B}$ are expressed as

$$\mathbf{I}_{Tx,A} = I_{Tx} e^{j0}, \mathbf{I}_{Tx,B} = I_{Tx} e^{j\frac{\pi}{2}}, \tag{5.2}$$

where I_{Tx} is the amplitude of the Tx winding current. Based on (5.1) and (5.2), the phasor of the induced voltage in the Rx coil of the elongated DIPT system $\mathbf{U}_{\mathrm{RxE}}$ can be calculated as

$$\begin{aligned}\mathbf{U}_{\mathrm{RxE}} &= j\omega M_0 I_{\mathrm{Tx}} sin(\frac{2\pi x}{l_{\mathrm{Tx}}})e^{j0} + j\omega M_0 I_{\mathrm{Tx}} sin(\frac{2\pi x}{l_{\mathrm{Tx}}} + \frac{\pi}{2})e^{j\frac{\pi}{2}} \\ &= j\omega M_0 I_{\mathrm{Tx}}(sin(\frac{2\pi x}{l_{\mathrm{Tx}}}) + jcos(\frac{2\pi x}{l_{\mathrm{Tx}}})) \\ &= -\omega M_0 I_{\mathrm{Tx}} e^{-j\frac{2\pi x}{l_{\mathrm{Tx}}}},\end{aligned} \tag{5.3}$$

where ω is the angular operation frequency, l_{Tx} is the period length. As per (5.3), $\mathbf{U}_{\mathrm{RxE}}$ has a magnitude of $\omega M_0 I_{\mathrm{Tx}}$ that is independent of the position of the Rx coil along the x axis. Therefore, the elongated DIPT system shown in Fig. 5.1 can deliver a stable pick-up power when the Rx side moves in the driving direction. However, the main drawback is the high cost of the Litz wire, which makes it very expensive to build a conventional multiphase DIPT system.

5.2.2 Proposed Dual-phase Segmented DIPT Systems

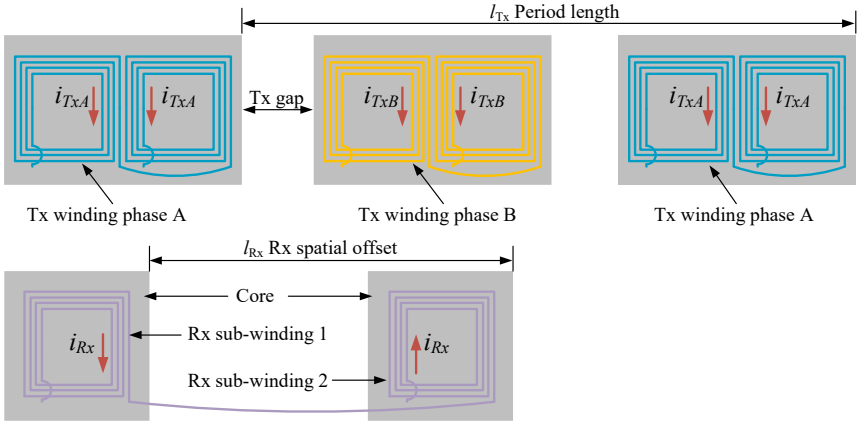

Figure 5.3: A dual-phase Tx track of a segmented DIPT system.

To reduce the cost of the conventional multiphase DIPT system, this study proposes a dual-phase DIPT system employing segmented Tx coils. Moreover, the Tx coils are deployed loosely and the gap between adjacent Tx coils is one of the key design variables to reduce the fluctuation of the pick-up power. As presented in Fig. 5.3, the proposed segmented DIPT system applies DD coils as the Tx side, such that the magnetic coupling curve between the Tx and Rx side has a sinusoidal-like shape when the Rx coil is above a DD coil. The Tx coils are powered by two separate AC sources whose phase difference is $\frac{\pi}{2}$. The Rx side consists of two rectangular sub-windings connected in an aiding series. These two Rx sub-windings are spatially separated by the Rx gap which can eliminate the magnetic coupling between these Rx sub-windings. The circuit configuration of the proposed DIPT system is shown in Fig. 5.4.

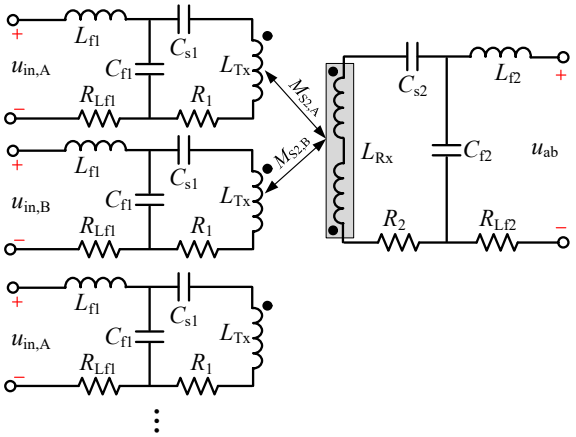

Figure 5.4: Circuit configuration of the proposed DIPT system.

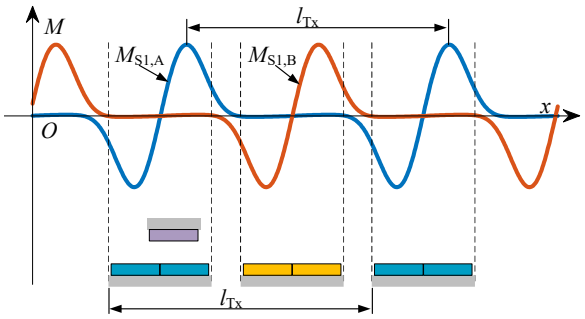

Figure 5.5: Magnetic coupling curves between one Rx sub-winding and the Tx winding phase A and phase B.

The magnetic coupling curves between one Rx sub-winding and the Tx winding phase A and phase B, $M_{S1,A}$ and $M_{S1,B}$, are presented in Fig. 5.5. Due to the even distribution of the Tx coils, $M_{S1,A}$ and $M_{S1,B}$ satisfy

$$M_{S1,B}(x) = M_{S1,A}(x + \frac{l_{Tx}}{2}). \tag{5.4}$$

Despite that $M_{S1,A}$ and $M_{S1,B}$ are discontinuous in x direction, the magnetic coupling curve has a sinusoidal-like shape when the Rx sub-winding is above a Tx coil, which is the foundation of a multiphase DIPT system to have a stable pick-up power as proved by (5.3).

To maintain a stable pick-up power, the magnetic coupling curves of phase A and phase B should have a spatial offset equal to a quarter of the period of the sinusoidal shape, as illustrated in Fig. 5.2. However, the curves of $M_{S1,A}$ and $M_{S1,B}$ has a spatial offset equal to half of the period length as shown in Fig. 5.3. To address this issue, a second Rx sub-winding is adopted to build the Rx side. The magnetic coupling curves between the Rx winding (sub-winding 1 and sub-winding 2) and the Tx winding phase A and phase B, $M_{S2,A}$ and $M_{S2,B}$, are presented in Fig. 5.6. l_{Rx} is the spatial offset between Rx sub-winding

1 and Rx sub-winding 2, and is illustrated in Fig. 5.3 and Fig. 5.6. Both $M_{S2,A}$ and $M_{S2,B}$ are dependent on l_{Rx}, which can be expressed as

$$M_{S2,A}(x) = M_{S1,A}(x) + M_{S1,A}(x + l_{Rx}), \tag{5.5a}$$

$$M_{S2,B}(x) = M_{S2,A}(x + \frac{l_{Tx}}{2}). \tag{5.5b}$$

Although both $M_{S2,A}$ and $M_{S2,B}$ are not globally sinusoidal, the curves within segments 1, 2 and 3 are still locally sinusoidal-like. It is defined that φ_A and φ_B are the phases of the sinusoidal curves within the specified segments, and l_{sin} is the period length of the sinusoidal curves within the specified segments. When $x \in$ segments 1, 2, and 3, one can get

$$M_{S2,A}(x) \approx M_0 sin(\frac{2\pi x}{l_{sin}} + \varphi_A(l_{Rx}, l_{Tx}, l_{sin})), \tag{5.6a}$$

$$M_{S2,B}(x) \approx M_0 sin(\frac{2\pi x}{l_{sin}} + \varphi_B(l_{Rx}, l_{Tx}, l_{sin})). \tag{5.6b}$$

As per (5.6), φ_A and φ_B are functions of l_{Rx}, l_{Tx}, and l_{sin}. Based on (5.6), $\mathbf{U}_{RxS}$ can be calculated as

$$\begin{aligned}\mathbf{U}_{RxS} =& j\omega M_0 I_{Tx} sin(\frac{2\pi x}{l_{sin}} + \varphi_A(l_{Rx}, l_{Tx}, l_{sin}))e^{j0} \\ &+ j\omega M_0 I_{Tx} sin(\frac{2\pi x}{l_{sin}} + \varphi_B(l_{Rx}, l_{Tx}, l_{sin}))e^{j\frac{\pi}{2}}.\end{aligned} \tag{5.7}$$

l_{sin} is determined by the dimension of the coils and the air gap. l_{Tx} is determined by the gap between two adjacent Tx coils. l_{Rx} is determined by the gap between the Rx sub-winding 1 and sub-winding 2. By optimizing the deployment of the Rx and Tx coils, the optimal l^*_{Tx} and l^*_{Rx} can be found to keep the difference between φ_A and φ_B to be close to $\frac{\pi}{2}$. Therefore, when $x \in$ segment 1, 2 and 3, the optimal $\mathbf{U}^*_{RxS}$ can be expressed as

$$\begin{aligned}\mathbf{U}^*_{RxS} \approx& j\omega M_0 I_{Tx}(sin(\frac{2\pi x}{l^*_{sin}} + \varphi_A(l^*_{Rx}, l^*_{Tx}, l^*_{sin})) \\ &+ jcos(\frac{2\pi x}{l^*_{sin}} + \varphi_A(l^*_{Rx}, l^*_{Tx}, l^*_{sin}))) \\ \approx& -\omega M_0 I_{Tx} e^{-j(\frac{2\pi x}{l^*_{sin}} + \varphi_A(l^*_{Rx}, l^*_{Tx}, l^*_{sin}))},\end{aligned} \tag{5.8}$$

where the superscript * indicates the optimal solution to keep $\varphi_A - \varphi_B \approx -\frac{\pi}{2}$. As proved by (5.8), the norm of $\mathbf{U}^*_{RxE}$ is a constant value when $x \in$ segment 1, 2 and 3. When $x \notin$ segments 1, 2 and 3, the pick-up power may change in a relatively larger fluctuation but remains seamless. Considering that the Tx gap is commonly much smaller than the size of the Tx coil, the proposed segmented DIPT system can deliver low-ripple pick-up power. Meanwhile, the proposed segmented DIPT system can reduce the Litz wire used to build the Tx track in comparison with the conventional elongated DIPT system in Fig. 5.1.

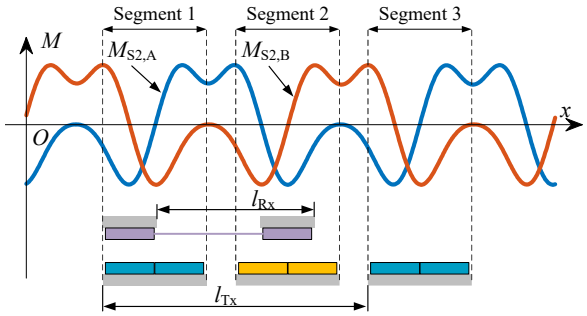

Figure 5.6: Magnetic coupling curves between two Rx sub-windings connected in series and the Tx winding phase A and phase B.

5.3 Fast Optimization of the Segmented DIPT System

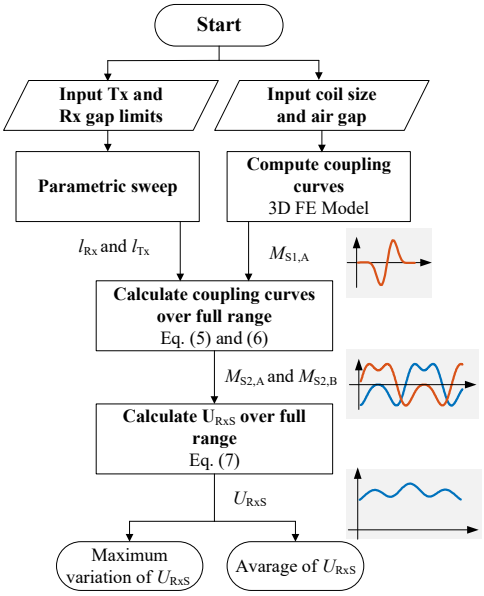

Figure 5.7: Flow chart of the fast optimization method.

To find the value of l_{Rx}^* and l_{Tx}^* for a given design of a magnetic coupler, an optimization method is presented in this section, and the flow chart is depicted in Fig. 5.7. The proposed optimization first employs a 3D FE model to compute the magnetic coupling curve of $M_{S1,A}$. Then, the parametric sweep output of l_{Rx} and l_{Tx} is combined with the computed $M_{S1,A}$ to calculate $M_{S2,A}$ and $M_{S2,B}$ according to (5.5) and (5.6). After obtaining the curves of $M_{S2,A}$ and $M_{S2,B}$, the Rx side induced voltage U_{RxS} is calculated by setting $I_{Tx} = 10$ A based on (5.7). To evaluate the performances of DIPT systems using different l_{Rx} and l_{Tx}, ΔU_{RxS} (the variation of $U_{RxS}(x)$) and $avg[U_{RxS}]$ (the average of $U_{RxS}(x)$) in the studied x range $[0, x_T]$

are used and defined as

$$\Delta U_{\mathrm{RxS}} = \frac{max[U_{\mathrm{RxS}}(x)] - min[U_{\mathrm{RxS}}(x)]}{2}, \tag{5.9a}$$

$$avg[U_{\mathrm{RxS}}] = \frac{1}{x_{\mathrm{T}}} \int_0^{x_{\mathrm{T}}} U_{\mathrm{RxS}}(x)dx. \tag{5.9b}$$

The studied coil structure is presented in Fig. 5.8. The design specifications are listed in Table 5.2. The structures and size of coils are used to build the 3D FE model as shown in Fig. 5.9. The search space of l_{Tx} and l_{Rx} are $560-1560$ mm and $280-590$ mm, respectively. By following the proposed optimization procedure introduced in Fig. 5.7, the results of ΔU_{RxS} and $avg[U_{\mathrm{RxS}}]$ are illustrated in Fig. 5.10.

On one hand, ΔU_{RxS} should be minimized to reduce the fluctuation of the pick-up power. On the other hand, $avg[U_{\mathrm{RxS}}]$ should be maximized, so the power transfer capability of the DIPT system can be improved. Therefore, the area where both ΔU_{RxS} and $avg[U_{\mathrm{RxS}}]$ are improved is highlighted by a circle in Fig. 5.10. By setting minimizing ΔU_{RxS} as the highest priority, an optimal solution is found where $l^*_{\mathrm{Rx}} = 0.415$ mm and $l^*_{\mathrm{Tx}} = 0.680$ mm. When the Tx side winding current $I_{\mathrm{Tx}} = 10$ A, the optimum performances are $\Delta U_{\mathrm{RxS}} = 18.3$ V and $avg[U_{\mathrm{RxS}}] = 107.0$ V. The curve of U_{RxS} in the studied range of x is presented in Fig. 5.11 where the ripple of U_{RxS} is globally below 17.1%.

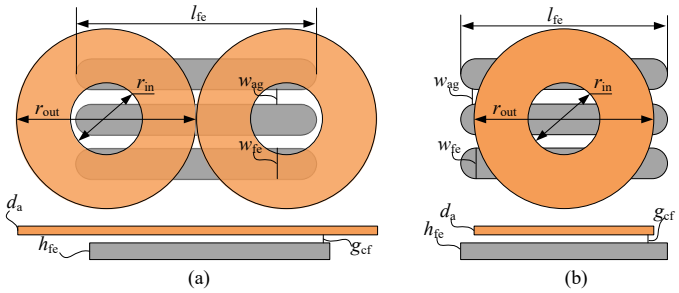

Figure 5.8: Structure of the studied coils, (a) Tx side DD coil, (b) Rx side sub-winding.

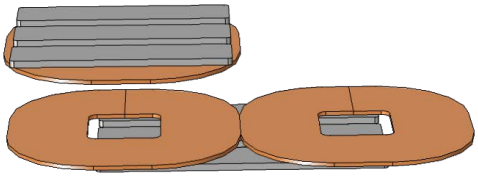

Figure 5.9: 3D FE model of the studied coils to compute $M_{\mathrm{S1,A}}$.

Table 5.2: Specifications of the coils

Variables	Symbol	Unit	Tx/Rx
Vertical clearance	Z_{ag}	mm	50
Number of turns	N	-	20/20
Inner radius	l_{in}	mm	44/44
Outer radius	w_{in}	mm	280/280
Ferrite bar thickness	h_{fe}	mm	4.1/4.1
Ferrite bar width	w_{fe}	mm	28/28
Ferrite bar length	l_{fe}	mm	172/129
The gap between ferrite bars	w_{ag}	mm	12/12
Litz wire radius	d_a	mm	2.4/2.4
Gap between coil and ferrites	g_{cf}	mm	3/3

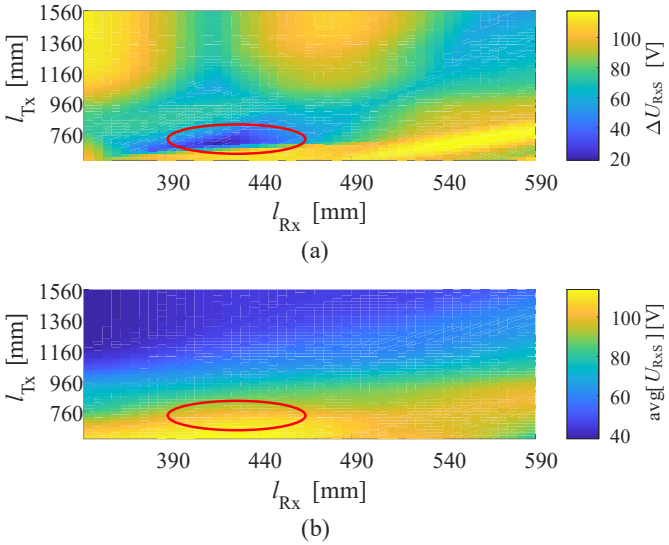

Figure 5.10: The results of ΔU_{RxS} and $avg[U_{RxS}]$ within the studied search space of l_{Rx} and l_{Tx}.

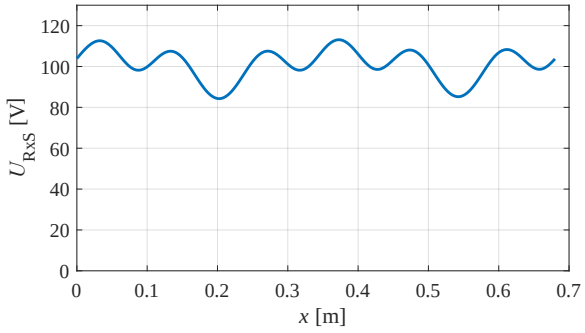

Figure 5.11: The curve of U_{RxS} when $l^*_{Rx} = 0.415$ mm and $l^*_{Tx} = 0.680$ mm.

5.4 Experimental Verification

To verify the performances of the proposed segmented DIPT system, a prototype is built as shown in Fig. 5.12. The details of the circuit components are listed in Tab. 5.3. It should be mentioned that the computed L_{Tx} is 134 μH and higher than the measured value due to the fabrication error in the coils. This also results in an error in the curve of $M_{\mathrm{S1,A}}$ between the measurement and FE model. For example, the measured $max[M_{\mathrm{S1,A}}]$ is 16.7 μH while the computed value is 20.1 μH.

The resonant circuit is connected as shown in Fig. 5.4. The self-inductance of one Rx side sub-winding is 55.6 μH which is half of L_{Rx}, so the two Rx side sub-windings have zero magnetic couplings. The input DC voltage to these two inverters is 60 V. The rectifier is connected to a 50 Ω resistive load. The movement of the Rx side coils is controlled via a motor, so the Rx side can move at a constant speed.

Considering that the Rx side is not moving at a high speed, the system can be seen to be in a steady state at each location. Therefore, the curve of u_{rec} and the envelope of u_{RxS} should be the same in terms of the average value and the ripple. By analyzing the data shown in Fig. 5.13(b), we can obtain that $avg[u_{\mathrm{rec}}] = 24.1$ [V], $\Delta u_{\mathrm{rec}} = 12.0$ [V] and the ripple is 24.9%. The measured ripple is 7.8% larger than the simulated result, which is acceptable because the real coils deviate from the FE model in their size and air gap. For example, the Tx DD coil self-inductance is computed to be 134 μH while the measurement is 121.6 μH. The difference between the prototype and the FE model results in an increment of the ripple of u_{rec}.

The measured Rx side induced voltage u_{RxS} and the rectified voltage to the load resistor u_{rec} are illustrated in Fig. 5.13. The measured envelope of u_{RxS} changes in the same pattern as the simulated result in Fig. 5.11, which verifies the advantage of the proposed DIPT system in delivering a low-ripple pick-up power.

Table 5.3: Details of the circuit components.

Variables	Symbol	Unit	Value
Tx coil	L_{Tx}	μH	121.6
Rx coil	L_{Rx}	μH	111.2
Tx side compensation inductor	L_{f1}	μH	71.1
Rx side compensation inductor	L_{f2}	μH	47.2
Tx side parallel capacitor	C_{f1}	nF	48.0
Rx side parallel capacitor	C_{f2}	nF	74.9
Tx side series capacitor	C_{s1}	nF	51.6
Rx side series capacitor	C_{s2}	nF	54.5

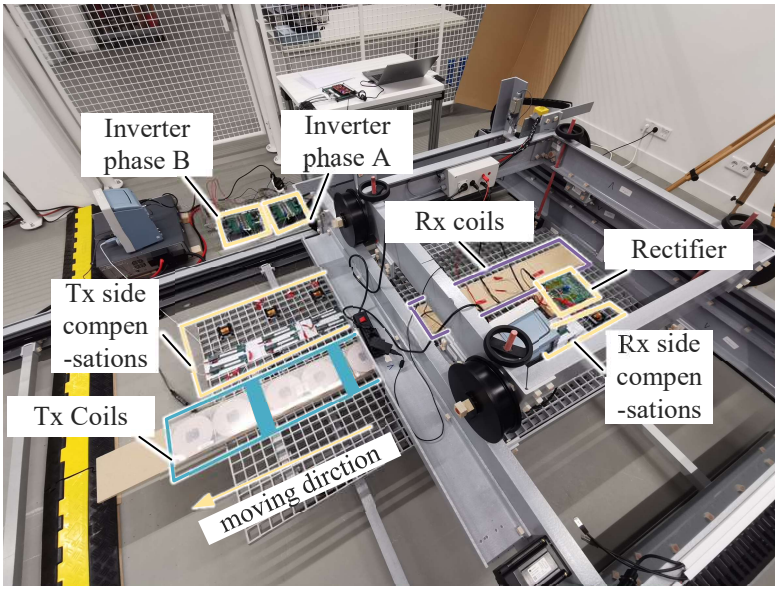

Figure 5.12: Picture of the designed DIPT prototype.

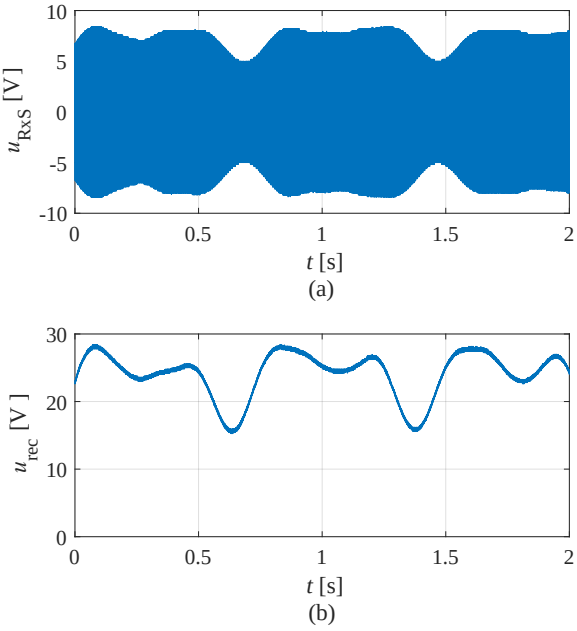

Figure 5.13: Experimental results of the designed DIPT prototype.

5.5 Conclusions

This paper presents the design of a new magnetic coupler mechanism for DIPT systems to achieve low-ripple pick-up power. The Tx track is composed of DD coils that are loosely deployed and powered by two inverters with a $\frac{\pi}{2}$ phase difference. The Rx side consists of two unipolar sub-windings spatially separated by a relatively large distance. By optimizing the distance between adjacent Tx DD coils and the distance between the two Rx sub-windings, the fluctuation of the pick-up power can be minimized. Based on the proposed optimization method, the ripple of the pick-up power can be maintained globally below 17.1% for the studied design of the coils. Finally, a DIPT prototype is built according to the optimization results. The measured curve of the DC voltage across the load changes in the same pattern as the calculated results with a ripple 7.8% higher due to the fabrication error of coils.

6

Electric Vehicles and Foreign Objects Detection

One of the challenges with the dynamic inductive power transfer (DIPT) technique is the electric vehicle detection (EVD) that helps the DIPT system to control the power supply of the transmitter. The EVD method applying auxiliary coils is a promising candidate because the flat shape of the auxiliary coils is suitable for the compact design. However, the EVD may fail when the metallic foreign object (MFO) is present. Therefore, the desire emerges in the integration design of the EVD and foreign object detection (FOD). The FOD can ensure the reliability of the EVD as well as the highly efficient operation of the DIPT system without MFOs. In this context, this paper proposes an integrated solution to the EVD and FOD well suited for DIPT systems. The integrated solution utilizes both passive coil sets (PCSs) and active coil sets (ACSs). Additionally, a novel detection resonant circuit (DRC) is proposed to realize EVD and FOD using the same coil sets and to amplify the measurement sensitivity. The operation mechanisms, the detection coil sets architecture, the design of the proposed resonant circuits and the detection procedure are detailed. Finally, a printed circuit board based prototype is built to validate the integrated functionality of the EVD and FOD in a DIPT prototype processing 1 kW *output. Experiments considering the practical DIPT application scenarios are conducted, and the proposed detection method is able to achieve advantageously high sensitivity and no blind zone.*

This chapter is based on:

- W. Shi, J. Dong, T. B. Soeiro, P. Bauer, *"Integrated solution for electric vehicle and foreign object detection in the application of dynamic inductive power transfer"*, *IEEE Transactions on Vehicular Technology*, 70(11):11365-11377.

6.1 Introduction

The dynamic IPT (DIPT) system for EVs enables battery charging while driving on the road [20, 92]. This can be used to reduce the required battery size and/or to extend the driving range. In a typical DIPT system, transmitters (Tx) are usually segmented charging pads [104, 110–112] or elongated tracks [18, 22, 113, 114] embedded under the road surface. When segmented charging pads are deployed, if all Txs are turned on, those uncoupled with the Rx will give rise to unnecessary power losses as well as leakage magnetic field which may be hazardous to nearby human beings and animals [49, 50]. Therefore, the DIPT Tx should be turned ON/OFF depending on the position of the EV [51, 53–61], which makes an EV detection (EVD) function necessary. The EVD method employing auxiliary coils on both the Tx and Rx sides is preferred because these auxiliary coils are flat and can be integrated into the charging pads. However, metallic foreign objects (MFOs) can considerably change the self-inductance of Tx side auxiliary coils and the coupling with the Rx side auxiliary coils [69, 115], which may cause the failure of the EVD function. Therefore, foreign object detection (FOD) also becomes necessary to ensure the reliability of the EVD. Moreover, the FOD can also protect the DIPT system from low-efficiency operation and potential hazards led by MFOs.

In the literature, the research topics of EVD and FOD are mostly discussed separately. Although the reported auxiliary coil arrays in [52] can realize FOD and EVD when the Tx and Rx are operating, this method is not suitable for DIPT applications where the Tx should not be energized before identifying the position of EVs. The operation of the EVD using auxiliary coils can be affected by the MFO. This makes the FOD essential to maintain the reliability of the EVD, while the research gap lying in the integrated design of the EVD and FOD has not been addressed in DIPT applications. Herein, in order to detect EVs and MFOs effectively at low cost, this chapter proposes and develops a new integrated detection method based on PCSs and ACSs. A core part of the proposed detection method is the detection resonant circuit (DRC) which improves the detection sensitivity and enables the ACSs to process the detection signals for both EVD and FOD. Compared with the existing literature, the proposed work achieves a zero-blind-zone for FOD without any coordinating switches to control the ACSs, and realizes EVD using the same set of circuits. This chapter analyses the detailed operation mechanism and validates the proposed concept in experiments.

This chapter will first introduce the operating principles of EVD and FOD. Then, the proposed method is compared with the state of the art to highlight the contribution. Motivated by the introduced operating principles, we propose an integrated detection solution. Later, the operating procedure of the proposed detection system is detailed. Finally, PCB coils and DRC are adapted into a 1 kW IPT system to validate the performance of the proposed integrated functionality of EVD and FOD.

6.2 Detection Principles

6.2.1 EVD Using Auxiliary Coil Sets

To achieve EVD, auxiliary coil sets are deployed on both the Tx and Rx pads. As presented in Fig. 6.1, the EV source coil (EVSC) is deployed onto the Rx pad to constantly produce the high frequent magnetic field. The high frequent magnetic field is sensed by the EVD

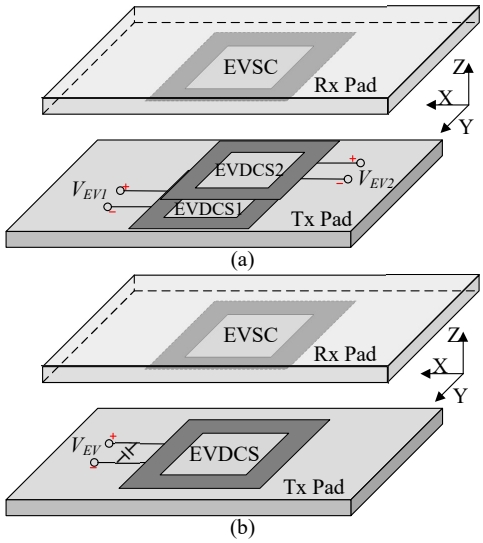

Figure 6.1: EVD methods using auxiliary coil sets, (a) EVD method reported in [60], (b) proposed EVD method

coil sets (EVDCS) applied onto the Tx pad. The phase and amplitude of the induced voltage in the EVDCS can be used to identify the position of the EV. The work in [60] proposed an EVD method detecting the phase of the induced voltage as shown in Fig. 6.1(a). This method applies two auxiliary coils (EVDCS1 and EVDCS2) onto the Tx pad with a spatial offset along the traveling direction. As shown in Fig. 6.2, the polarity of the mutual inductance M_{EVD} changes when the Rx pad approaches. Due to the spatial offset between the EVDCS1 and EVDCS2, there is an effective region where the polarities of their mutual inductance are opposite as highlighted in Fig. 6.2. By multiplying the induced voltages in EVDCS1 and EVDSC2 through an analog multiplier, the detection signal can be triggered when the Rx pad enters the effective region. However, the presence of MFO can lead to a change of M_{EVD}. As shown in Fig. 6.2, the effective region is minimal when the MFO is placed on EVDCS1 and the detection may fail.

In this chapter, we propose an EVD method whose auxiliary coils can also be used for the FOD to ensure the reliability of the EVD. The proposed EVD method uses the amplitude of the induced voltage in EVDCS. It is not practical to directly measure the induced voltage in EVDCS, because M_{EVD} is low and the current through the EVSC should be limited to reduce the power loss. As a result, the induced voltage in the EVDCS might be too low to be distinguishable. To solve this problem, capacitors are applied to form a series resonant circuit with the EVDCS as shown in Fig. 6.1(b). The phasor voltage across the capacitor $\mathbf{V}_{\mathrm{EV}}$ can be expressed as

$$\begin{cases} \mathbf{V}_{\mathrm{EV}} = -jQ_{\mathrm{EVDCS}}\omega_{\mathrm{EVD}}M_{\mathrm{EVD}}\mathbf{I}_{\mathrm{EVSC}} \\ Q_{\mathrm{EVDCS}} = \dfrac{\omega_{\mathrm{EVD}}L_{\mathrm{EVDCS}}}{R_{\mathrm{EVDCS}}} \end{cases} \tag{6.1}$$

where Q_{EVDCS} denotes the quality factor of the EVDCS, L_{EVDCS} and R_{EVDCS} are the self-

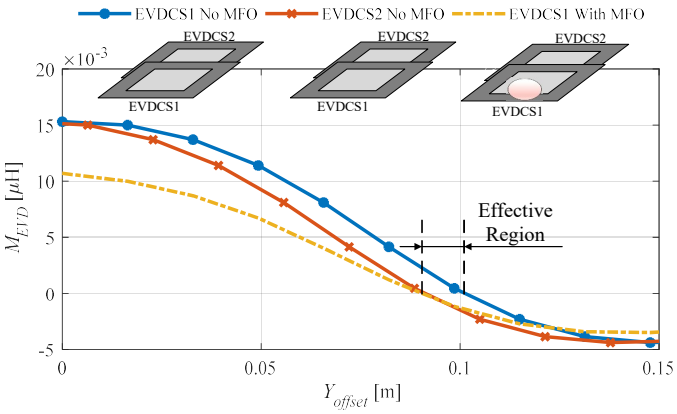

Figure 6.2: Influence of MFOs on the reliability of the EVD method

inductance and resistance of the EVDCS, respectively. ω_{EVD} and $\mathbf{I}_{\mathrm{EVSC}}$ are the angular switching frequency and phasor current amplitude of the EVSC, respectively. It can be seen that $\mathbf{V}_{\mathrm{EV}}$ is amplified by Q_{EVDCS}.

To ensure the reliability of the EVD, the interference from the main magnetic field and MFOs has to be addressed. Regarding the main magnetic field interference, the EVSC and EVDCS both should be decoupled from the charging pad, and the frequency of the EVSC current should be much higher than the rated charging frequency of 85 kHz, such that the induced voltage in EVDCS at 85 kHz can be attenuated by the DRC. When the MFO is placed on the EVDCS, its self-inductance drops [69] which could detune the DRC and the detection may fail. Therefore, it is essential to conduct FOD to ensure there is no MFO around the EVDCS.

6.2.2 FOD Using PCSs

As illustrated in Fig. 6.3(a), the PCS is deployed onto the Tx pad to sense the variation of the magnetic field caused by MFOs. The variation of the magnetic field can be measured through the induced voltage of the PCSs. The FOD sensitivity S_{PCS} is expressed as

$$S_{\mathrm{PCS}} = \left| \frac{\Delta V_{\mathrm{d}}}{V_{\mathrm{d}}} \right| \tag{6.2}$$

where V_{d} denotes the amplitude of the PCSs induced voltages, Δ represents the variation of a variable metric, e.g., voltage, caused by MFOs. To obtain high S_{PCS} to the MFO, one solution is to have V_{d} close to zero. Thus, it is necessary to keep the PCS decoupled from the Tx pad, which can be realized by selecting a proper topology and position for the PCS. Another solution of increasing S_{PCS} is to enlarge ΔV_{d}, and it can be achieved by decreasing the size of the PCS [66]. However, ΔV_{d} is distinguishable when the MFO is placed within the area enclosed by the PCS. Thus, multiple small PSCs are applied to cover the area of the Tx pad [52, 66, 67].

It is reported that a PCS consists of two subcoils and the PCS behaves as a bipolar coil as shown in Fig. 6.3(b) [52] and 6.3(c) [68]. By locating the PCSs properly according to the

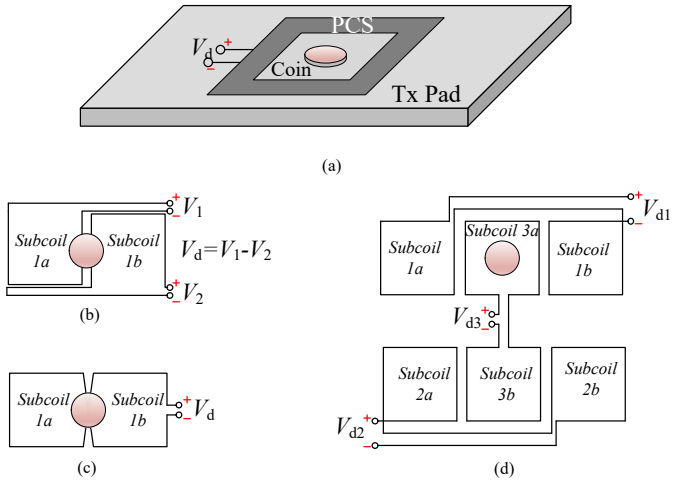

Figure 6.3: FOD methods using PCSs, (a) the deployment of PCSs, (b) non-overlapped topology [52], (c) overlapped topology [68], (d) proposed topology

feature of the main field, the total flux in each PCS can be minimal. Due to the symmetrical property of the PCSs in Fig. 6.3(b) and Fig. 6.3(c), the MFO symmetrically placed between two subcoils can hardly be detected and a blind zone emerges. To eliminate this blind zone, two layers of PCSs with a spatial offset are required [52, 68].

In this chapter, one proposes a new PCS topology dedicated for DD charging pads as shown in Fig. 6.3(d). To eliminate the blind zone of the bipolar PCS, a subcoil of a unipolar PCS is deployed between the subcoils of the bipolar PCS, and it is not necessary to have another layer of PCSs. It should be mentioned that the unipolar and bipolar PCSs should be deployed according to the symmetric property of the DD pad to ensure they are decoupled.

6.2.3 FOD Using ACSs

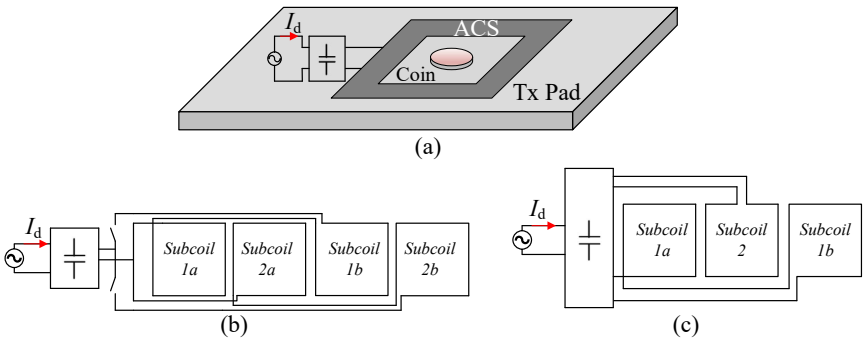

Figure 6.4: FOD methods using ACSs, (a) topology in [69], (b) proposed topology.

The ACS depicted in Fig. 6.4(a) is powered by a dedicated AC source, and capacitors are

applied to form the DRC. Instead of measuring the induced voltage like in the PCSs case, the magnitude of the input impedance Z_d is measured to identify the magnetic variation resulting from MFOs. When the MFO is coupled with the ACS, the self-inductance of the ACS L_{ACS} decreases [115]. ΔL_{ACS} can be measured through ΔZ_d. In the case that the MFO is of small size like coins, ΔL_{ACS} is minimal, while the corresponding ΔZ_d can be amplified by the DRC. The FOD sensitivity S_{ACS} is calculated as

$$S_{ACS} = \left|\frac{\Delta Z_d}{Z_d}\right| = G_r \left|\frac{\Delta L_{ACS}}{L_{ACS}}\right| \tag{6.3}$$

where G_r is the gain coefficient determined by the DRC. Since Z_d is measured by the amplitude of the input current I_d, the ACS is supposed to be decoupled with the Tx pad. To obtain high S_{ACS}, one approach is to design a DRC whose input impedance is sensitive to the resonance. Another approach is to decrease the size of the ACSs, such that the ratio of ΔL_{ACS} to L_{ACS} can be increased. However, if multiple ACSs are applied to cover the area of the Tx pad and operate at the same time, the coupling among ACSs will detune their DRC and switches should be applied [69] as shown in Fig. 6.4(b). In Fig. 6.4(b), a bipolar ACS is connected to a capacitor to form a parallel resonant circuit. To eliminate the blind zone, one subcoil of an ACS is placed between two subcoils of another ACS and switches are applied to avoid the simultaneous operation.

In this chapter, one proposes a new ACS topology dedicated for DD charging pads as presented in Fig. 6.4(c). This topology includes both unipolar and bipolar ACSs. The unipolar coil is deployed between the subcoils of the bipolar coil. According to the field property, these two ACSs are internally decoupled which means no switches are required and the design of the DRC is simplified.

6.2.4 Integration of EVD and FOD

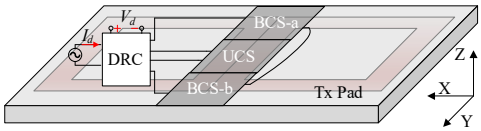

Figure 6.5: Proposed auxiliary coil deployment over a DD charging pad.

As discussed in Section II-A, the FOD should be conducted as an initializing step of the EVD. The FOD method using ACSs could be a good candidate because it can operate when the Tx is not energized. Then, the EVD and FOD rely on the DRC to amplify the magnetic field variation caused by the EVSC and MFO, respectively. This chapter proposes an integration design solution which can achieve EVD and FOD using the same auxiliary detection coil set. The integration design includes the topology of the DRC and the deployment of the auxiliary coils, which are presented in Fig. 6.5 and Fig. 6.6.

In Fig. 6.5, three auxiliary coils are applied to form a unipolar coil set (UCS) and bipolar coil set (BCS) consisting of BCS-a and BCS-b. The UCS and BCS are placed along the ZY symmetric plane of the Tx pad. The advantage of the proposed coil deployment is that the UCS and BCS are both decoupled with the Tx. The interference of the main field on EVD and FOD can be eliminated. Meanwhile, the UCS and BCS are also decoupled from each

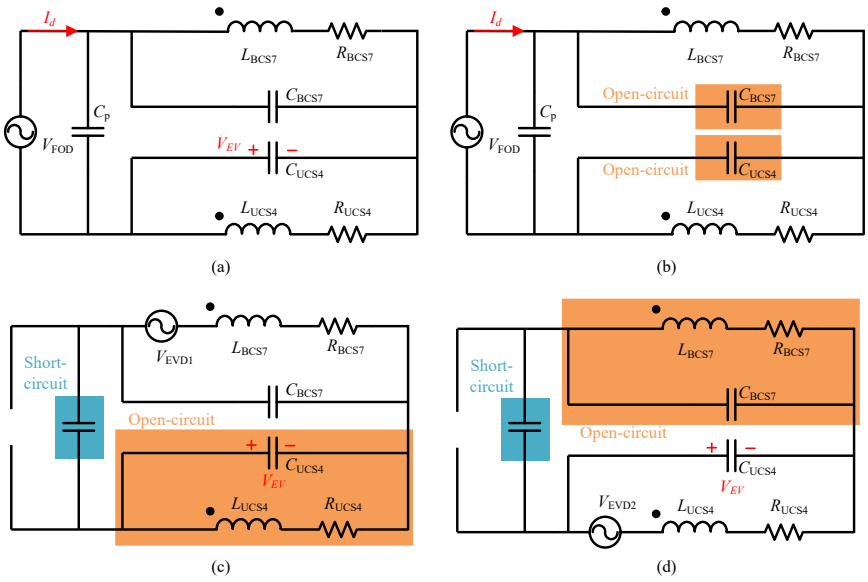

Figure 6.6: Proposed DRC, (a) topology, (b) low frequency mode, (c) and (d) high frequency mode. V_{FOD} is the voltage source for FOD. V_{EVD} is the induced voltage in the auxiliary coil sets resulting from the coupling with the EVSC.

6

other as depicted in Fig. 6.4(c). Thus, the UCS and BCS can be energized simultaneously as ACSs for FOD.

In Fig. 6.6, the proposed DRC adopts three capacitors (C_p, C_{BCS} and C_{UCS}) which are designed as follow

$$\begin{cases} \omega_{EVD} = 2\pi f_{EVD} \\ \omega_{FOD} = 2\pi f_{FOD} \\ C_{BCS} = \dfrac{1}{\omega_{EVD}^2 L_{BCS}} \\ C_{UCS} = \dfrac{1}{\omega_{EVD}^2 L_{UCS}} \\ C_p = \dfrac{1}{\omega_{FOD}^2 (L_{BCS} + L_{UCS})} \end{cases} \tag{6.4}$$

where L_{BCS} and L_{UCS} are the self-inductance of the BCS and UCS, respectively. When the operating frequency of the EVD f_{EVD} and FOD f_{FOD} satisfies $f_{FOD} << f_{EVD}$, the DRC can work in two different modes. When powered by the voltage source V_{FOD}, the DRC behaves in the low frequency mode as shown in Fig. 6.6(b). The parallel resonant tanks formed by L_{BCS} and C_{BCS} and by L_{UCS} and C_{UCS} have the input impedance phasor $\mathbf{Z}_{BCS,p}$ and $\mathbf{Z}_{UCS,p}$, respectively. $\mathbf{Z}_{BCS,p}$, $\mathbf{Z}_{UCS,p}$ and the input impedance phasor of the DRC $\mathbf{Z}_d$ can

be calculated as

$$\begin{cases} \mathbf{Z}_{\mathrm{BCS,p}} = \dfrac{j\omega_{\mathrm{op}} L_{\mathrm{BCS}} + R_{\mathrm{BCS}}}{j\omega_{\mathrm{op}} C_{\mathrm{BCS}} R_{\mathrm{BCS}} + 1 - \omega_{\mathrm{op}}^2 L_{\mathrm{BCS}} C_{\mathrm{BCS}}} \\ \mathbf{Z}_{\mathrm{UCS,p}} = \dfrac{j\omega_{\mathrm{op}} L_{\mathrm{UCS}} + R_{\mathrm{UCS}}}{j\omega_{\mathrm{op}} C_{\mathrm{UCS}} R_{\mathrm{UCS}} + 1 - \omega_{\mathrm{op}}^2 L_{\mathrm{UCS}} C_{\mathrm{UCS}}} \\ \mathbf{Z}_{\mathrm{d}} = \dfrac{(Z_{\mathrm{BCS,p}} + Z_{\mathrm{UCS,p}})}{j\omega_{\mathrm{op}} C_{\mathrm{p}} (Z_{\mathrm{BCS,p}} + Z_{\mathrm{UCS,p}}) + 1} \end{cases} \tag{6.5}$$

where ω_{op} is the operating angular frequency. When $\omega_{\mathrm{op}} = \omega_{\mathrm{FOD}}$, $\mathbf{Z}_{\mathrm{BCS,p}}$ and $\mathbf{Z}_{\mathrm{UCS,p}}$, according to the design requirements in (6.4), can be simplified as

$$\mathbf{Z}_{\mathrm{BCS,p}} \approx j\omega_{\mathrm{FOD}} L_{\mathrm{BCS}} + R_{\mathrm{BCS}} \tag{6.6a}$$

$$\mathbf{Z}_{\mathrm{UCS,p}} \approx j\omega_{\mathrm{FOD}} L_{\mathrm{UCS}} + R_{\mathrm{UCS}} \tag{6.6b}$$

C_{UCS} and C_{BCS} can be seen as open-circuit. Thus, the DRC becomes a parallel resonant circuit comprised of C_{p}, L_{UCS} and L_{BCS}. When the DRC operates at f_{FOD}, its input impedance phasor $\mathbf{Z}_{\mathrm{d}}$ can be approximated as

$$\begin{cases} \mathbf{Z}_{\mathrm{d}} \approx (Q_{\mathrm{FOD}} - j)\omega_{\mathrm{FOD}}(L_{\mathrm{BCS}} + L_{\mathrm{UCS}}) \\ Q_{\mathrm{FOD}} = \dfrac{\omega_{\mathrm{FOD}}(L_{\mathrm{BCS}} + L_{\mathrm{UCS}})}{R_{\mathrm{BCS}} + R_{\mathrm{UCS}}} \end{cases} \tag{6.7}$$

The resistive part of $\mathbf{Z}_{\mathrm{d}}$ is large due to the quality factor Q_{FOD} which can be as high as tens. Since $\mathbf{Z}_{\mathrm{d}}$ is sensitive to the resonance [69, 116], Z_{d} will reduce significantly when there are MFOs as shown in Fig. 6.7. Thus, by measuring the increment of I_{d}, the MFO can be detected.

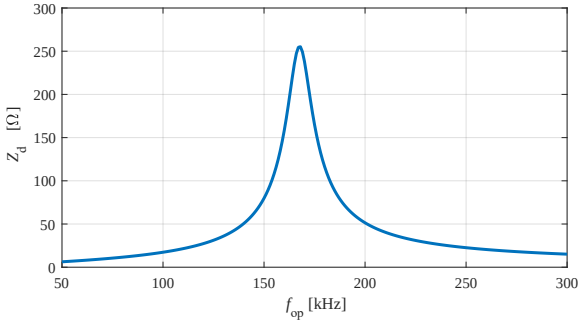

Figure 6.7: Frequency response of $\mathbf{Z}_{\mathrm{d}}$, $\omega_{\mathrm{FOD}} = 170$kHz.

When the EVSC is present, there will be the induced voltage $\mathbf{V}_{\mathrm{EVD}}$ in the BCS and UCS and the DRC will operate in the high frequency mode as presented in Fig. 6.6(c) and 6.6(d). When $\omega_{\mathrm{op}} = \omega_{\mathrm{EVD}}$, based on (6.5) $\mathbf{Z}_{\mathrm{BCS,p}}$ and $\mathbf{Z}_{\mathrm{UCS,p}}$ can be calculated as

$$\begin{cases} \mathbf{Z}_{\mathrm{BCS,p}} = (Q_{\mathrm{EVD}} - j)\omega_{\mathrm{EVD}} L_{\mathrm{BCS}} \\ \mathbf{Z}_{\mathrm{UCS,p}} = (Q_{\mathrm{EVD}} - j)\omega_{\mathrm{EVD}} L_{\mathrm{UCS}} \\ Q_{\mathrm{EVD}} = \dfrac{\omega_{\mathrm{EVD}} L_{\mathrm{BCS}}}{R_{\mathrm{BCS}}} = \dfrac{\omega_{\mathrm{EVD}} L_{\mathrm{UCS}}}{R_{\mathrm{UCS}}} \end{cases} \tag{6.8}$$

Due to the high coil quality factor Q_{EVD}, $Z_{BCS,p}$ and $Z_{UCS,p}$ are far lager than the reactance of C_{BCS} and C_{UCS}. When V_{EVD} is the input, the DRC behaves like a series resonant circuit consisting of L_{BCS} (L_{UCS}) and C_{BCS} (C_{UCS}). Thus, $\mathbf{V}_{EV}$ can be approximated as

$$\mathbf{V}_{EV} \approx jQ_{EVD}\omega_{EVD}\mathbf{I}_{EVSC} \times (M_{EVD,BCS} + M_{EVD,UCS}) \tag{6.9}$$

where V_{EV} is Q_{EVD} times as high as V_{EVD}. By comparing the measured V_{EV} with a predefined value, the EVD can be realized.

6.2.5 Deployment of Auxiliary Coil Sets

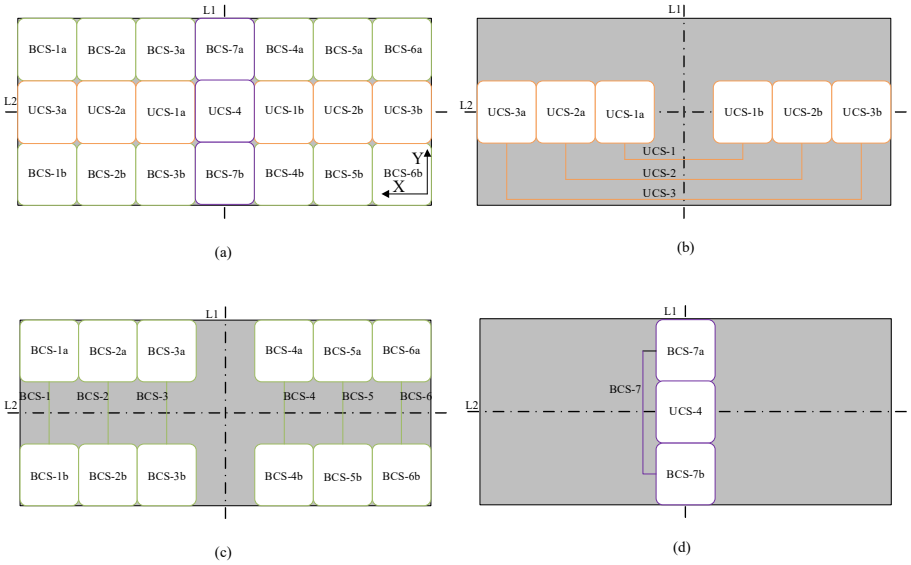

Figure 6.8: Arrangement of auxiliary coil sets (a) overview, (b) and (c) PCSs, and (d) ACSs. L1 is the projection of the ZY symmetrical plane on the XY plane. L2 is the projection of the ZX symmetrical plane on the XY plane.

As the MFO may weaken the coupling between the Tx and the Rx pads and lead to extra eddy current losses, the FOD function should be effective over the area enclosed by the Tx pad. In Section II-D, the integration design of EVD and FOD is presented. However, to ensure a high FOD resolution, the size of ACSs should be limited [66] and only part of the Tx pad can be covered by the ACSs. To eliminate the FOD blind zone, PCSs are adopted to cover the rest of the area of the Tx. The coil arrangement is presented in Fig. 6.8.

Both the UCS and BCS are adopted for PCSs. The deployment of PCSs is illustrated in Fig. 6.8(b) and 6.8(c). UCS-i (i = 1, 2 and 3) consists of two rectangular coils, UCS-ia and UCS-ib, which are arranged symmetrically at L1 and connected in opposing series. BCS-i (i=1, 2,..., 6) is composed of two rectangular coils, BCS-ia and BCS-ib, placed symmetrically at L2 but connected in aiding series. According to the magnetic field property of the DD pad, the total flux in UCSs and BCSs is close to zero, which means they are decoupled with the Tx pad and high S_{PCS} can be guaranteed. Since the BCS can hardly detect the MFO

placed on L2, a subcoil of the UCS is deployed in between BCS-ia and BCS-ib. Thus, the blind zone over the area covered by PCSs is eliminated.

The deployment of ACSs is presented in Fig. 6.8(d), including UCS-4 and BCS-7. The EVSC is a UCS placed onto the Rx pad. Assuming that the EV travels along the Y axis, the coupling between the EVSC and ACSs is presented in Fig. 6.9. Based on (6.9), the range of V_{EV} can be calculated which can be used to define the threshold value for EVD.

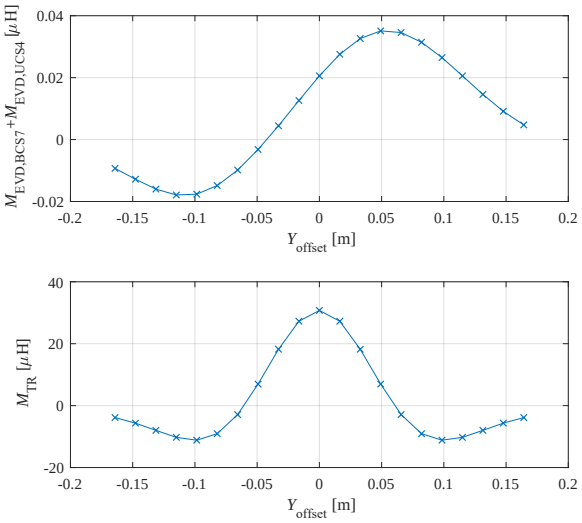

Figure 6.9: Mutual coupling for EVD and the main coupling between the Tx and Rx M_{TR} computed by the finite element model.

6.3 Detection Procedures

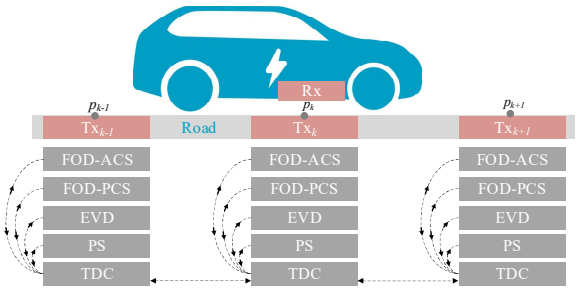

Figure 6.10: DIPT systems applying the proposed detection method.

In the proposed DIPT system shown in Fig. 6.10, each Tx has five modules, FOD-ACS, FOD-PCS, EVD, power supply (PS) and Tx detection controller (TDC). The FOD-ACS module consists of a low voltage AC power supply at f_{FOD}, the DRC and the ACSs. This is used to detect MFOs over the ACSs illustrated in Fig. 6.8(d), and it operates before the

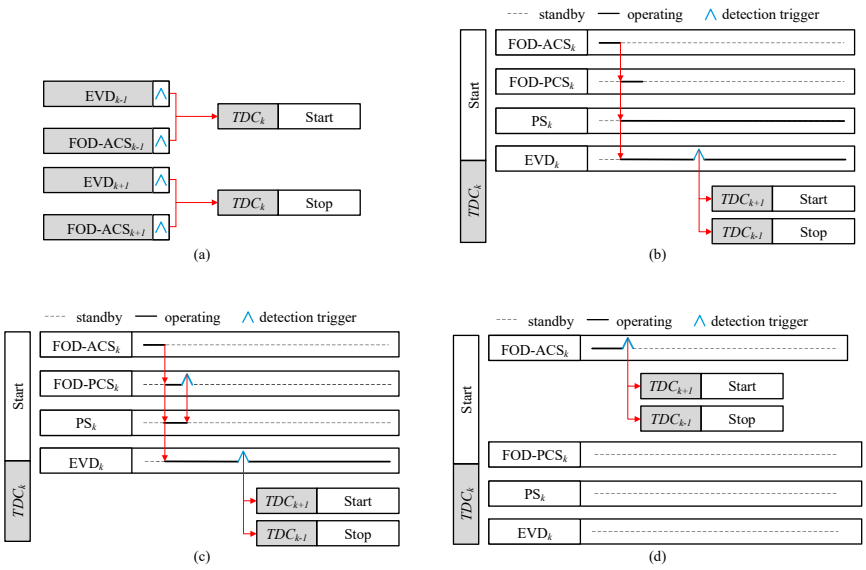

Figure 6.11: Detection procedures, (a) communications among Txs and detection logics when there is (b) no MFOs, (c) a MFO on PCSs and (d) a MFO on ACSs.

Tx is energized. The FOD-PCS module consists of the PCSs requiring no power supply and it is used to detect MFOs in the area enclosed by the PCSs. The Tx pad has to be energized before the FOD-PCS module starts to detect MFOs. The EVD module consists of the DRC and the ACSs. The EVSC coil is mounted on the Rx side and powered by a low voltage AC power supply at f_{EVD} which is constantly on. It is used to identify whether there is an EV aligned with the Tx. The PS module is the power source of the Tx pad. As shown in Fig. 6.10 the TDC module is used to receive the detection signals to control the operating sequence of each module and to communicate with the TDC module of adjacent Tx pads. It can enable and disable the FOD-ACS, FOD-PCS and EVD modules and process the detection results to determine the action of the PS module of the Tx. Thus, the PS can be switched on only when there are no MFOs and an EV is in the near range.

Due to the presence of resonant circuits in the Tx side, it takes some time for the winding current of the Tx pad to reach the rated value from its initial condition. To make full use of the limited effective charging zone of each Tx pad, it is practical to initialize and to start the Tx pad before the EV enters the effective charging zone. Therefore, $\mathrm{Tx_k}$ is designed to be started by the detection signal of $\mathrm{Tx_{k-1}}$ and to be stopped by the detection signal of $\mathrm{Tx_{k+1}}$ as shown in Fig. 6.11(a). The detailed detection logic is illustrated in Fig. 6.11(b), 6.11(c) and 6.11(d):

- Fig. 6.11(b), the detection trigger from $\mathrm{Tx_{k-1}}$ enables the FOD-ACS module. The FOD-ACS module finds no MFOs and disables itself. Meanwhile, the FOD-PCS module, PS module and EVD module are enabled. The FOD-PCS module finds no MFOs and disables itself. The PS module stays in operation mode until the detection trigger is received from $\mathrm{Tx_{k+1}}$. When the EV is aligned with $\mathrm{Tx_k}$, a detection trigger is sent to

stop Tx_{k-1} and start Tx_{k+1}.

- Fig. 6.11(c), the detection trigger from Tx_{k-1} enables the FOD-ACS module. The FOD-ACS module finds no MFOs and disables itself. Meanwhile, the FOD-PCS module, PS module and EVD module are enabled. The FOD-PCS module finds a MFO and disables itself and the PS module. When the EV is aligned with Tx_k, a detection trigger is sent to stop Tx_{k-1} and start Tx_{k+1}.
- Fig. 6.11(d), the detection trigger from Tx_{k-1} enables the FOD-ACS module. The FOD-ACS module finds a MFO and disables itself. Meanwhile, a detection trigger is sent to stop Tx_{k-1} and start Tx_{k+1}.

6.4 Experimental Verification

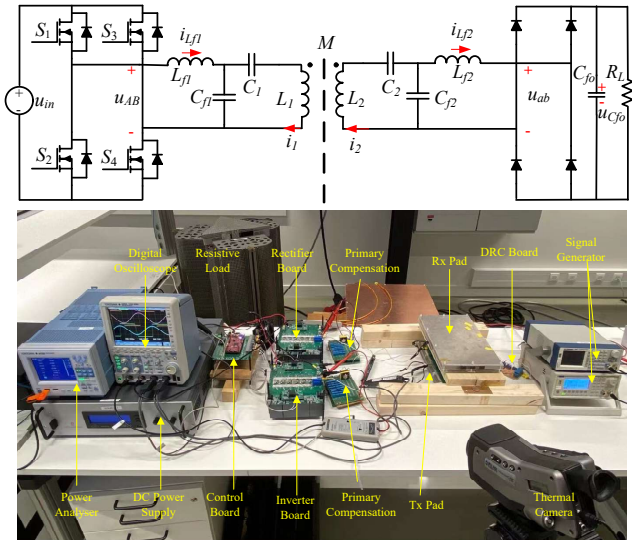

Figure 6.12: IPT charging system using double-sided LCC compensation and DD Tx and Rx coils.

In order to verify the proposed detection method, an IPT system is built as shown in Fig. 6.12. The Tx and Rx pads using DD coil topology are identical. The IPT system is compensated with double-sided LCC compensation tuned at 85 kHz. The IPT system circuit parameters are listed in Table I. Other details of the IPT system components are presented in Table II.

6.4.1 Design of Auxiliary Coils and DRC

As shown in Fig. 6.8, the deployment of auxiliary detection coils is determined by the axis of symmetry of the Tx pads, L1 and L2. To guarantee the geometrical features of the auxiliary detection coils, the PCB coils are designed as shown in Fig. 6.13 and Fig. 6.14. On the Tx side, there are twenty-one identical auxiliary detection coils. Each auxiliary detection coil has ten number of turns with a length and width of 42.6 mm*54.7 mm. On

Table 6.1: IPT SYSTEM CIRCUIT SPECIFICATIONS

Part	Unit	Value
L_1	μH	200.7
L_2	μH	203.5
M	μH	30
L_{f1}	μH	66.39
L_{f2}	μH	68.97
C_1	nF	26.87
C_2	nF	28.98
C_{f1}	nF	54.83
C_{f2}	nF	51.67
C_{fo}	μF	110
R_L	Ω	123

Table 6.2: COMPONENT SPECIFICATIONS OF THE IPT SYSTEM

Part	Property
Ferrite	Material type: P, number of bars: 3, length of bars: 220 mm
Litz wire	Type: AWG 41, number of strands: 525
Coil	Topology: DD-DD, number of turns: 30, size: 172*298 mm^2
Capacitor	Polypropylene film, 6.7 nF
MOSFET	IMZ120R030M1H

the Rx side, EVSC coil consists of one single coil having five turns with a length and width of 298 mm*164 mm. By using the impedance analyser (Agilent 4294A, 40 Hz to 110 MHz), the self-inductance and AC resistance R_{ac} of UCS-4 and BCS-7 are measured as listed in Table III.

In practice, it is hard to ensure that the auxiliary detection coils are strictly decoupled to the charging pads. The deflection and displacement of the PCB coil may lead to a certain coupling with the Tx pad. Therefore, it is essential to keep f_{PS} much smaller than f_{FOD} and avoid odd-order harmonics of the PS such that the harmonics at f_{PS} can be bypassed. To test the performance of the PCB coil, f_{FOD} is selected to be around 170 kHz. The EVD frequency is selected to be around 1 MHz which satisfies $f_{FOD} << f_{EVD}$. The capacitors in the DRC are designed to be 200 nF for C_p, 4.3 nF for C_{UCS4} and 2.2 nF for C_{BCS7}.

Table 6.3: COMPONENT SPECIFICATIONS OF THE IPT SYSTEM

Coil set	L [μH]	R_{ac} [mΩ]
UCS-4	6.05	470
BCS-7	11.63	889
EVSC	15.4	360

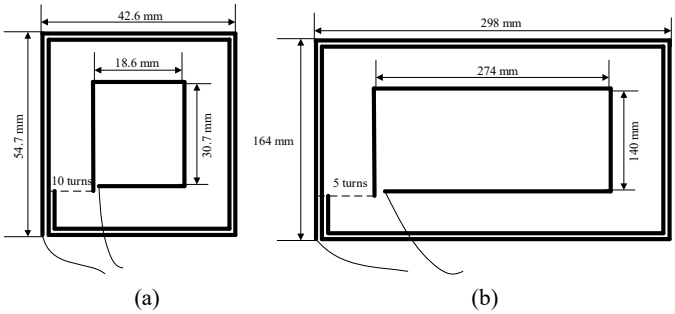

Figure 6.13: Dimension of (a) a single auxiliary detection coil, (b) EVSC.

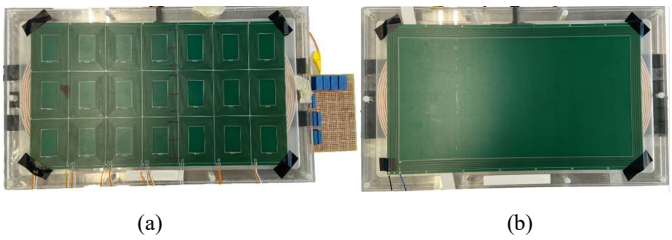

Figure 6.14: PCB coils integrated to the charging pads, (a) Tx pad, (b) Rx pad.

6.4.2 FOD Function Using ACSs

To verify the performance of FOD using the ACSs, a one-euro coin with a diameter of 23.25 mm and thickness of 2.33 mm is taken as the reference MFO. According to the detection procedure in Fig. 6.11, the FOD-ACS module operates when the Rx pad is absent and the PS is off. A signal generator is applied to feed the AC power at f_{FOD}. The ACSs, including BCS-7 and UCS-4, are used to build the DRC together with the capacitors C_{p}, C_{BCS7} and C_{UCS4}. By measuring the input voltage V_{FOD} and current I_{d}, the input impedance Z_{d} variation caused by the MFO is obtained. The MFO moves along the trajectory x1 as shown in Fig. 6.15.

As shown in Fig. 6.16(a), the waveforms of V_{FOD} and I_{d} are in-phase, indicating a resistive Z_{d} around 205.1 Ω. A high input impedance helps to reduce the power loss in the ACSs. Due to the intrusion of the MFO at (x1,P4) in Fig. 6.16(b), Z_{d} drops to 158.8 Ω, indicating a 22.6% reduction of Z_{d}. This is a consequence of a 3.9% reduction of the total self-inductance of the ACSs L_{ACS}.

Fig. 6.16(c) presents the full-range FOD performance of the ACSs. Compared with the curve of ΔL_{ACS}, ΔZ_{d} shows the same trend and an obvious positive scaling factor. It can be seen that ΔL_{ACS} becomes relatively high when the MFO is placed near the center of the ACSs, while the peaks are not at the center points P3, P9 and P15. According to [115], the self-inductance reduction of the ACS ΔL_{ACS} is determined by its coupling with the MFO as

$$\Delta L_{\mathrm{ACS}} = \frac{\omega_{\mathrm{FOD}}^2 M_{\mathrm{MFO,A}}^2 L_{\mathrm{MFO}}}{\omega_{\mathrm{FOD}}^2 L_{\mathrm{MFO}}^2 + R_{\mathrm{MFO}}^2} \tag{6.10}$$

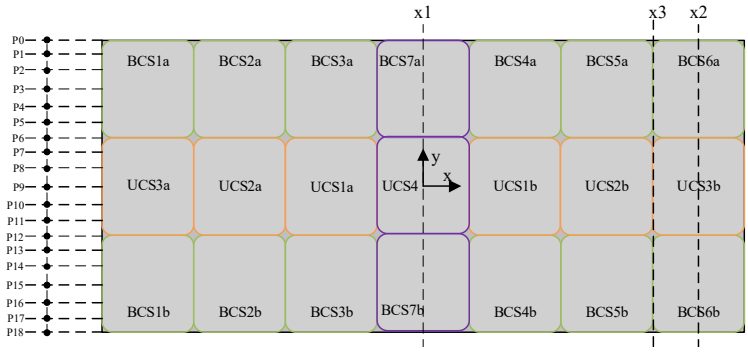

Figure 6.15: MFO locations for the FOD test. Trajectory x1 for FOD-ACS. Trajectories x2 and x3 for FOD-PCS. Under each trajectory, nineteen points are highlighted.

where L_{MFO}, $M_{\mathrm{MFO,A}}$ and R_{MFO} are the equivalent self-inductance, mutual inductance with the ACSs and resistance of the MFO, respectively. As illustrated in Fig. 6.17, the magnetic field becomes stronger at points close to the inner edges of the ACSs. Thus, $M_{\mathrm{MFO,A}}$ at points P2 and P4 is higher than that at point P3. Based on (6.10), ΔL_{ACS} at points P2 and P4 is also higher than that at point P3. The same reason can be applied to explain the dips at points P9 and P15. According to Fig. 6.7, ΔZ_{d} increases as the resonant frequency of the DRC deviates away from f_{FOD}. Therefore, ΔZ_{d} has the same trend as ΔL_{ACS}. The maximum ΔL_{ACS} is around 5% with the MFO at P2, P4, P8, P10, P14 and P16 and the corresponding ΔZ_{d} is higher than 17%. The influence of the MFO becomes weaker as it approaches the outer edge of the ACSs. The minimum ΔL_{ACS} is around 0.63% with the MFO at P0 and P18, while the corresponding ΔZ_{d} is about four times higher, around 2.6%. In summary, by virtue of the proposed DRC, the influence of the MFO on the ACSs is considerably amplified. The FOD of high sensitivity and no blind zone is achieved within the area enclosed by the ACSs.

6.4.3 FOD Function Using PCSs

According to the detection procedure in Fig. 6.11, the FOD-PCS module operates when the Rx pad is absent and the PS is on. The Tx pad is powered by a winding current I_1 of 1.88 Arms. With the intrusion of the MFO an increment of the induced voltage V_{d} can be observed from the studied PCSs, UCS-3 and BCS-6. The MFO moves along the trajectory x2 and x3 as shown in Fig. 6.15.

Fig. 6.18(a) and 6.18(b) present the waveforms of V_{d} when the MFO is placed at (x2, P8) and (x2, P2), where $V_{\mathrm{d,UCS3}}$ and $V_{\mathrm{d,BCS6}}$ are the measured induced voltage of UCS-3 and BCS-6, respectively. Fig. 6.18(c) shows the full-range FOD performance of the PCSs. The value of V_{d} is determined by the coupling of the MFO with the PCSs and the main field distribution. Based on (6.10), the self-inductance reduction of the PCS ΔL_{PCS} can reflect its coupling with the MFO $M_{\mathrm{MFO,P}}$ as

$$M_{\mathrm{MFO,P}} = \frac{1}{\omega_{\mathrm{PS}}} \sqrt{\frac{(\omega_{\mathrm{PS}}^2 L_{\mathrm{MFO}}^2 + R_{\mathrm{MFO}}^2)\Delta L_{\mathrm{PCS}}}{L_{\mathrm{MFO}}}} \tag{6.11}$$

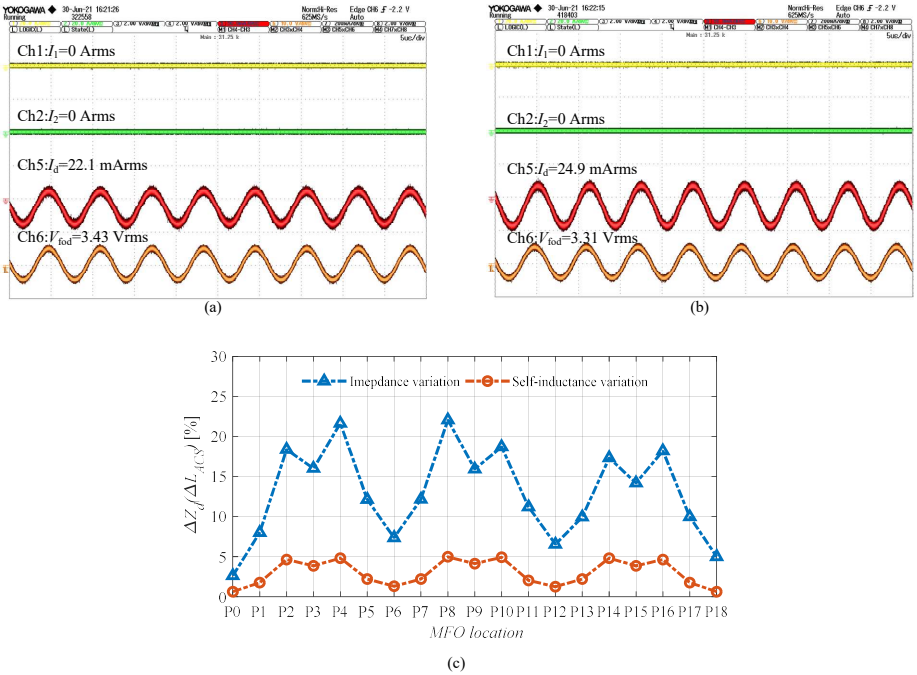

Figure 6.16: Experimental results of FOD using ACS. Waveforms of V_{FOD} and I_{d} (a) with no MFOs, and (b) with the MFO at (x1, P4), and (c) full-range performance when the MFO moves along trajectory x1.

where ω_{PS} is the angular frequency of the PS. Based on (6.11), Fig. 6.19(a) can prove that $M_{\mathrm{MFO,P}}$ at trajectory x2 is consistently higher than that at trajectory x3. However, the magnetic field at trajectory x3 is stronger than that at trajectory x2 as depicted in Fig. 6.19(b). As shown in Fig. 6.19(a), $M_{\mathrm{MFO,P}}$ at (x2, P8) is close to that at (x2, P2), while the magnetic field is higher at (x2, P8). As a result, V_{d} at (x2, P8) has a larger value than that at (x2, P2). Due to the magnetic field distribution, V_{d} of trajectory x2 is lower than that of trajectory x3 at points P0, P6, P12, and P18 although $M_{\mathrm{MFO,P}}$ of trajectory x2 is slightly higher. At other points, $M_{\mathrm{MFO,P}}$ of trajectory x2 are significantly higher than that of trajectory x3. As a consequence, V_{d} of trajectory x2 is higher than or close to that of trajectory x3 at these points. In summary, the proposed design of the PCSs can effectively identify MFOs within the area enclosed by the PCSs.

6.4.4 EVD Function Using ACSs

To validate the performance of the EVD using ACSs, the EVSC is powered by a signal generator at f_{EVD} and the ACSs are used to sense their coupling with the EVSC. The coupling between the ACSs and the EVSC increases when the Rx pad approaches to the Tx pad. The induced voltage in the ACSs can be amplified in V_{EV} by the DRC. Thus, by comparing with a predefined threshold voltage, the alignment condition of the Rx pad can be identified and the EVD can be accomplished with a high sensitivity.

According to the detection procedure in Fig. 6.11, the EVD module operates when

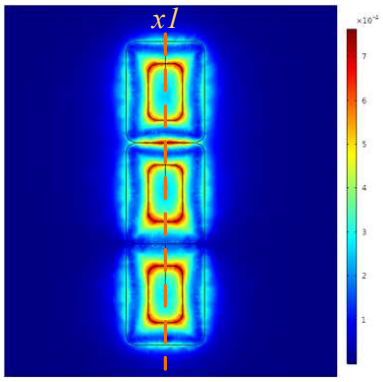

Figure 6.17: Magnetic field distribution (unit T) when 1 A current is applied to the ACSs.

there is no MFO on the ACSs and the PS can be either on or off. Fig. 6.20 presents the waveform of V_{EV} and I_{EVSC} when the Rx pad is aligned with the Tx pad. When the PS is off, the rms value of V_{EV} is 634 mV with I_{EVSC} equal to 50.1 mA, as shown in Fig. 6.20(a). In Fig. 6.20(b) the PS is on, and the rms value of V_{EV} slightly increases to 727 mV. It is because the EVSC is relatively large and not perfectly decoupled with the Rx pad, and the 85 kHz harmonics emerge in the waveform of I_{EVSC} and V_{EV}. The harmonics can be filtered, since the frequency of the harmonics is much smaller than f_{EVD}. In summary, the DRC formed by the ACSs can effectively identify the alignment condition of the EV by measuring the rms value of V_{EV}.

6.4.5 System Performances in Practical Scenarios

To investigate the influence of the detection modules on the power transfer, the dc-dc efficiency of the system is measured at 1 kW output power when the Rx is aligned with the Tx as illustrated in Fig. 6.21. Due to the presence of the PCB coils together with the DRC, the measured efficiency drops by 0.48%, which is minimal. Considering that the power analyser (YOKOGAMA WT500) has a basic measurement uncertainty about 0.1% of the reading plus 0.1% of the range, the efficiency difference led by the PCB coils is comparable with the measurement uncertainty.

To verify the performance of the proposed detection method, experiments are conducted considering the DIPT application scenarios as depicted in Fig. 6.22. It is assumed that the distance between two Tx pads is 28 cm. According to the detection procedures in Fig. 6.11, the FOD-ACS module is enabled when the Rx reaches p_{k-1} as shown in Fig. 6.23(a) and 6.23(d). If there is no MFO on the ACSs, the FOD-PCS module and PS module will be enabled as presented in Fig. 6.23(b) and 6.23(e). When the Rx reaches p_k and FOD-ACS module is not triggered, the EVD will be triggered as per Fig. 6.23(c) and 6.23(f).

In the comparison between Fig. 6.23(a) and 6.23(d), the input impedance Z_d changed by around 20% which proves the effectiveness of the FOD-ACS module. It should be mentioned that V_{EV} has harmonics at f_{FOD} because V_{FOD} is shared by L_{BCS7} and L_{UCS4} according to the DRC in Fig. 6.6(b). This does not affect the operation of EVD module because EVD module is enabled after the operation of FOD-ACS module.

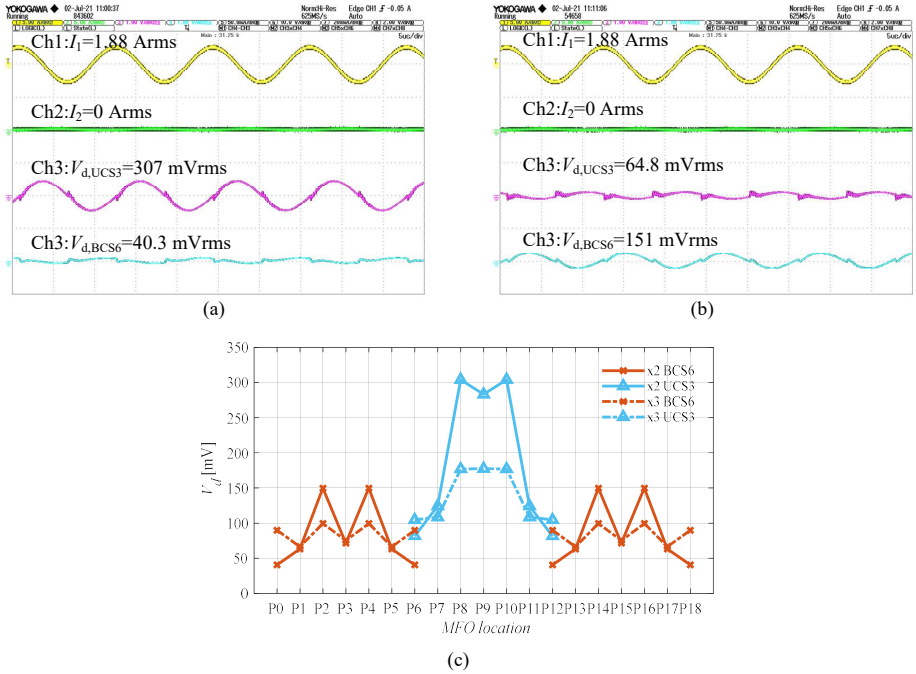

Figure 6.18: Experimental results of FOD using PCS. Waveforms of V_d with the MFO (a) at (x2, P8) and (b) at (x2, P2), and (c) full-range performance when the MFO moves along trajectory x2 and x3.

In the comparison between Fig. 6.23(b) and 6.23(e), $V_{d,UCS3}$ changes from 186 mVrms to 1103 mVrms due to the MFO placed on UCS-3. The change in $V_{d,BCS6}$ is insignificant although the MFO is close to BCS-6. In Fig. 6.23(c) and 6.23(f) both Rx and Tx are energized so the magnetic field is stronger than that in Fig. 6.23(b) and 6.23(e). Correspondingly, $V_{d,UCS3}$ and $V_{d,BCS6}$ increase slightly. To avoid the fault detection of the FOD-PCS module, the predefined threshold value should be selected based on the measurements in Fig. 6.23(c) and 6.23(e). Taking UCS-3 as an example, $V_{d,UCS3}$ is 381 mVrms in Fig. 6.23(c) and 1103 mVrms in Fig. 6.23(e). Thus, the threshold value should be between these two measured values.

As the Rx moves from p_{k-1} to p_k, the mutual coupling between the EVSC and ACSs increases as shown in Fig. 6.9. Therefore, V_{EV} increases from 405 mVrms in Fig. 6.23(b) to 752 mVrms in Fig. 6.23(c), which proves that the main field does not affect the effectiveness of the EVD module. Besides, it is also proved by Fig. 6.23(f) that the presence of the MFO on PCSs has no influence on the operation of the EVD module.

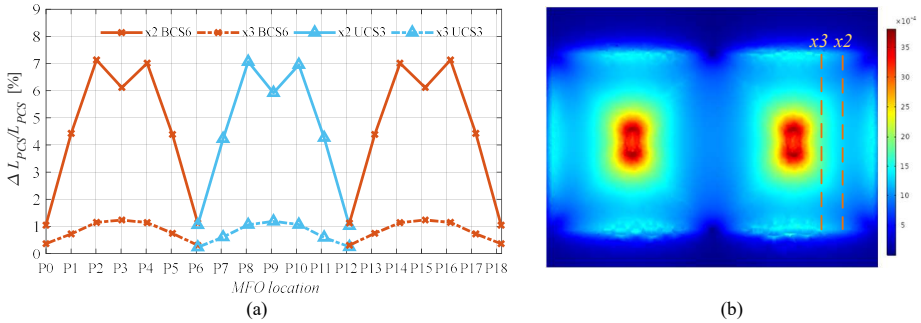

Figure 6.19: Finite element model results, (a) the normalized self-inductance reduction of PCSs led by MFOs, (b) the magnetic field distribution (unit T).

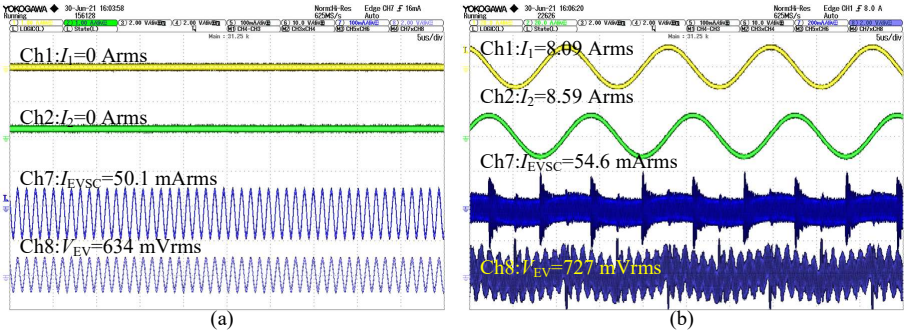

Figure 6.20: Measured waveform of V_{EV} , I_{EVSC} and I_d when the Tx and Rx are aligned, with (a) PS off and (b) PS on.

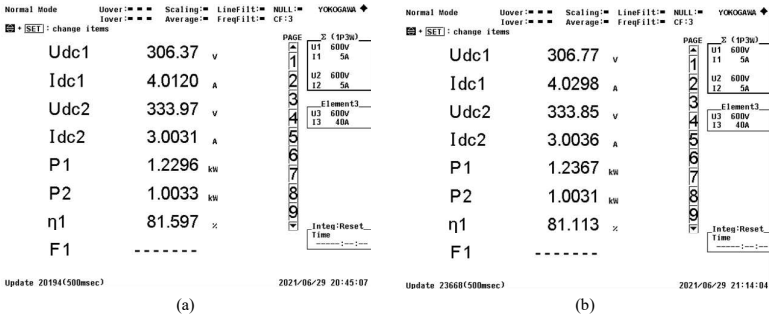

Figure 6.21: System efficiency at 1 kW output power (a) with no PCB coils and (b) with PCB coils connected to the DRC.

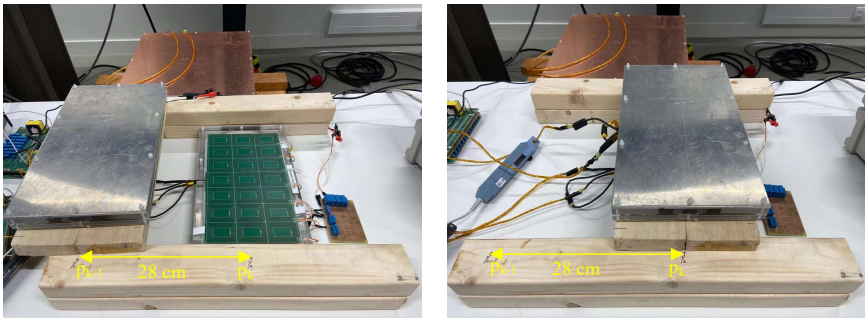

(a) (b)

Figure 6.22: Experiments considering the real practical scenarios. The Rx is (a) aligned with Tx_{k-1} at p_{k-1} and (b) aligned with Tx_k at p_k. The distance between p_{k-1} and p_k is 28 cm.

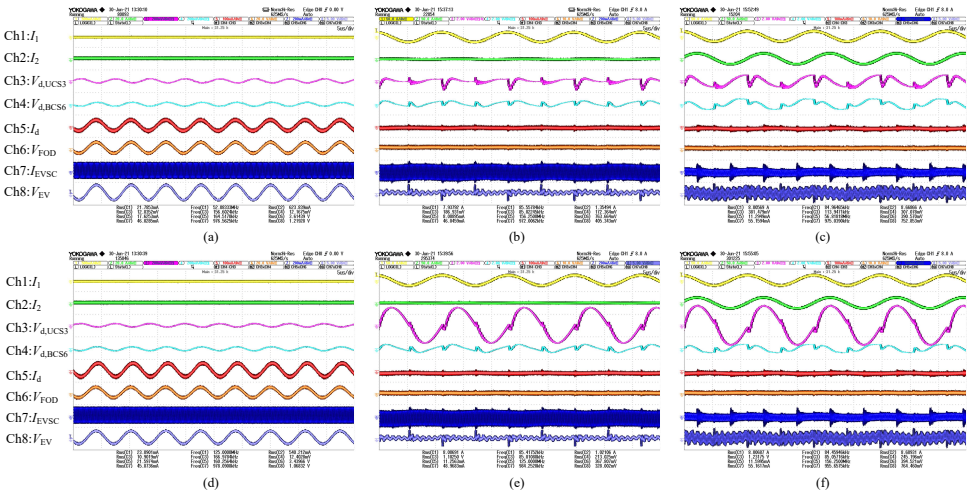

Figure 6.23: System performances at different operating conditions. (a) the FOD-ACS operates with no MFOs and the Rx at p_{k-1}, (b) the FOD-PCS operates with the PS on, no MFOs and the Rx at p_{k-1}. (c) the EVD is triggered with the PS on, no MFOs and the Rx at p_k. (d) the FOD-ACS is triggered with a MFO on UCS-4 and the Rx at p_{k-1}, (e) the FOD-PCS is triggered with the PS on, a MFO on UCS-3 and the Rx at p_{k-1}. (f) the EVD triggered with the PS on, a MFO on UCS-3 and the Rx at p_k.

6.5 Conclusions

This chapter proposes an integrated detection method that applies the same auxiliary detection coil sets to realize both EVD and FOD for DIPT systems. The proposed detection system mainly consists of auxiliary detection coil sets and a DRC. Different from the existing topology of auxiliary coil sets, the proposed detection coil sets apply both PCSs and ACSs to eliminate the blind zone and gain a high sensitivity to the intrusion of MFOs. Besides, a DRC topology is proposed to further amplify the influence of MFOs and EVs on auxiliary detection coil sets to make EVD and FOD more effective and reliable. Aiming at DIPT applications, the detection procedures are introduced and the operating conditions of the detection modules are concluded. The proposed design mainly includes the FOD-ACS module, the FOD-PCS module, and the EVD module. To validate the proposed detection method, PCB coils are designed and integrated into an IPT system. According to the operating conditions of the detection modules, experiments are conducted for each detection module as well as the entire system considering the practical DIPT application scenarios. Based on the experimental results, the proposed design is able to realize reliable EVD and FOD functions with high sensitivity and no blind zone.

7

Conclusions and Future Work

This thesis studied four research questions that should be addressed before dynamic IPT becomes mature enough for commercial use. The study first presents the steady-state circuit models of IPT systems to explain the general operating principles and features. Then, the thesis answers the research questions in four chapters, focusing on magnetic coupler design, prediction and control of transient behaviors, reduction of power fluctuation, and detection of EVs and FOs.

Conclusions

1. *How to optimize the IPT charging pad?*

The key performance indicators of an IPT system include power transfer capability, power density, power efficiency, and misalignment tolerance. Due to conflicts among these performance indicators, it is indispensable to formulate the design of IPT charging pads as a multi-objective optimization (MOO) problem. By using finite element (FE) models, the magnetic field property of a coupler can be computed. However, calculating the aligned and misaligned power losses at the rated power requires not only the magnetic field property but also the compensation strategy. The compensation strategy determines the load match method which is used to calculate the optimal load condition and the rated winding currents. Therefore, compensation selection should be considered at the start of the MOO problem. With the magnetic field distribution known, the power losses in the AC link can be calculated through the existing analytical method.

In Chapter 3, the double-sided LCC (DLCC) compensation and the series-series (SS) compensation are compared thoroughly. The SS compensation is found to have a higher power efficiency and less voltage/current stresses on the receiver (Rx) side, so the SS compensation is selected in the target design. By sweeping the design search space of magnetic couplers, the performances of IPT systems can be computed and Pareto fronts are obtained. Finally, a 20 kW prototype is built and the accuracy of the proposed power

losses method is verified. In conclusion, the study shows that analytically calculating the AC link power efficiency is possible when the magnetic field is accurately computed at the rated condition. More importantly, the fact that the DC-DC power efficiency reaches 97.2% at the rated operation point proves that the MOO design is vital to making full use of IPT technology.

2. *How to model the dynamic characteristics of DIPT systems?*

IPT systems require capacitive/inductive components to form resonant circuits on both sides to improve the power transfer capability and power efficiency, while the compensation components also make the resonant stage of a high order. As a result, the analytical dynamic models of IPT systems are complex and mostly impossible to solve in the time domain. On one hand, the high-order dynamic model cannot provide insights into system design to improve dynamic behavior. On the other hand, the high complexity of the conventional dynamic models prevents the application of control strategies that require an accurate dynamic model to regulate the output, for example, model predictive control (MPC).

Chapter 4 proposes a new reduced-order dynamic modeling method that describes the transient behavior of a resonant stage from the energy point of view. The order of the resultant dynamic model is one-fourth that of conventional ones for SS compensated IPT systems. Besides, a MPC controller is designed based on the proposed dynamic model. The accuracy of the proposed dynamic model and the function of the designed MPC controller are verified experimentally. It can be concluded that simplifying the dynamic model makes it possible to explain how circuit parameters influence the transient behavior, facilitate the application of advanced control strategies, and reduce the computation cost of prediction in IPT systems.

3. *How to reduce the pick-up power fluctuation of DIPT systems?*

The most obvious difference between static and dynamic IPT is the change in magnetic coupling. In DIPT applications, the magnetic coupling fluctuates from the maximum to a usable level as EVs move, so one of the main challenges of DIPT is to stabilize the pick-up power, especially for DIPT systems using segmented transmitter (Tx) coils where magnetic coupling changes more frequently. The conventional methods are either to overlap Tx coils or to add extra sets of the receiver (Rx) sides, which are expensive in building costs.

Chapter 5 presents the design of a segmented DIPT system using a multiphase Tx side. The Rx coil consists of two sub-windings connected in series with a relatively large spatial offset in the EV moving direction. One advantage of the proposed design is that the Tx coils are deployed loosely so the building cost can be reduced. The other advantage is that the pick-up power is seamless with a small ripple. The pick-up power demonstrates a 24.9% ripple by experiments. Chapter 5 also presents a method to optimize the spatial offset on the Tx and Rx sides, so one can compromise between reducing the output ripple and minimizing the building cost according to the preference. To draw a conclusion, the proposed design of the DIPT system can achieve a low pick-up power fluctuation and less material cost on the Tx side compared with conventional segmented DIPT systems.

4. *What is the most suited solution for the detection of EVs and foreign objects in DIPT systems?*

To minimize the transmitter (Tx) side power losses and magnetic field radiation, the detection of EVs and foreign objects (FOs) should be implemented in DIPT systems. Considering the integration of the detection equipment into the charging pads, PCB coils become the most suitable candidate to sense the magnetic field for detection purposes. However, the detection of EVs and FOs are mostly discussed separately in the literature. There is a need to achieve these two detection functions within one set of PCB coils.

Chapter 6 presents the design of detection equipment consisting of PCB coils installed onto charging pads and the detection resonant circuit (DRC) connected to Tx side PCB coils. By measuring the voltage/current variations in the DRC, the presence of EVs and FOs can be identified in the same set of PCB coils. The effectiveness of the proposed detection method is experimentally verified in a 1 kW IPT system. It can be concluded that the detection of EVs and FOs can both be realized by measuring the variation of the magnetic field caused by their intrusion, and PCB coils demonstrate good performances in measuring the change of magnetic field together with DRC to amplify the detection signals.

Future work

This thesis studies various technical problems related to IPT applications and presents solutions for each of these problems. However, these solutions are independently realized in three different IPT prototypes where the coil topology and compensation strategy are different. Some of the proposed solutions are only applicable to a specific coil or compensation topology. The dynamic modeling method proposed in Chapter 4 can only accurately model IPT systems using the SS compensation. The detection method proposed in Chapter 6 can only work on IPT systems using DD coils on both sides. It would significantly enhance the contribution of this thesis if the proposed solutions are not limited to a specific kind of IPT system and can be realized in one IPT prototype.

Another valuable research direction is to realize the proposed MOO method using open-source FE tools. In this thesis, the MOO code uses COMSOL to compute the magnetic field and uses MATLAB to wrap the optimization loop. There are open-source candidates that can realize the same functions. In the research area of IPT, there is no open-source MOO tool available in the literature, which can handle different power levels, coil topology, and compensation strategies.

Lastly, more effort should be paid to fully stabilize the output of the DIPT system in Chapter 5. By using the proposed design, the ripple of pick-up power is 24.9% which can be further stabilized by a back-end DC-DC converter. Due to the relatively high speed of EVs in real applications, it is important to investigate a suitable design of a controller for the back-end DC-DC converter that can rapidly respond to the change of its input.

Bibliography

References

[1] G. Strbac, D. Papadaskalopoulos, N. Chrysanthopoulos, A. Estanqueiro, H. Algarvio, F. Lopes, L. de Vries, G. Morales-España, J. Sijm, R. Hernandez-Serna, J. Kiviluoma, and N. Helisto, "Decarbonization of Electricity Systems in Europe: Market Design Challenges," *IEEE Power and Energy Magazine*, vol. 19, no. 1, pp. 53–63, Jan. 2021, conference Name: IEEE Power and Energy Magazine.

[2] P. Jochem, S. Babrowski, and W. Fichtner, "Assessing CO2 emissions of electric vehicles in Germany in 2030," *Transportation Research Part A: Policy and Practice*, vol. 78, pp. 68–83, Aug. 2015. [Online]. Available: https://www.sciencedirect.com/science/article/pii/S0965856415001354

[3] C. Xue, H. Zhou, Q. Wu, X. Wu, and X. Xu, "Impact of Incentive Policies and Other Socio-Economic Factors on Electric Vehicle Market Share: A Panel Data Analysis from the 20 Countries," *Sustainability*, vol. 13, no. 5, p. 2928, Jan. 2021, number: 5 Publisher: Multidisciplinary Digital Publishing Institute. [Online]. Available: https://www.mdpi.com/2071-1050/13/5/2928

[4] "The Electric Driving Monitor 2021 | ANWB." [Online]. Available: https://www.anwb.nl/belangenbehartiging/duurzaam/elektrisch-rijden-monitor-2021

[5] C. Yang, "Running battery electric vehicles with extended range: Coupling cost and energy analysis," *Applied Energy*, vol. 306, p. 118116, Jan. 2022. [Online]. Available: https://www.sciencedirect.com/science/article/pii/S0306261921013957

[6] "inistry of Industry and Information Technology of China. Energy-saving and New Energy Vehicle Technology Roadmap (2016)." [Online]. Available: https://www.sohu.com/a/www.sohu.com/a/117.879.979_386926

[7] J. H. Kim, B. Lee, J. Lee, S. Lee, C. Park, S. Jung, S. Lee, K. Yi, and J. Baek, "Development of 1-MW Inductive Power Transfer System for a High-Speed Train," *IEEE Transactions on Industrial Electronics*, vol. 62, no. 10, pp. 6242–6250, Oct. 2015.

[8] R. Bosshard, "Multi-Objective Optimization of Inductive Power Transfer Systems for EV Charging," Ph.D. dissertation, ETH Zurich, 2015, artwork Size: 233 p. Medium: application/pdf Pages: 233 p. [Online]. Available: http://hdl.handle.net/20.500.11850/117204

[9] S. Li, S. Lu, and C. C. Mi, "Revolution of Electric Vehicle Charging Technologies Accelerated by Wide Bandgap Devices," *Proceedings of the IEEE*, pp. 1–19, 2021, conference Name: Proceedings of the IEEE.

[10] S.-H. Lee, B.-S. Lee, and J.-H. Lee, "A New Design Methodology for a 300-kW, Low Flux Density, Large Air Gap, Online Wireless Power Transfer System," *IEEE Transactions on Industry Applications*, vol. 52, no. 5, pp. 4234–4242, Sep. 2016, conference Name: IEEE Transactions on Industry Applications.

[11] J. Shin, S. Shin, Y. Kim, S. Ahn, S. Lee, G. Jung, S. Jeon, and D. Cho, "Design and Implementation of Shaped Magnetic-Resonance-Based Wireless Power Transfer System for Roadway-Powered Moving Electric Vehicles," *IEEE Transactions on Industrial Electronics*, vol. 61, no. 3, pp. 1179–1192, Mar. 2014.

[12] R. Bosshard and J. W. Kolar, "Multi-Objective Optimization of 50 kW/85 kHz IPT System for Public Transport," *IEEE Journal of Emerging and Selected Topics in Power Electronics*, vol. 4, no. 4, pp. 1370–1382, Dec. 2016.

[13] ——, "All-SiC 9.5 kW/dm3 On-Board Power Electronics for 50 kW/85 kHz Automotive IPT System," *IEEE Journal of Emerging and Selected Topics in Power Electronics*, vol. 5, no. 1, pp. 419–431, Mar. 2017, conference Name: IEEE Journal of Emerging and Selected Topics in Power Electronics.

[14] J. Pries, V. P. N. Galigekere, O. C. Onar, and G.-J. Su, "A 50-kW Three-Phase Wireless Power Transfer System Using Bipolar Windings and Series Resonant Networks for Rotating Magnetic Fields," *IEEE Transactions on Power Electronics*, vol. 35, no. 5, pp. 4500–4517, May 2020, conference Name: IEEE Transactions on Power Electronics.

[15] A. U. Ibrahim, W. Zhong, and M. D. Xu, "A 50-kW Three-Channel Wireless Power Transfer System With Low Stray Magnetic Field," *IEEE Transactions on Power Electronics*, vol. 36, no. 9, pp. 9941–9954, Sep. 2021, conference Name: IEEE Transactions on Power Electronics.

[16] H. H. Wu and M. P. Masquelier, "An overview of a 50kW inductive charging system for electric buses," in *2015 IEEE Transportation Electrification Conference and Expo (ITEC)*, Jun. 2015, pp. 1–4.

[17] N. Shinohara, "Wireless power transmission progress for electric vehicle in Japan," in *2013 IEEE Radio and Wireless Symposium*, Jan. 2013, pp. 109–111, iSSN: 2164-2974.

[18] C. C. Mi, G. Buja, S. Y. Choi, and C. T. Rim, "Modern Advances in Wireless Power Transfer Systems for Roadway Powered Electric Vehicles," *IEEE Transactions on Industrial Electronics*, vol. 63, no. 10, pp. 6533–6545, Oct. 2016.

[19] A. Foote and O. C. Onar, "A review of high-power wireless power transfer," in *2017 IEEE Transportation Electrification Conference and Expo (ITEC)*, Jun. 2017, pp. 234–240.

[20] J. Huh, S. W. Lee, W. Y. Lee, G. H. Cho, and C. T. Rim, "Narrow-Width Inductive Power Transfer System for Online Electrical Vehicles," *IEEE Transactions on Power Electronics*, vol. 26, no. 12, pp. 3666–3679, Dec. 2011.

[21] M. Bojarski, E. Asa, K. Colak, and D. Czarkowski, "A 25 kW industrial prototype wireless electric vehicle charger," in *2016 IEEE Applied Power Electronics Conference and Exposition (APEC)*, Mar. 2016, pp. 1756–1761.

[22] S. Y. Choi, S. Y. Jeong, B. W. Gu, G. C. Lim, and C. T. Rim, "Ultraslim S-Type Power Supply Rails for Roadway-Powered Electric Vehicles," *IEEE Transactions on Power Electronics*, vol. 30, no. 11, pp. 6456–6468, Nov. 2015.

[23] B. Goeldi, J. Tritschler, and S. Reichert, "Measurement Results of a 22 kW Bidirectional Inductive Charger," in *Proceedings of PCIM Europe 2015; International Exhibition and Conference for Power Electronics, Intelligent Motion, Renewable Energy and Energy Management*, May 2015, pp. 1–8.

[24] M. Mohammad, O. C. Onar, G.-J. Su, J. Pries, V. P. Galigekere, S. Anwar, E. Asa, J. Wilkins, R. Wiles, C. P. White, and L. E. Seiber, "Bidirectional LCC-LCC Compensated 20 kW Wireless Power Transfer System for Medium-Duty Vehicle Charging," *IEEE Transactions on Transportation Electrification*, pp. 1–1, 2021, conference Name: IEEE Transactions on Transportation Electrification.

[25] S. Y. Choi, B. W. Gu, S. Y. Jeong, and C. T. Rim, "Advances in Wireless Power Transfer Systems for Roadway-Powered Electric Vehicles," *IEEE Journal of Emerging and Selected Topics in Power Electronics*, vol. 3, no. 1, pp. 18–36, Mar. 2015.

[26] R. Bosshard, J. Mühlethaler, J. W. Kolar, and I. Stevanović, "The --Pareto front of inductive power transfer coils," in *IECON 2012 - 38th Annual Conference on IEEE Industrial Electronics Society*, Oct. 2012, pp. 4270–4277, iSSN: 1553-572X.

[27] S. Li and C. C. Mi, "Wireless Power Transfer for Electric Vehicle Applications," *IEEE Journal of Emerging and Selected Topics in Power Electronics*, vol. 3, no. 1, pp. 4–17, Mar. 2015.

[28] M. Budhia, J. T. Boys, G. A. Covic, and C. Huang, "Development of a Single-Sided Flux Magnetic Coupler for Electric Vehicle IPT Charging Systems," *IEEE Transactions on Industrial Electronics*, vol. 60, no. 1, pp. 318–328, Jan. 2013.

[29] M. Budhia, G. A. Covic, J. T. Boys, and C. Huang, "Development and evaluation of single sided flux couplers for contactless electric vehicle charging," in *2011 IEEE Energy Conversion Congress and Exposition*, Sep. 2011, pp. 614–621.

[30] M. Budhia, G. A. Covic, and J. T. Boys, "Design and Optimization of Circular Magnetic Structures for Lumped Inductive Power Transfer Systems," *IEEE Transactions on Power Electronics*, vol. 26, no. 11, pp. 3096–3108, Nov. 2011.

[31] A. Zaheer, D. Kacprzak, and G. A. Covic, "A bipolar receiver pad in a lumped IPT system for electric vehicle charging applications," in *2012 IEEE Energy Conversion Congress and Exposition (ECCE)*, Sep. 2012, pp. 283–290.

[32] S. Kim, G. A. Covic, and J. T. Boys, "Tripolar Pad for Inductive Power Transfer Systems for EV Charging," *IEEE Transactions on Power Electronics*, vol. 32, no. 7, pp. 5045–5057, Jul. 2017.

[33] H. Matsumoto, Y. Neba, H. Iura, D. Tsutsumi, K. Ishizaka, and R. Itoh, "Trifoliate Three-Phase Contactless Power Transformer in Case of Winding-Alignment," *IEEE Transactions on Industrial Electronics*, vol. 61, no. 1, pp. 53–62, Jan. 2014.

[34] A. Tejeda, S. Kim, F. Y. Lin, G. A. Covic, and J. T. Boys, "A Hybrid Solenoid Coupler for EV Wireless Charging Applications," *IEEE Transactions on Power Electronics*, pp. 1–1, 2018.

[35] R. Bosshard, J. W. Kolar, J. Mühlethaler, I. Stevanović, B. Wunsch, and F. Canales, "Modeling and$\eta $-$\alpha $-Pareto Optimization of Inductive Power Transfer Coils for Electric Vehicles," *IEEE Journal of Emerging and Selected Topics in Power Electronics*, vol. 3, no. 1, pp. 50–64, Mar. 2015.

[36] S. Bandyopadhyay, P. Venugopal, J. Dong, and P. Bauer, "Comparison of Magnetic Couplers for IPT based EV Charging using Multi-Objective Optimization," *IEEE Transactions on Vehicular Technology*, pp. 1–1, 2019.

[37] W. Shi, F. Grazian, S. Bandyopadhyay, J. Dong, T. B. Soeiro, and P. Bauer, "Analysis of Dynamic Charging Performances of Optimized Inductive Power Transfer Couplers," in *2021 IEEE 19th International Power Electronics and Motion Control Conference (PEMC)*, Apr. 2021, pp. 751–756, iSSN: 2473-0165.

[38] M. Lu and K. D. T. Ngo, "A Fast Method to Optimize Efficiency and Stray Magnetic Field for Inductive-Power-Transfer Coils Using Lumped-Loops Model," *IEEE Transactions on Power Electronics*, vol. 33, no. 4, pp. 3065–3075, Apr. 2018.

[39] A. K. Swain, M. J. Neath, U. K. Madawala, and D. J. Thrimawithana, "A Dynamic Multivariable State-Space Model for Bidirectional Inductive Power Transfer Systems," *IEEE Transactions on Power Electronics*, vol. 27, no. 11, pp. 4772–4780, Nov. 2012.

[40] S. R. Sanders, J. M. Noworolski, X. Z. Liu, and G. C. Verghese, "Generalized averaging method for power conversion circuits," in *21st Annual IEEE Conference on Power Electronics Specialists*, 1990, pp. 333–340.

[41] H. Hao, G. A. Covic, and J. T. Boys, "An Approximate Dynamic Model of LCL-T-Based Inductive Power Transfer Power Supplies," *IEEE Transactions on Power Electronics*, vol. 29, no. 10, pp. 5554–5567, Oct. 2014.

[42] C. T. Rim and G. H. Cho, "Phasor transformation and its application to the DC/AC analyses of frequency phase-controlled series resonant converters (SRC)," *IEEE Transactions on Power Electronics*, vol. 5, no. 2, pp. 201–211, Apr. 1990.

[43] S. Lee, B. Choi, and C. T. Rim, "Dynamics Characterization of the Inductive Power Transfer System for Online Electric Vehicles by Laplace Phasor Transform," *IEEE Transactions on Power Electronics*, vol. 28, no. 12, pp. 5902–5909, Dec. 2013.

[44] H. Li, J. Fang, and Y. Tang, "Dynamic Phasor-Based Reduced-Order Models of Wireless Power Transfer Systems," *IEEE Transactions on Power Electronics*, vol. 34, no. 11, pp. 11 361–11 370, Nov. 2019.

[45] Z. U. Zahid, Z. M. Dalala, C. Zheng, R. Chen, W. E. Faraci, J. J. Lai, G. Lisi, and D. Anderson, "Modeling and Control of Series–Series Compensated Inductive Power Transfer System," *IEEE Journal of Emerging and Selected Topics in Power Electronics*, vol. 3, no. 1, pp. 111–123, Mar. 2015.

[46] H. A. Haus and W. Huang, "Coupled-mode theory," *Proceedings of the IEEE*, vol. 79, no. 10, pp. 1505–1518, Oct. 1991.

[47] H. Li, K. Wang, L. Huang, W. Chen, and X. Yang, "Dynamic Modeling Based on Coupled Modes for Wireless Power Transfer Systems," *IEEE Transactions on Power Electronics*, vol. 30, no. 11, pp. 6245–6253, Nov. 2015.

[48] J. Tang, S. Dong, C. Cui, and Q. Zhang, "Sampled-Data Modeling for Wireless Power Transfer Systems," *IEEE Transactions on Power Electronics*, vol. 35, no. 3, pp. 3173–3182, Mar. 2020.

[49] D. Patil, M. K. McDonough, J. M. Miller, B. Fahimi, and P. T. Balsara, "Wireless Power Transfer for Vehicular Applications: Overview and Challenges," *IEEE Transactions on Transportation Electrification*, vol. 4, no. 1, pp. 3–37, Mar. 2018.

[50] F. Grazian, W. Shi, J. Dong, P. van Duijsen, T. B. Soeiro, and P. Bauer, "Survey on Standards and Regulations for Wireless Charging of Electric Vehicles," in *2019 AEIT International Conference of Electrical and Electronic Technologies for Automotive (AEIT AUTOMOTIVE)*, Jul. 2019, pp. 1–5.

[51] A. N. Azad, A. Echols, V. A. Kulyukin, R. Zane, and Z. Pantic, "Analysis, Optimization, and Demonstration of a Vehicular Detection System Intended for Dynamic Wireless Charging Applications," *IEEE Transactions on Transportation Electrification*, vol. 5, no. 1, pp. 147–161, Mar. 2019, conference Name: IEEE Transactions on Transportation Electrification.

[52] S. Y. Jeong, H. G. Kwak, G. C. Jang, S. Y. Choi, and C. T. Rim, "Dual-Purpose Nonoverlapping Coil Sets as Metal Object and Vehicle Position Detections for Wireless Stationary EV Chargers," *IEEE Transactions on Power Electronics*, vol. 33, no. 9, pp. 7387–7397, Sep. 2018.

[53] Q. Deng, J. Liu, D. Czarkowski, M. Bojarski, J. Chen, W. Hu, and H. Zhou, "Edge Position Detection of On-line Charged Vehicles With Segmental Wireless Power Supply," *IEEE Transactions on Vehicular Technology*, vol. 66, no. 5, pp. 3610–3621, May 2017, conference Name: IEEE Transactions on Vehicular Technology.

[54] A. Kamineni, M. J. Neath, A. Zaheer, G. A. Covic, and J. T. Boys, "Interoperable EV Detection for Dynamic Wireless Charging With Existing Hardware and Free Resonance," *IEEE Transactions on Transportation Electrification*, vol. 3, no. 2, pp. 370–379, Jun. 2017, conference Name: IEEE Transactions on Transportation Electrification.

[55] K. Lee, Z. Pantic, and S. M. Lukic, "Reflexive Field Containment in Dynamic Inductive Power Transfer Systems," *IEEE Transactions on Power Electronics*, vol. 29, no. 9, pp. 4592–4602, Sep. 2014.

[56] R. M. Tyburski, "A review of road sensor technology for monitoring vehicle traffic," *ITE (Institute of Transportation Engineers) Journal; (USA)*, vol. 59:8, Aug. 1988. [Online]. Available: https://www.osti.gov/biblio/5578046

[57] Xiaoying Jin and C. H. Davis, "Vector-guided vehicle detection from high-resolution satellite imagery," in *IGARSS 2004. 2004 IEEE International Geoscience and Remote Sensing Symposium*, vol. 2, Sep. 2004, pp. 1095–1098.

[58] Q. Wang, J. Zheng, B. Xu, and Y. Huang, "Analysis and experiments of vehicle detection with magnetic sensors in urban environments," in *2015 IEEE International Conference on Cyber Technology in Automation, Control, and Intelligent Systems (CYBER)*, Jun. 2015, pp. 71–75.

[59] M. Rivas-López, C. A. Gomez-Sanchez, J. Rivera-Castillo, O. Sergiyenko, W. Flores-Fuentes, J. C. Rodríguez-Quiñonez, and P. Mayorga-Ortiz, "Vehicle detection using an infrared light emitter and a photodiode as visualization system," in *2015 IEEE 24th International Symposium on Industrial Electronics (ISIE)*, Jun. 2015, pp. 972–975, iSSN: 2163-5145.

[60] G. R. Nagendra, L. Chen, G. A. Covic, and J. T. Boys, "Detection of EVs on IPT Highways," *IEEE Journal of Emerging and Selected Topics in Power Electronics*, vol. 2, no. 3, pp. 584–597, Sep. 2014.

[61] M. A. G. Clark, "Induction loop vehicle detector," US Patent US4 568 937A, Feb., 1986. [Online]. Available: https://patents.google.com/patent/US4568937A/en

[62] S. Fukuda, H. Nakano, Y. Murayama, T. Murakami, O. Kozakai, and K. Fujimaki, "A novel metal detector using the quality factor of the secondary coil for wireless power transfer systems," in *2012 IEEE MTT-S International Microwave Workshop Series on Innovative Wireless Power Transmission: Technologies, Systems, and Applications*, May 2012, pp. 241–244.

[63] H. Kikuchi, "Metal-loop effects in wireless power transfer systems analyzed by simulation and theory," in *2013 IEEE Electrical Design of Advanced Packaging Systems Symposium (EDAPS)*, Dec. 2013, pp. 201–204.

[64] M. Moghaddami and A. I. Sarwat, "A Sensorless Conductive Foreign Object Detection for Inductive Electric Vehicle Charging Systems Based on Resonance Frequency Deviation," in *2018 IEEE Industry Applications Society Annual Meeting (IAS)*, Sep. 2018, pp. 1–6.

[65] N. Kuyvenhoven, C. Dean, J. Melton, J. Schwannecke, and A. E. Umenei, "Development of a foreign object detection and analysis method for wireless power systems," in *2011 IEEE Symposium on Product Compliance Engineering Proceedings*, Oct. 2011, pp. 1–6.

[66] V. X. Thai, G. C. Jang, S. Y. Jeong, J. H. Park, Y.-S. Kim, and C. T. Rim, "Symmetric Sensing Coil Design for the Blind-zone Free Metal Object Detection of a Stationary Wireless Electric Vehicles Charger," *IEEE Transactions on Power Electronics*, pp. 1–1, 2019.

[67] L. Xiang, Z. Zhu, J. Tian, and Y. Tian, "Foreign Object Detection in a Wireless Power Transfer System Using Symmetrical Coil Sets," *IEEE Access*, vol. 7, pp. 44 622–44 631, 2019.

[68] S. Verghese, M. P. Kesler, K. L. Hall, and H. T. Lou, "Foreign object detection in wireless energy transfer systems," US Patent US9 442 172B2, Sep., 2016. [Online]. Available: https://patents.google.com/patent/US9442172B2/en

[69] S. Y. Jeong, V. X. Thai, J. H. Park, and C. T. Rim, "Self-Inductance-Based Metal Object Detection With Mistuned Resonant Circuits and Nullifying Induced Voltage for Wireless EV Chargers," *IEEE Transactions on Power Electronics*, vol. 34, no. 1, pp. 748–758, Jan. 2019.

[70] V. X. Thai, S. Y. Choi, B. H. Choi, J. H. Kim, and C. T. Rim, "Coreless power supply rails compatible with both stationary and dynamic charging of electric vehicles," in *2015 IEEE 2nd International Future Energy Electronics Conference (IFEEC)*, Nov. 2015, pp. 1–5.

[71] W. Shi, J. Dong, T. B. Soeiro, C. Riekerk, F. Grazian, G. Yu, and P. Bauer, "Design of a Highly Efficient 20 kW Inductive Power Transfer System with Improved Misalignment Performance," *IEEE Transactions on Transportation Electrification*, pp. 1–1, 2021, conference Name: IEEE Transactions on Transportation Electrification.

[72] S. Song, Q. Zhang, Z. He, H. Li, and X. Zhang, "Uniform Power Dynamic Wireless Charging System With I-Type Power Supply Rail and DQ-Phase-Receiver Employing Receiver-Side Control," *IEEE Transactions on Power Electronics*, vol. 35, no. 10, pp. 11 205–11 212, Oct. 2020.

[73] Z. Wang, S. Cui, S. Han, K. Song, C. Zhu, M. I. Matveevich, and O. S. Yurievich, "A Novel Magnetic Coupling Mechanism for Dynamic Wireless Charging System for Electric Vehicles," *IEEE Transactions on Vehicular Technology*, vol. 67, no. 1, pp. 124–133, Jan. 2018, conference Name: IEEE Transactions on Vehicular Technology.

[74] C. Park, S. Lee, S. Y. Jeong, G. Cho, and C. T. Rim, "Uniform Power I-Type Inductive Power Transfer System With DQ-Power Supply Rails for On-Line Electric Vehicles," *IEEE Transactions on Power Electronics*, vol. 30, no. 11, pp. 6446–6455, Nov. 2015.

[75] B. Song, S. Cui, Y. Li, and C. Zhu, "A Narrow-Rail Three-Phase Magnetic Coupler With Uniform Output Power for EV Dynamic Wireless Charging," *IEEE Transactions on Industrial Electronics*, vol. 68, no. 8, pp. 6456–6469, Aug. 2021, conference Name: IEEE Transactions on Industrial Electronics.

[76] V.-B. Vu, M. Dahidah, V. Pickert, and V.-T. Phan, "A High-Power Multiphase Wireless Dynamic Charging System With Low Output Power Pulsation for Electric Vehicles," *IEEE Journal of Emerging and Selected Topics in Power Electronics*, vol. 8, no. 4, pp. 3592–3608, Dec. 2020, conference Name: IEEE Journal of Emerging and Selected Topics in Power Electronics.

[77] J. Deng, B. Pang, W. Shi, and Z. Wang, "A new integration method with minimized extra coupling effects using inductor and capacitor series-parallel compensation for wireless EV charger," *Applied Energy*, vol. 207, pp. 405–416, Dec. 2017. [Online]. Available: http://www.sciencedirect.com/science/article/pii/S0306261917305925

[78] F. Grazian, W. Shi, T. B. Soeiro, J. Dong, P. van Duijsen, and P. Bauer, "Compensation Network for a 7.7 kW Wireless Charging System that Uses Standardized Coils," in *2020 IEEE International Symposium on Circuits and Systems (ISCAS)*, Oct. 2020, pp. 1–5, iSSN: 2158-1525.

[79] W. Zhong and S. Y. R. Hui, "Maximum Energy Efficiency Operation of Series-Series Resonant Wireless Power Transfer Systems Using On-Off Keying Modulation," *IEEE Transactions on Power Electronics*, vol. 33, no. 4, pp. 3595–3603, Apr. 2018.

[80] W. Zhang, S. Wong, C. K. Tse, and Q. Chen, "Design for Efficiency Optimization and Voltage Controllability of Series–Series Compensated Inductive Power Transfer Systems," *IEEE Transactions on Power Electronics*, vol. 29, no. 1, pp. 191–200, Jan. 2014.

[81] T. Diekhans and R. W. D. Doncker, "A Dual-Side Controlled Inductive Power Transfer System Optimized for Large Coupling Factor Variations and Partial Load," *IEEE Transactions on Power Electronics*, vol. 30, no. 11, pp. 6320–6328, Nov. 2015.

[82] S. Li, W. Li, J. Deng, T. D. Nguyen, and C. C. Mi, "A Double-Sided LCC Compensation Network and Its Tuning Method for Wireless Power Transfer," *IEEE Transactions on Vehicular Technology*, vol. 64, no. 6, pp. 2261–2273, Jun. 2015.

[83] Y. Chen, H. Zhang, C.-S. Shin, C.-H. Jo, S.-J. Park, and D.-H. Kim, "An Efficiency Optimization-Based Asymmetric Tuning Method of Double-Sided LCC Compensated WPT System for Electric Vehicles," *IEEE Transactions on Power Electronics*, vol. 35, no. 11, pp. 11 475–11 487, Nov. 2020, conference Name: IEEE Transactions on Power Electronics.

[84] K. Takeda and T. Koseki, "Analytical Investigation on Asymmetric LCC Compensation Circuit for Trade-off between High Efficiency and Power," in *2018 International Power Electronics Conference (IPEC-Niigata 2018 -ECCE Asia)*, May 2018, pp. 2309–2316.

[85] V.-T. Nguyen, V.-B. Vu, G. Gohil, and B. Fahimi, "Efficiency optimization of double-sided LCC topology for inductive power transfer systems," in *2021 IEEE Applied Power Electronics Conference and Exposition (APEC)*, Jun. 2021, pp. 1610–1617, iSSN: 2470-6647.

[86] W. Zhang and C. C. Mi, "Compensation Topologies of High-Power Wireless Power Transfer Systems," *IEEE Transactions on Vehicular Technology*, vol. 65, no. 6, pp. 4768–4778, Jun. 2016.

[87] J. Mühlethaler, "Modeling and multi-objective ptimization of inductive power components," Ph.D. dissertation, ETH Zurich, 2012.

[88] J. Deng, Y. Zhang, S. Wang, Z. Wang, and Y. Yang, "The Design and Coupler Optimization of a Single-Transmitter Coupled Multi-Receiver Inductive Power Transfer System for Maglev Trains," *IEEE Transactions on Transportation Electrification*, pp. 1–1, 2021, conference Name: IEEE Transactions on Transportation Electrification.

[89] A. Berger, M. Agostinelli, S. Vesti, J. A. Oliver, J. A. Cobos, and M. Huemer, "A Wireless Charging System Applying Phase-Shift and Amplitude Control to Maximize Efficiency and Extractable Power," *IEEE Transactions on Power Electronics*, vol. 30, no. 11, pp. 6338–6348, Nov. 2015, conference Name: IEEE Transactions on Power Electronics.

[90] D. Pehrman, Y. Liu, C. Cui, and X. Huang, "Loss Reduction by Synchronous Rectification in a 50 kW SiC-based Inductive Power Transfer System," in *IECON 2020 The 46th Annual Conference of the IEEE Industrial Electronics Society*, Oct. 2020, pp. 3907–3912, iSSN: 2577-1647.

[91] C. Jung, "Power Up with 800-V Systems: The benefits of upgrading voltage power for battery-electric passenger vehicles," *IEEE Electrification Magazine*, vol. 5, no. 1, pp. 53–58, Mar. 2017, conference Name: IEEE Electrification Magazine.

[92] J. M. Miller, O. C. Onar, C. White, S. Campbell, C. Coomer, L. Seiber, R. Sepe, and A. Steyerl, "Demonstrating Dynamic Wireless Charging of an Electric Vehicle: The Benefit of Electrochemical Capacitor Smoothing," *IEEE Power Electronics Magazine*, vol. 1, no. 1, pp. 12–24, Mar. 2014.

[93] G. A. Covic, J. T. Boys, M. L. G. Kissin, and H. G. Lu, "A Three-Phase Inductive Power Transfer System for Roadway-Powered Vehicles," *IEEE Transactions on Industrial Electronics*, vol. 54, no. 6, pp. 3370–3378, Dec. 2007.

[94] C. Riekerk, "Digital Control of a Wireless Power Transfer System for Electrical Vehicles," Jun. 2020. [Online]. Available: https://repository.tudelft.nl/islandora/object/uuid%3A3aa0f0e5-96be-466d-9a0f-28fdb4c53813

[95] W. Shi, J. Deng, Z. Wang, and X. Cheng, "The Start-up Dynamic Analysis and One Cycle Control-PD Control Combined Strategy for Primary-Side Controlled Wireless Power Transfer System," *IEEE Access*, vol. 6, pp. 14 439–14 450, 2018.

[96] Z. Zhou, L. Zhang, Z. Liu, Q. Chen, R. Long, and H. Su, "Model Predictive Control for the Receiving-Side DC–DC Converter of Dynamic Wireless Power Transfer," *IEEE Transactions on Power Electronics*, vol. 35, no. 9, pp. 8985–8997, Sep. 2020, conference Name: IEEE Transactions on Power Electronics.

[97] J. Xu, T. B. Soeiro, F. Gao, L. Chen, H.-J. Tang, P. Bauer, and T. Dragicevic, "Carrier-Based Modulated Model Predictive Control Strategy for Three-Phase Two-level VSIs," *IEEE Transactions on Energy Conversion*, pp. 1–1, 2021, conference Name: IEEE Transactions on Energy Conversion.

[98] C. Qi, Z. Lang, L. Su, X. Chen, and H. Miao, "Finite-Control-Set Model Predictive Control for a Wireless Power Transfer System," in *2019 IEEE International Symposium on Predictive Control of Electrical Drives and Power Electronics (PRECEDE)*, May 2019, pp. 1–5.

[99] Chwei-Sen Wang, G. A. Covic, and O. H. Stielau, "Power transfer capability and bifurcation phenomena of loosely coupled inductive power transfer systems," *IEEE Transactions on Industrial Electronics*, vol. 51, no. 1, pp. 148–157, Feb. 2004.

[100] Y. Geng, Z. Yang, and F. Lin, "Design and Control for Catenary Charged Light Rail Vehicle Based on Wireless Power Transfer and Hybrid Energy Storage System," *IEEE Transactions on Power Electronics*, vol. 35, no. 8, pp. 7894–7903, Aug. 2020, conference Name: IEEE Transactions on Power Electronics.

[101] W. V. Wang and D. J. Thrimawithana, "A Novel Converter Topology for a Primary-Side Controlled Wireless EV Charger With a Wide Operation Range," *IEEE Journal of Emerging and Selected Topics in Industrial Electronics*, vol. 1, no. 1, pp. 36–45, Jul. 2020, conference Name: IEEE Journal of Emerging and Selected Topics in Industrial Electronics.

[102] J. M. Miller, P. T. Jones, J. Li, and O. C. Onar, "ORNL Experience and Challenges Facing Dynamic Wireless Power Charging of EV's," *IEEE Circuits and Systems Magazine*, vol. 15, no. 2, pp. 40–53, 2015.

[103] W. Shi, J. Dong, T. B. Soeiro, and P. Bauer, "Integrated Solution for Electric Vehicle and Foreign Object Detection in the Application of Dynamic Inductive Power Transfer," *IEEE Transactions on Vehicular Technology*, pp. 1–1, 2021, conference Name: IEEE Transactions on Vehicular Technology.

[104] S. Cui, Z. Wang, S. Han, C. Zhu, and C. C. Chan, "Analysis and Design of Multiphase Receiver with Reduction of Output Fluctuation for EV Dynamic Wireless Charging System," *IEEE Transactions on Power Electronics*, pp. 1–1, 2018.

[105] X. Li, J. Hu, H. Wang, X. Dai, and Y. Sun, "A New Coupling Structure and Position Detection Method for Segmented Control Dynamic Wireless Power Transfer Systems," *IEEE Transactions on Power Electronics*, vol. 35, no. 7, pp. 6741–6745, Jul. 2020, conference Name: IEEE Transactions on Power Electronics.

[106] Y. Li, J. Hu, T. Lin, X. Li, F. Chen, Z. He, and R. Mai, "A New Coil Structure and Its Optimization Design With Constant Output Voltage and Constant Output Current for Electric Vehicle Dynamic Wireless Charging," *IEEE Transactions on Industrial Informatics*, vol. 15, no. 9, pp. 5244–5256, Sep. 2019, conference Name: IEEE Transactions on Industrial Informatics.

[107] S. Li, L. Wang, Y. Guo, C. Tao, and L. Ji, "Power Stabilization With Double Transmitting Coils and T-Type Compensation Network for Dynamic Wireless Charging of EV," *IEEE Journal of Emerging and Selected Topics in Power Electronics*, vol. 8, no. 2, pp. 1801–1812, Jun. 2020, conference Name: IEEE Journal of Emerging and Selected Topics in Power Electronics.

[108] C. Cai, M. Saeedifard, J. Wang, P. Zhang, J. Zhao, and Y. Hong, "A Cost-Effective Segmented Dynamic Wireless Charging System With Stable Efficiency and Output Power," *IEEE Transactions on Power Electronics*, vol. 37, no. 7, pp. 8682–8700, Jul. 2022, conference Name: IEEE Transactions on Power Electronics.

[109] K. Shi, C. Tang, H. Long, X. Lv, Z. Wang, and X. Li, "Power Fluctuation Suppression Method for EV Dynamic Wireless Charging System Based on Integrated Magnetic

Coupler," *IEEE Transactions on Power Electronics*, pp. 1–1, 2021, conference Name: IEEE Transactions on Power Electronics.

[110] G. R. Nagendra, G. A. Covic, and J. T. Boys, "Sizing of Inductive Power Pads for Dynamic Charging of EVs on IPT Highways," *IEEE Transactions on Transportation Electrification*, vol. 3, no. 2, pp. 405–417, Jun. 2017.

[111] M. G. S. Pearce, G. A. Covic, and J. T. Boys, "Robust Ferrite-less Double D Topology for Roadway IPT Applications," *IEEE Transactions on Power Electronics*, pp. 1–1, 2018.

[112] B. Song, S. Dong, Y. Li, and S. Cui, "A Dual-Layer Receiver With a Low Aspect Ratio and a Reduced Output Fluctuation for EV Dynamic Wireless Charging," *IEEE Transactions on Power Electronics*, vol. 35, no. 10, pp. 10 338–10 351, Oct. 2020.

[113] B. Song, S. Cui, Y. Li, and C. Zhu, "A narrow-rail three-phase magnetic coupler with uniform output power for EV dynamic wireless charging," *IEEE Transactions on Industrial Electronics*, pp. 1–1, 2020, conference Name: IEEE Transactions on Industrial Electronics.

[114] J. Shin, S. Shin, Y. Kim, S. Ahn, S. Lee, G. Jung, S.-J. Jeon, and D.-H. Cho, "Design and Implementation of Shaped Magnetic-Resonance-Based Wireless Power Transfer System for Roadway-Powered Moving Electric Vehicles," *IEEE Transactions on Industrial Electronics*, vol. 61, no. 3, pp. 1179–1192, Mar. 2014, conference Name: IEEE Transactions on Industrial Electronics.

[115] W. Shi, J. Dong, S. Bandyopadhyay, F. Grazian, T. B. Soeiro, and P. Bauer, "Comparative Study of Foreign Object and Misalignment in Inductive Power Transfer Systems," in *IECON 2019 - 45th Annual Conference of the IEEE Industrial Electronics Society*, vol. 1, Oct. 2019, pp. 2634–2639, iSSN: 1553-572X.

[116] W. Shi, F. Grazian, J. Dong, T. B. Soeiro, and P. Bauer, "Detection of Metallic Foreign Objects and Electric Vehicles Using Auxiliary Coil Sets for Dynamic Inductive Power Transfer Systems," in *2020 IEEE 29th International Symposium on Industrial Electronics (ISIE)*, Jun. 2020, pp. 1599–1604, iSSN: 2163-5145.

Curriculum Vitæ

Wenli SHI

11-10-1992	Born in Wuhan, China.

Education

2018-2023	Ph.D. candidate Delft University of Technology (TU Delft), the Netherlands
2015–2018	MSc in Mechanical Engineering Beijing Institute of Technology, China
2011–2015	BSc in Automotive Engineering Jilin University, China

Awards

2022	Apple prize - ESE Department of TU Delft
2022	Best paper award - Powerweb of TU Delft

List of Publications

Journal papers

1. W. Shi, J. Dong, G. Yu, G. Zhu, P. Bauer, “Low Output Power Ripple Dynamic Wireless Power Transfer based on Dual-Phase Non-Overlapped Transmitters”, *preprint*.

2. W. Shi, J. Dong, T. B. Soeiro, C. Riekerk, F. Grazian, G. Yu, P. Bauer, “Design of a highly efficient 20-kw inductive power transfer system with improved misalignment performance”, *IEEE Transactions on Transportation Electrification*, 8(2):2384-2399.

3. W. Shi, J. Dong, T. B. Soeiro, J. Deng, C. Riekerk, P. Bauer, “Continuous Reduced-Order Dynamic Model Based on Energy Balancing for Inductive Power Transfer Systems”, *IEEE Transactions on Power Electronics*, 37(8):9959-9971.

4. W. Shi, J. Dong, T. B. Soeiro, P. Bauer, “Integrated solution for electric vehicle and foreign object detection in the application of dynamic inductive power transfer”, *IEEE Transactions on Vehicular Technology*, 70(11):11365-11377.

As a co-author:

1. G. Zhu, J. Dong, W. Shi, T. B. Soeiro, J. Xu, P. Bauer, “A Mode-Switching Based Phase Shift Control for Optimized Efficiency and Wide ZVS Operations in Wireless Power Transfer Systems”, *IEEE Transactions on Power Electronics*, 38(4):5561-5575.

2. C. Riekerk, W. Shi, J. Dong, T. B. Soeiro, P. Bauer, “Design of a Highly Efficient 50 kW Inductive Power Transfer System for the Opportunity Charging of Electric Buses”, *under review*.

Conference papers

1. W. Shi, J. Dong, S. Bandyopadhyay, F. Grazian, T. B. Soeiro, P. Bauer, "Comparative Study of Foreign Object and Misalignment in Inductive Power Transfer Systems", *IECON 2019 - 45th Annual Conference of the IEEE Industrial Electronics Society*, 2019, 2634-2639.

2. W. Shi, F. Grazian, J. Dong, T. B. Soeiro, P. Bauer, "Analysis of Magnetic Field Emissions in Inductive Power Transfer EV Chargers Following Reference Designs in SAE J2954/2019", *2020 IEEE International Symposium on Circuits and Systems (ISCAS)*, 2020, 1-5.

3. W. Shi, F. Grazian, J. Dong, T. B. Soeiro, P. Bauer, "Detection of Metallic Foreign Objects and Electric Vehicles Using Auxiliary Coil Sets for Dynamic Inductive Power Transfer Systems", *2020 IEEE 29th International Symposium on Industrial Electronics (ISIE)*, 2020, 1599-1604.

4. W. Shi, F. Grazian, S. Bandyopadhyay, J. Dong, T. B. Soeiro, P. Bauer, "Analysis of Dynamic Charging Performances of Optimized Inductive Power Transfer Couplers", *2021 IEEE 19th International Power Electronics and Motion Control Conference (PEMC)*, 2021, 751-756.

As a co-author:

1. F. Grazian, W. Shi, J. Dong, P. van Duijsen, T. B. Soeiro, P. Bauer, "Survey on Standards and Regulations for Wireless Charging of Electric Vehicles", *2019 AEIT International Conference of Electrical and Electronic Technologies for Automotive (AEIT AUTOMOTIVE)*, 2019, 1-5.

2. F. Grazian, W. Shi, T. B. Soeiro, J. Dong, P. van Duijsen, P. Bauer, "Compensation network for a 7.7 kW wireless charging system that uses standardized coils", *2020 IEEE International Symposium on Circuits and Systems (ISCAS)*, 2020, 1-5.

3. F. Grazian, W. Shi, T. B. Soeiro, J. Dong, P. Bauer, "Electric Vehicle Charging Based on Inductive Power Transfer Employing Variable Compensation Capacitance for Optimum Load Matching", *IECON 2020 The 46th Annual Conference of the IEEE Industrial Electronics Society*, 2020, 5262-5267.

4. F. Grazian, W. Shi, T. B. Soeiro, J. Dong, P. van Duijsen, P. Bauer, "Quality Factor Based Design Guideline for Optimized Inductive Power Transfer", *2020 IEEE PELS Workshop on Emerging Technologies: Wireless Power Transfer (WoW)*, 2020, 178-183.

5. F. Grazian, W. Shi, T. B. Soeiro, P. Bauer, "Coils' Current Distortion Due to Variable Series Compensation Capacitance in EV Wireless Charging for a Constant Optimum Load", *2022 Wireless Power Week (WPW)*, 2022, 54-59.

Acknowledgments

I enjoyed the PhD study at TU Delft because I received lots of love on this journey and was never alone. This love led me to conduct research that I am proud of and to finally grow up as a researcher.

First of all, I would like to thank my promotor, Prof. Bauer, for giving me the opportunity to join the DCE&S group, for the insightful guidance to develop my research, for supporting me during my six-month absence in China, and for helping me go through the darkness in 2022.

I was fortunate to have Jianning as my supervisor. I learned a lot from you both technically and philosophically. I benefited from your way of conducting good research as well as being a good researcher. I have brought you many headaches in research and worries in life, but thanks to your encouragement and always-there help that made me feel joyful to do my research and live in Delft. Thank you for being my supervisor and friend.

I want to thank Thiago who was always ready to answer my questions and solve experimental problems. I enjoyed every conversation with you in the office, corridor, coffee room, and lab. I was impressed by your experience, knowledge, and passion for research which was a dreaming example for me. I feel honored to work with him.

I also want to thank Sharmila for your kindness and help with my endless requests. Thank you for arranging the gifts and beautiful flowers, and your yoga suggestions worked well to help me calm down! Thank you to the lab managers Bart, Wim, Harry, Mladen, and Joris, who helped me with hardware issues and building the professional movable platform.

I want to say thanks to my office mates who fought together in the PhD journey to be good researchers. Thank you Marco, I enjoyed the "Ciao fratello" everyday morning which was a great source of motivation for me. My fratello was always active in both research and life, and that's probably why his group photo has the most "charming" eyes. You and Vitoria impressed my life in Delft with many unforgettable memories. I wish you two all the best for the future. Thank you Francesca, I feel at home working with you. You were always so kind and considerate. I gained a lot of experience and knowledge about wireless charging from you. Thank you Wiljan, it is very nice to have you as an office mate especially when I encountered some Dutch language issues. You were always friendly and willing to help. I also want to thank other wireless charging teammates, Calvin, Guangyao, Yi, and Gangwei. We helped each other and had inspiring discussions about wireless charging research.

The DCE&S group is a big family where everyone tries to give care and help. I am very happy to be part of this lovely group. Sachin and Tianming, thank you for your enthusiasm for badminton. I enjoyed every battle we had and soon we will have more. Yunhe, Yang, Lyu, Lu, Junzhong, Junjie, Yun, Jundong, and Kevin, thank you all for your kind care, concerns and help. I enjoyed the barbecue and hotpot parties which is a wonderful part of my life in Delft. Lucia, thank you for your great company in Lisbon. I want to say thank you for the interesting daily conversations with Ibra, Farshid, Dhanashree, Djurre, Christian, Sohrab, Alejandro, Miad, Joel, Gautam, Rohan, Faezeh, Nikos, Carina, Yawen,

Heshi, Zichen, Dario and Adnan. I would like to thank the graduated seniors for welcoming me at the start and setting good examples, Soumya, Nils, Pavel, Jiayang, Guillermo, Nishant, Victor, and Udai. I would like to thank the assistant professors, Zian, Mohamad, Aditiya, Gautham, and Laura.

The past years in Delft have been enjoyable and memorable. I want to especially thank Jing for being my good roommate. It was always fun talking and joking with you after work. I hope we can have more bike tours soon. Zhenyu, this is the eighth year since we knew each other. Thank you for keeping me company, for your delicious homemade food, and for your sincere help. Zhi, thank you for being my professional gym trainer.

I could not have completed this long journey without the unconditional love and support of my family. I would like to thank my father, Mr. Shuzhai Shi and my mother, Mrs. Wurong Li, you are my constant source of inspiration and strength. Wenbin, Wenjuan, and Yajuan, I am blessed to have you as my brothers and sisters. I hope I can be your proud.

Lastly, I would like to thank Meiling. We have shared so many joys and frustrations together since 2011. I can't imagine how I could make it without you. Thank you for always trusting and encouraging me. We are married! I can't wait to see how beautiful and happy our lives will be!

Wenli
Delft, October 2023